UNIVERSITY OF CALIFORNIA,
IRVINE

Quantifying the Neutrino Energy and Pointing Resolution of the ARIANNA Detector

DISSERTATION

submitted in partial satisfaction of the requirements
for the degree of

DOCTOR OF PHILOSOPHY

in Physics

by

Geoffrey George Gaswint

Dissertation Committee:
Professor Steven Barwick, Chair
Professor Stuart Kleinfelder
Professor Simona Murgia

2021

DEDICATION

I dedicate this thesis to my mother, Isabel Graves, and my two fathers, Peter Graves and Guy Gaswint. Thank you for giving me your unconditional support and love that has allowed me to be successful in life. I am extremely fortunate to have you - the most amazing parents and role models in the Universe! I love you with all my heart, and I look forward to our many more memories to be had!

TABLE OF CONTENTS

LIST OF FIGURES

LIST OF TABLES

ACKNOWLEDGMENTS

The work in this thesis would not be possible without all the compounding achievements of previous scientists and their support. Thank you to everyone who have dedicated parts of their lives in order to advance scientific knowledge for humanity.

I would like to give a special thanks to Steven Barwick, Christopher Persichilli, and Christian Glaser who had a huge impact on my development into becoming a scientist and also on my character as a teammate. My success is in large part because of their guidance and support. The community in ARIANNA has never discouraged me even when I made mistakes and has always pushed me into the right direction. Thank you for the opportunity to learn and help advance the ARIANNA experiment.

Also, I would like to give credit to my family, in particular my mother and two fathers who gave me the support that was necessary to minimize stress and focus on education. Without their support, achieving a Ph.D. would seem infeasible. I am very lucky with the cards I have been dealt in life, and I am very grateful for all the freedom and opportunities I have been given.

Further, the support of my friends was crucial in times when necessary. In particular, Trevor Nesbitt provided me with professional and friendly guidance that helped me become a more proficient writer and communicator along with a better programmer.

I would like to acknowledge the Cares Act Emergency Grant and the Departmental Dissertation Fellowship for the financial help I received. I would also like to acknowledge the Journal of Instrumentation for publishing my work.

CURRICULUM VITAE

Geoffrey George Gaswint

EDUCATION

Doctor of Philosophy in Physics **2021**
University of California, Irvine *Irvine, California*

Masters of Science in Physics **2019**
University of California, Irvine *Irvine, California*

Bachelor of Arts in Physics
Bachelor of Arts in Pure Mathematics **2014**
University of California, Berkeley *Berkeley, California*

RESEARCH EXPERIENCE

Graduate Research Assistant **2017–2021**
University of California, Irvine *Irvine, California*

TEACHING EXPERIENCE

Teaching Assistant **2016–2021**
University of California, Irvine *Irvine, California*

JOURNAL PUBLICATIONS

Probing the angular and polarization reconstruction of the ARIANNA detector at the South Pole **2020**
Journal of Instrumentation

Neutrino vertex reconstruction with in-ice radio detectors using surface reflections and implications for the neutrino energy resolution **2019**
Journal of Cosmology and Astroparticle Physics

NuRadioReco: A reconstruction framework for radio neutrino detectors **2019**
The European Physical Journal C

Targeting ultra-high energy neutrinos with the ARIANNA experiment **2019**
Advances in Space Research

SOFTWARE

ARIANNAanalysis `https://github.com/ggaswint/ARIANNAanalysis`
Data analysis software

NuRadioReco `https://github.com/nu-radio/NuRadioReco`
Data processing software

NuRadioMC `https://github.com/nu-radio/NuRadioMC`
Monte Carlo radio-neutrino detector simulation

ABSTRACT OF THE DISSERTATION

Quantifying the Neutrino Energy and Pointing Resolution of the ARIANNA Detector

By

Geoffrey George Gaswint

Doctor of Philosophy in Physics

University of California, Irvine, 2021

Professor Steven Barwick, Chair

The emerging field of radio based neutrino astronomy holds promise in answering long lasting questions about our universe such as identifying the sources of ultra-high energy (UHE) cosmic rays. This requires a multi-messenger effort in astronomy which is a relatively new collaboration between the various particles/waves used to study space. It is important for radio neutrino astronomers to show that UHE neutrino detection can be made with excellent precision in direction and energy reconstruction for the field to grow from pilot phases into large scale experiments. The Antarctic Ross Ice-shelf Antenna Neutrino Array (ARIANNA) is one such detector with this goal. ARIANNA aims to detect UHE neutrinos via radio (Askaryan) emission from particle showers when a neutrino interacts with ice, which is an efficient method for neutrinos with energies between 10^{16} eV and 10^{20} eV. The ARIANNA radio detectors are located in Antarctic ice just beneath the surface. Neutrino observation requires that radio pulses propagate to the antennas at the surface with minimum distortion by the ice and firn medium. To reconstruct the direction, a measurement of polarization, radio frequency signal direction, and viewing angle off of the Cerenkov cone, along with ice attenuation and signal trajectories must be made. The energy further requires a modeling of the Askaryan radiation created from the stochastic processes of particle showers in dense media. This results in an irreducible energy resolution, which sets the goal for energy reconstruction techniques.

An experimental evaluation of radio signal polarization and direction resolution was completed using the residual hole from the South Pole Ice Core (SPICEcore) Project. Radio pulses were emitted from a transmitter located down to 1.7 km below the snow surface. After deconvolving the raw signals for the detector response and attenuation from propagation through the ice, the signal pulses show no significant distortion and agree with a reference measurement of the emitter made in an anechoic chamber. The origin of the transmitted radio pulse was measured with an angular resolution of 0.37°, indicating that the neutrino direction can be determined with good precision if the polarization and viewing angle of the radio-pulse can be well determined. In the present study we obtained a resolution of the polarization vector of 2.7°. Neither measurement show a significant offset relative to expectation.

We also report on the results of a simulation study of the ARIANNA neutrino direction and energy resolution. The software tool NuRadioMC, which is rapidly becoming the industry standard, was used to reconstruct the polarization and viewing angle to determine the neutrino direction. Multiple models of Askaryan radiation and detector sites along with a range of neutrino energies were tested. The neutrino space angle resolution was determined to be below 3°, which is governed by the polarization uncertainty of the same scale. The polarization reconstruction from experimental SPICEcore studies showed large systematic errors that results in the 2.7° uncertainty, whereas the per depth resolution is a sub degree statistical error. Therefore it is expected that the polarization resolution, which is the dominant contribution to the neutrino space angle resolution, will be greatly improved in future studies by determining and eliminating systematic effects such as antenna modeling. Neutrino energy resolution is reported at 40% for 10^{18} eV neutrinos, which is below the inelasticity limit and therefore ARIANNA is not limited by its detectors ability to reconstruct the energy.

Chapter 1

Introduction

1.1 Multi-messenger Astronomy

In 2013, IceCube presented the first evidence of the detection of high-energy neutrinos, which further pushed astronomy into the multi-messenger era [23]. For the longest time, humans have studied the Universe through a single messenger, light, or more specifically electromagnetic radiation. However, electromagnetic radiation has it's limitation on studying the Universe. Perhaps the most obvious of which is the cosmic dead end where the Universe had cooled enough for ions and electrons to recombine and form atoms known as the epoch of recombination. This occurred when the Universe was roughly 380,000 years old. Electromagnetic radiation cannot be used to study the Universe before this time because the extremely hot plasma that existed scattered this radiation so efficiently that the Universe is opaque (sometimes referred to as the wall of light). The cosmic microwave background (CMB) is a measurement of the oldest photons (i.e. the ones whose last scatter was during this recombination period). This is an example of a time limitation as it puts a limit on the farthest back in time one can hope to study the Universe when using electromagnetic

radiation. There are other limitations of physical quantities as well, one of which is the energy.

Ultra high energy (UHE) photons can and will interact with another photon through photon-photon pair production which is the result of a UHE photon colliding with a lower energy photon and resulting in an electron-positron pair. These electrons and positrons can then undergo annihilation, creating more photons. The resulting photons have less energy than the initial UHE photon. Pair production requires that the minimum energy of the two colliding photons be larger than the rest mass energy of the resulting electron and positron pair, $2m_e c^2 \approx 1.02$ MeV [24]. As the energy becomes much larger than the threshold energy, pair production starts to dominate. This energy essentially translates to a PeV photon interacting with a CMB photon, or a TeV photon interacting with an optical or near infrared (IR) photon. The occurrence of this process is quantified through the mean free path, which is the average distance that a UHE photon travels before pair producing. It is the mean free path that provides the limitation on the distance an UHE photon can travel with a given energy and this boundary is known as the energy horizon. The distance a photon can travel before pair producing varies with energy and is plotted in figure 1.1. At really extreme energies a photon can even undergo double pair production (resulting in two electrons and positrons) which would only serve to reduce the UHE photons energy by even more [24]. The highest energy photons detected so far have been on the few 100 TeV scale [25].

If we are ever to observe areas of the Universe that are otherwise impossible with photons, we will have to switch to a new messenger for astronomy, and this is where the multi-messenger era begins. The idea of multi-messenger astronomy is to be able to study an object in space with more than just one messenger which then would reduce the limitations of knowledge that can be learned from that object. Luckily, the earth is not only bombarded with photons from the Universe but a range of other particles and waves that are so far grouped into three more categories (there may be even more in the future as we advance particle physics

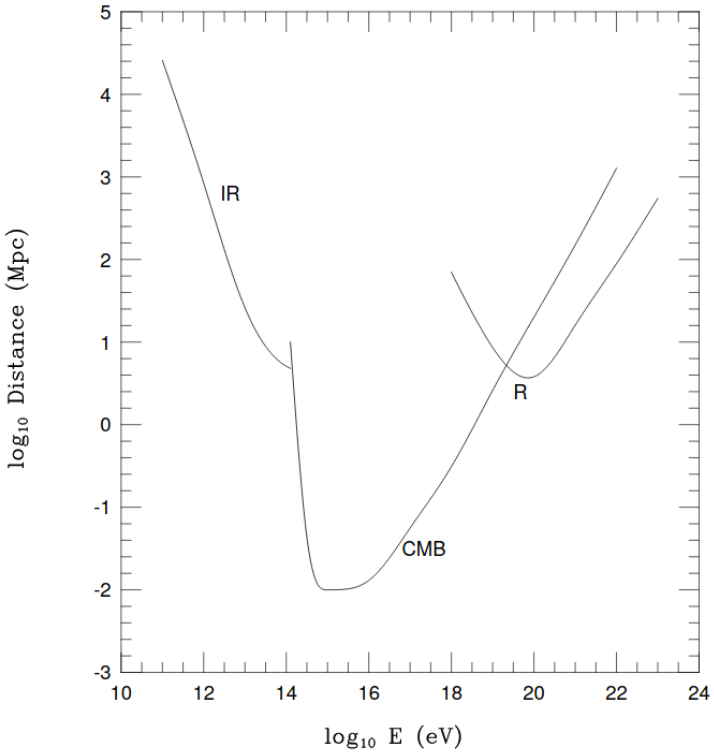

Figure 1.1: Shows the mean free path of pair production for UHE photons of various energies which then coalesce into the energy horizon [1]. The secondary photon has wavelengths in the infrared (IR), microwave (CMB), or radio (R) spectrum.

further). The other candidates include the cosmic-rays (charges elementary particles and nuclei), gravitational waves, and neutrinos. Neutrinos are a fascinating subatomic particle with vast mysteries and is the messenger of choice for this thesis, but before getting into neutrinos, I would first like to introduce the concept and limitations of using cosmic rays or gravitational waves to study the Universe.

1.2 Gravitational Waves

Einstein's theory of General Relativity predicts gravitational waves that propagate at the speed of light (see section 21.2.3 in [2]). Gravitational wave are disturbances in spacetime and are generated by accelerating masses. The first bursts of gravitational waves detected were from a binary black-hole coalescence. It was detected in September of 2015 by US-based Laser Interferometer Gravitational-wave Observatory (LIGO), making gravitational waves the youngest category of messenger types [26].

Gravitational waves, being the distortion of spacetime itself, will travel in straight lines, preserving the direction information and can be used to pin-point sources. This is similar to photons when neglecting the small effects gravity has on light. The smallest objects known to emit gravitational waves are black-holes and neutron stars which correspond to wavelengths of roughly a kilometer. In order to detect gravitational waves on the kilometer scale, a detector is required to have kilometer long antennas. For even larger objects, a detector would require even bigger antennas, and this quickly grows to the size of earth and larger. This sets a human financial and constructional limitation on current gravitational detectors that will need to be overcome in order to detect larger waves, putting a strict limitation on how big of objects we can detect using gravitational waves in the near future.

1.3 Cosmic Rays

Cosmic rays are the broad category of ionizing radiation coming from space. They are composed of charged elementary particles and nuclei and are very abundant, with roughly 20 cosmic rays of MeV energies striking you every second. Cosmic rays are the oldest group of messengers used in astronomy (excluding light of course), with the first being detected in 1912 by Victor Hess in a balloon experiment [27]. In 1962, John Linsley discovered one of the first UHE cosmic rays, with an energy of 10^{20}eV [28]. This showed the vast range of energies that cosmic rays can have; between an MeV to tens of joules.

Like using a telescope for light, one would want to detect cosmic rays directly with a dedicated detector. However, also like light, at the highest energies the cosmic ray flux becomes too small for direct measurements to be sufficient, and detection then has to turn to measuring the particle air showers that are produced when UHE cosmic rays interact with the earth's atmosphere. This is even harder for UHE photons that induce electromagnetic showers, because the number of UHE cosmic rays can outnumber UHE photons by 10,000 to 1 or more [29].

Figure 1.2 shows the all composition cosmic ray flux as a function of energy-per-nucleus taken from [2]. There are four striking features in figure 1.2 that are worth discussion - the two knees, the ankle, and the sharp cutoff at the highest energy. The sources of these features are still under debate. One strong argument for the first knee, which can be seen at an energy of roughly 10^{15}eV, is that cosmic accelerators in the Milky Way have reached their maximum energy for proton acceleration [30]. The second knee, found at around 10^{17}eV, could have a similar origin to the first knee but would be due to the limiting energy of accelerating larger cosmic rays such as iron [30]. The ankle, found at 10^9 GeV, shows a slight increase in the trend of the flux vs energy. One possible explanation for this is that the cosmic ray flux from extragalactic origins is overtaking the cosmic ray flux from within the Milky Way.

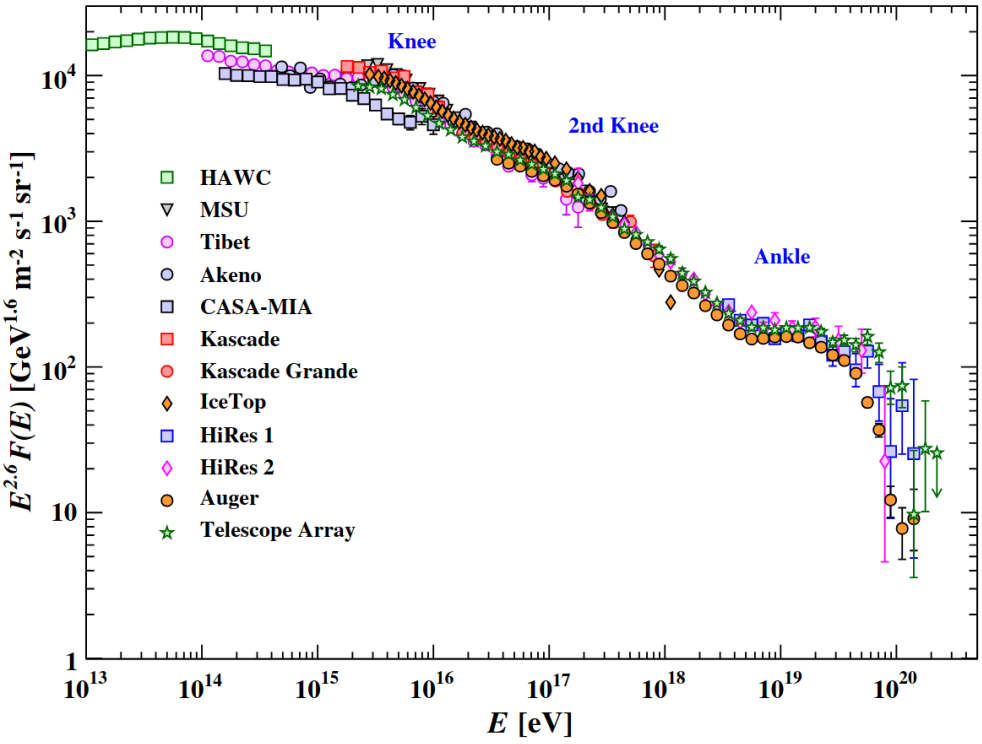

Figure 1.2: All subatomic particle and nuclei cosmic ray flux as a function of energy [2].

Cosmic rays have the nice feature that they extend the energy horizon limitation placed by photons, but in turn they have their own energy limitation. Just like photons, UHE cosmic rays have a limitation on the distance they can travel before losing energy. One way they can lose energy is through red shifting which increases the de broglie wavelength. UHE cosmic rays also undergo pair production, and either photopion production for protons, or photo-disintegration for heavier nuclei. See figure 1.3 for how this converts into the energy horizon for UHE cosmic rays.

One compelling reason that the highest energetic cosmic rays in figure 1.2 are of extragalactic origin is through the absence of the detection of PeV photons. UHE cosmic rays produce UHE photons and if UHE cosmic rays originated within our own galaxy, then UHE photons with PeV energies should be observed. This is because the mean free path length of PeV photons is on galactic scales and therefore can travel from within our galaxy to Earth without interacting with the CMB (see figure 1.1). The missing detection of PeV photons suggests

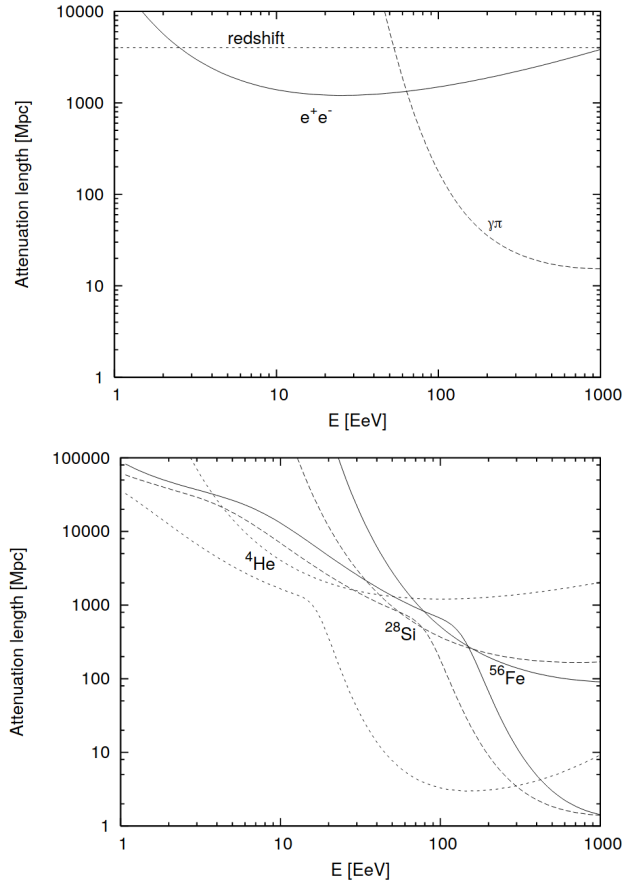

Figure 1.3: (First) proton energy horizon, with the three main mechanism for energy loss; redshift, photopion production (labeled as $\gamma\pi$) and pair production (labeled as e^+e^-). (Second) energy horizon for heavier nuclei with the lower curves being caused by photo-disintegration and the higher curves being caused by pair production [3].

that UHE cosmic rays originate from outside the Milky Way, which is roughly 32 kiloparsecs in diameter.

Cosmic rays are charged particles, so they will bend as they travel through the galactic and extragalactic magnetic fields of our Universe. This creates a big problem with UHE cosmic rays, that has been unsolved for decades. What is the source that is producing UHE cosmic rays? They do not travel in straight lines, so simple pointing does not work, and the distances that they have traveled are astronomical. The most important energy loss mechanism for cosmic rays that may help answer this question is through photopion production with a CMB photon. This process was first computed by Kenneth Greisen, Georgiy Zatespin, and

Vadim Kuzmin, and thus the energy horizon due to this mechanism is known as the GZK limit. The GZK process can be described as a proton interacting with a CMB photon, which undergoes a delta resonance producing a breath of secondary particles or:

$$p + \gamma_{CMB} \rightarrow \Delta^+ \rightarrow \pi^+ + n \rightarrow p + \bar{\nu_\mu} + \nu_\mu + \nu_e$$

and

$$p + \gamma_{CMB} \rightarrow \Delta^+ \rightarrow \pi^0 + p \rightarrow p + 2\gamma$$

The GZK process predicts a sharp cutoff in the cosmic ray flux around $5x10^{19}$eV, which is precisely the cutoff that is seen in Figure 1.2, providing evidence for the GZK mechanism.

What is beneficial about these two process modes is that the secondary particles produced include UHE photons and UHE neutrinos (discussed in section 1.4), which both travel in straight lines and is usually referred to as cosmogenic neutrinos or cosmogenic photons as they are produced from the photon fields in the cosmos. So taking multi-messenger astronomy at the core, if we can measure an UHE cosmic ray in coincidence with an UHE neutrino or UHE photon, then we can pin point where in the sky that UHE cosmic ray came from. Some potential candidates for UHE cosmic ray sources are shown in figure 1.4

Another question about UHE cosmic rays is that the exact composition is still heavily debated and an area of active research. It is unknown if the UHE cosmic ray composition is comprised entirely of protons, iron, or some mixture of protons and heavy nuclei. UHE neutrinos provide a way to answer this question because the flux of UHE neutrinos depends on the fractional composition of protons in UHE cosmic rays as only the protons undergo photopion production.

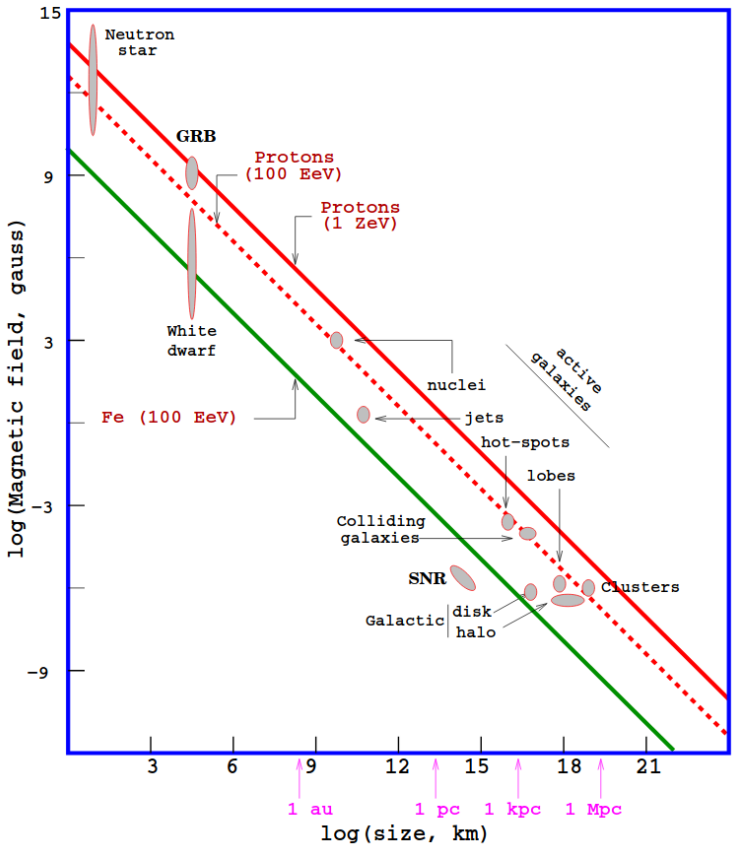

Figure 1.4: Size of potential cosmic ray sources for various magnetic field strengths. The red line assumes a cosmic ray population of pure protons with energies of 10^{21}eV, dashed red line is pure protons with energies of 10^{20}eV, and the green line represents a cosmic ray population of iron with energies of 10^{20}eV. Cosmic ray sources for these three different populations must be above their respective lines, otherwise the source would not be able to accelerate these cosmic rays to their respective energies (assumes $\beta = 1$). [1].

1.4 Neutrinos

Neutrinos are electrically neutral leptons and have the lightest known mass out of all the fermions. They have an extremely small cross-section which results in very little interactions with matter. For context, trillions of neutrinos with a range of energies pass through your body without interacting with you every second. Neutrinos are arguably the most bizarre particle because they travel near the speed of light and are the only known particle that undergoes oscillations between its three generations (electron, muon, and tauon neutrinos).

Neutrinos are also arguable one of the best messenger candidates for probing the ultra high energy Universe. Due to them being electrically neutral, they travel in straight lines similar to photons. Further, unlike photons, they are not expected to interact with the CMB and do not suffer from GZK losses, allowing them to travel cosmological distances undisturbed. This makes UHE neutrinos the natural candidate to use in coincidence with UHE cosmic rays in order to discover UHE cosmic ray sources.

All this is great news for studying the extreme energies of the Universe, but neutrinos also have their limitations, mainly in the fact that they are so rarely interacting. The drawback is that a large detector volume is needed to make the probability of detecting an UHE neutrino considerable. The flux of neutrinos naturally drops with larger and larger energies, therefore the larger the neutrino energy is, the larger the detector volume will need to be. Figure 1.5 shows the current neutrino flux measurements along with photons, and cosmic rays for comparison. To expand on the energy detection limits of neutrinos, a detector volume will need to be built on a kilometer scale.

The Antarctic Ross Ice-Shelf ANtenna Neutrino Array (ARIANNA) group aims to be at the forefront of pushing the limits on UHE neutrino detection. My thesis describes my research with the ARIANNA group which resulted in quantifying the performance of surface-based radio neutrino detection, in particular the angular resolution, which in turn describes the

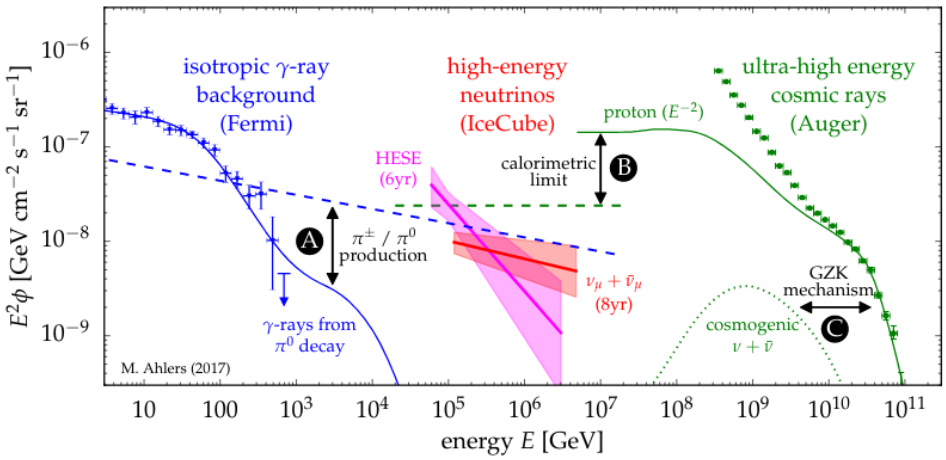

Figure 1.5: Summary of the flux of various particle messengers for different energies. The blue curve shows the gamma ray flux as measured by Fermi [4]. The red and magenta curve shows the neutrino flux measured by IceCube using up going track analysis verses HESE analysis respectively [5]. The green curve shows the flux of cosmic rays as measured by Auger [6]. Three key transitions are highlighted in this plot. A: Charged and neutral pion production leads to the emission of gamma-rays (solid blue) and neutrinos (dashed blue). B: Observed cosmic ray fluxes (solid green) produce a model independent limit on neutrino fluxes (dashed green) through what is known as the calorimetric limit [7]. C: The theoretical flux of cosmogenic neutrino emissions due to the GZK process by which cosmic rays interact with CMB photons. Taken from [5].

ability to finally pinpoint the sources of UHE cosmic rays.

1.5 Particle Shower Physics

UHE particles like cosmic rays and neutrinos are far too few for direct measurements, however, they sometimes interact with the atoms in the atmosphere or in dense media which results in many unstable secondary particles. These interactions result in either hadronic showers or electromagnetic showers.

UHE photons can induce an electromagnetic shower directly, whereas a UHE cosmic ray produces a set of secondary particles, in particular, neutral pions which nearly instantly decay into photons that in turn induce an electromagnetic shower. The electromagnetic cascade develops mainly through the intimate dance between pair production and bremsstrahlung which create even more electrons and photons, along with positrons all at lower energies. Bremsstrahlung creates photons in the shower through the deceleration of electrons as they deflect off of another electron or from the atoms in the medium. This loss of energy is converted into a photon. The photons interact with the surrounding matter undergoing pair production. Eventually the resulting particles energies fall below the critical energy for the shower development to continue increasing in particle number. At this point, ionization and excitation effects kick in, absorbing more particles in the surrounding medium than creation.

Hadronic showers proceed via the strong nuclear force and are produced from particles made up of quarks. Hadron showers are governed through hadron production, nuclear deexitations, and pion/muon decays. Some of the pions are neutral pions which then result in electromagnetic showers.

UHE neutrinos have small cross sections and therefore do not initiate showers in the air. Instead, they require a dense medium like ice for a shower to have any significant chance

of occurring. On the other hand, UHE cosmic rays and photons are more likely to induce an air shower, and hence neutrinos can be distinguished from cosmic rays or photons if a detector can determine if the shower was initiated in air or in a dense medium.

UHE particle showers produce a characteristic radio signal and the main mechanism responsible for this also differs between air showers and dense media showers. It is this radio signal that dedicated UHE detectors try to capture and reconstruct in order to learn about the properties of the shower. Radio detection of cosmic ray showers was first studied in the 1960's with the first demonstration being by J. V. Jelly [31] in 1965. However, at that time, analog detection techniques had limited the field of radio detection and the community turned it's attention to fluorescence detectors.

With the progression of the digital age, the radio detection techniques has grown new interest and the ability to detect UHE particle showers can now be studied with greater efficiency. Particle showers have two main sources of radio emission, the geometric emission which has larger contributions for longer shower lengths, and Askaryan emission which starts to dominate when the shower lengths are too short for geomagnetic effects to kick in. Particle showers in the air which are induced by UHE cosmic rays have shower lengths on the order of kilometers producing a radio signal that is dominated by geomagnetic emission. Particle showers in dense media such as ice which result from neutrino interactions, have shower lengths on the order of meters, and therefore are dominated by the Askaryan effect. Figure 1.7 gives a visual representation of the two different emission mechanisms.

Geomagnetic radio emission is caused by transverse currents induced by the Earth's magnetic field. As the shower develops, the charged particles are accelerated by the Lorentz force. When the shower is developed it reaches a maximum before losing energy due to ionization losses with the surrounding atoms in the media. The change in the transverse currents is maximized at the shower maximum, and produces the largest radio emission. because of the extreme amounts of energy in the shower, the particles travel faster than the speed

of light in air or ice. This makes the radiation Cherenkov like, and the emitted radio waves add up coherently along the Cherenkov angle. The geomagnetic emission dominates Askaryan emission in air, with Askaryan emission providing roughly 10% to the electric fields amplitude. However, in dense media, where the shower lengths are on the scale of meters, the Earth's magnetic influence is a lot weaker. This results in the Askaryan emission being the dominate factor in the radio emission of particle showers.

Askaryan radio emission is caused by the equivalence of longitudinal currents induced by a charge excess at the shower front. As the shower develops, the atoms in the surrounding media get ionized, releasing extra electrons into the shower. The Shower develops a time changing excess of negative charge at the shower front, which is maximized when the number of particles is maximized known as the shower maximum. This time varying charge excess creates a radio signature which is the source for detecting showers in dense media.

When a neutrino interacts with a proton in the ice, it can either undergo a charged current interaction which is mediated by the charged W boson, or through a neutral current interaction mediated by the neutral Z boson. Figure 1.6 depicts the Feynman diagrams for these two types of interactions and is taken from [8]. In either case, the radio emission comes from the electromagnetic part of each shower, either directly through a primary electromagnetic shower or secondarily through electromagnetic showers that originate from the development of a hadronic shower.

1.6 ARIANNA and Askaryan Radiation Detection

The ARIANNA detector, which is located in Moore's Bay on the Ross Ice Shelf near the coast of Antarctica, will be discussed in great detail in chapter 2. ARIANNA utilizes the kilometer scale attenuation lengths of radio waves produced from neutrino interactions with

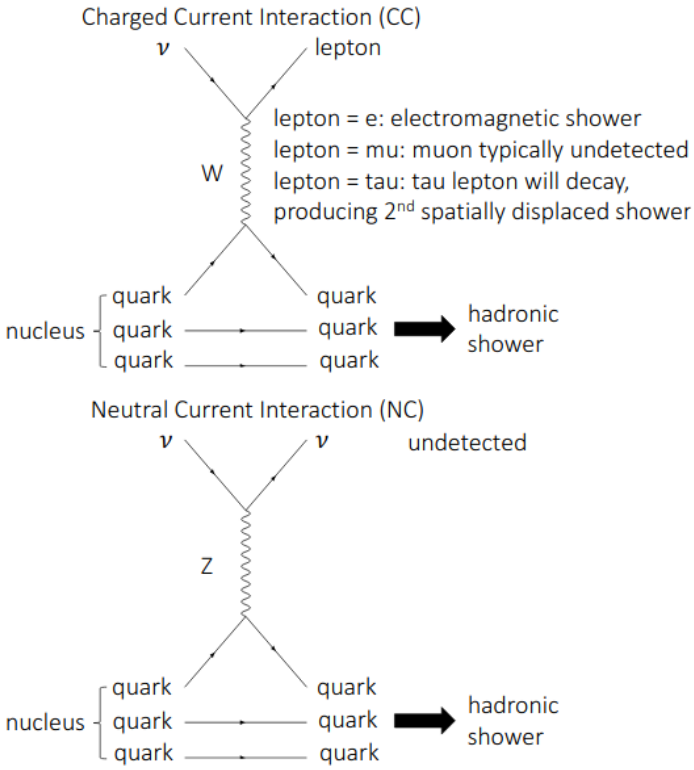

Figure 1.6: Feynman diagrams for a UHE neutrino interacting with the a nucleus. The charged current interactions (mediated by W bosons) can lead to electromagnetic showers and is more likely to occur at lower energies. Neutral current interactions initially produce only hadronic showers. Taken from [8].

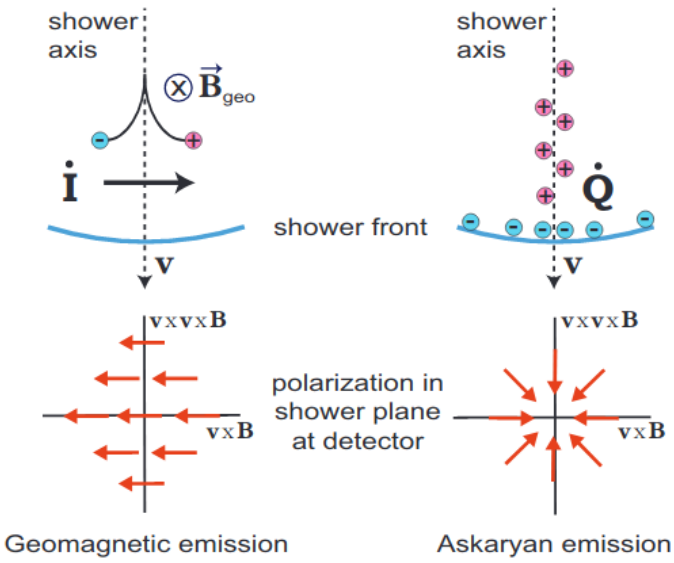

Figure 1.7: The two main modes for coherent radio emission in particle showers. The geometric mode is induced when charged particles travel through the earth;s magnetic field, producing time dependent transverse currents. The Askaryan mode is due to the build up of negative charge at the shower front through Compton scattering with the atoms within the medium and has a bigger effect for more dense media. [9].

protons in the vast sheets of ice in Antarctica. This will allow a relatively small and cost efficient detector to be built with kilometer spacing to probe the ice while maintaining a large detector volume as needed to detect UHE neutrinos.

One of the main science questions an UHE neutrino detector would be able to constrain is the diffuse flux model of UHE cosmic rays. Such a constraint could help determine the elemental composition of cosmic rays as a function of energy (Fig 1.8), the source evolution and the cosmic ray energy cutoff of the spectrum of cosmic rays injected into the intergalactic medium by the accelerator. To be able to capture such small quantities of neutrinos, a detector will need to have a large effective volume and a long live time. For example, with a volume of $1000\,\mathrm{km}^3$, a minimum of 5 years is necessary to start to constrain the most optimistic models [32].

A high quality detector should be able to determine the direction of the neutrino, so that it

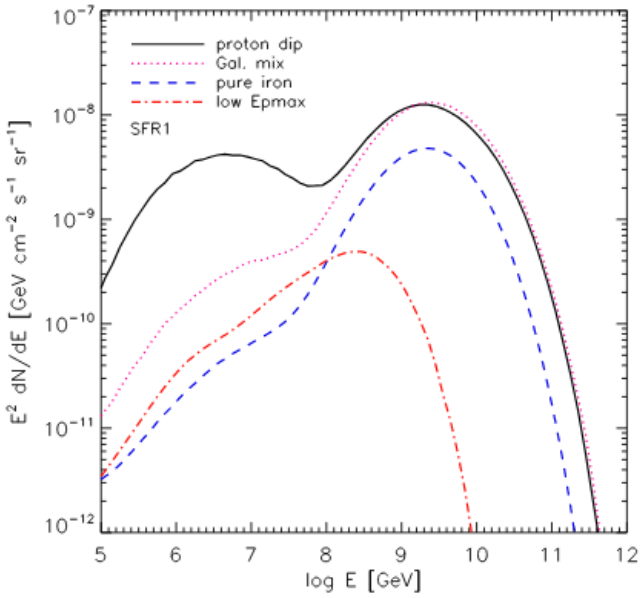

Figure 1.8: Theoretical predictions on the neutrino flux at ultra high energies for various cosmic ray populations. The black curve assumes a pure proton cosmic ray population, where as the blue dotted assumed a pure iron composition of cosmic rays. The dotted magenta curve is for a mixture of cosmic rays dominated by protons, where as the red dotted curve is for a mixture of cosmic rays dominated by iron. [10].

can be traced back to an angular region of the sky. If the angular region is characterized by a space angle less than 5°, then this reduces the potential source candidates that produced this neutrino. The direction of the neutrino relative to the coordinate system of the detector must be coupled to the time of arrival to determine both the right ascension (RA) and declination (DEC) of the neutrino direction. Fortunately, the time stamp does not need to be very accurate, and the ARIANNA clock provides an absolute accuracy of 10 ms, which meets requirements. Another requirement for the detector is to measure the energy of the neutrino. To measure this quantity, the ARIANNA detector must compute the polarization of the electric field, determine the viewing angle which indicates the emission angle of the electromagnetic pulse relative to the ideal Cherenkov cone, and determine the distance to the interaction vertex. In this thesis, we will show that ARIANNA will measure the shower energy quite precisely, to a resolution of 40 percent. However, if flavor information is not available (and so far, flavor identification has not been demonstrated yet), then the energy resolution will be limited by the unknown fraction of energy that is transferred between the neutrino and the hadronic shower, known as inelasticity. Generally, this leads to an uncertainty in the neutrino energy of a factor of 2. The goal of ARIANNA is to measure the energy of the shower so that the uncertainty of the neutrino energy is dominated by inelasticity.

(Fig. 1.9) shows the general technique to determine direction of the neutrino and energy of the shower. The polarization of Askaryan radiation is radial and is orthogonal to both the radio propagation direction and the plane made by the neutrino incoming direction and radio propagation direction. Using these criteria, the exact dependence on polarization with the neutrino direction, radio signal direction, and viewing angle is given by equation 1.1 [11].

$$\vec{p} = \vec{l} \times (\vec{v}_\nu \times \vec{l}) \tag{1.1}$$

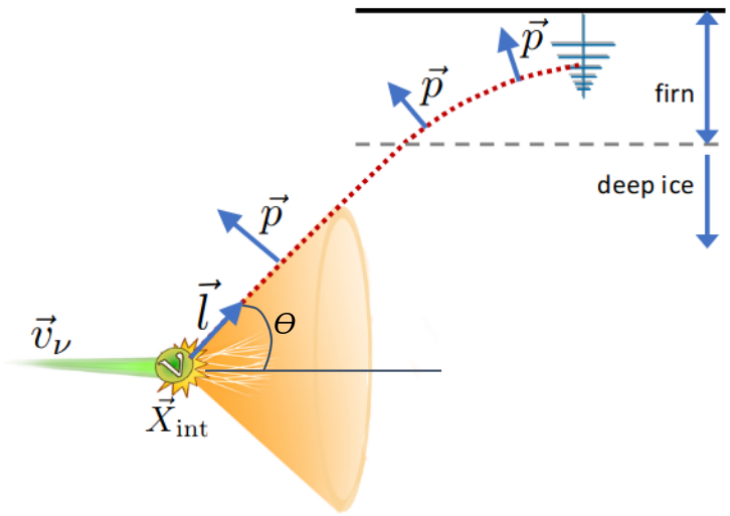

Figure 1.9: Sketch of how the neutrino induced particle shower depends on the Askaryan radiation's angular direction ($\vec{l}$), polarization ($\vec{p}$), and viewing angle (θ) along with ice properties (bending of signals in the firn). [11].

One can rearrange this to isolate the neutrino direction, utilizing the vector triple product identity and the definition of the cross product. First, using the cross product definition, the cross product between $\vec{v}_\nu$ and $\vec{l}$ results in a vector that is orthogonal to both $\vec{v}_\nu$ and $\vec{l}$. Therefore the cross product of the outer term has an angle between the two vectors of 90 degrees and the sine function of this angle results in the value of 1. Equation 1.1 can then be simplified using the magnitudes as:

$$|\vec{p}| = |\vec{l}|^2 |\vec{v}_\nu| \sin\theta_{v_\nu,l} \tag{1.2}$$

Where the commutative property was used to switch $|\vec{l}|$ and $|\vec{v}_\nu|$ and the angle, $\theta_{v_\nu,l}$, is between $\vec{v}_\nu$ and $\vec{l}$. The other route from equation 1.1 utilizes the vector triple product

identity and results in:

$$\vec{p} = \vec{v}_\nu(\vec{l}\cdot\vec{l}) - \vec{l}(\vec{l}\cdot\vec{v}_\nu) \tag{1.3}$$

This can be further solved using the dot product definition and the symmetry of the cosine function to flip the indices of the angle. The result is:

$$\vec{p} = \vec{v}_\nu|\vec{l}|^2 - \vec{l}\cos\theta_{v_\nu,l}|\vec{l}||\vec{v}_\nu| \tag{1.4}$$

rearranging this to solve for the neutrino direction gives:

$$\vec{v}_\nu = \frac{1}{|\vec{l}|^2}\big(\vec{p}\frac{|\vec{p}|}{|\vec{p}|} + \vec{l}\cos\theta_{v_\nu,l}|\vec{l}||\vec{v}_\nu|\big) \tag{1.5}$$

Where I stuck in a factor of 1 (e.g. $\frac{|\vec{p}|}{|\vec{p}|}$) which will become clear in the next step. Now, if we plug in $|\vec{p}|$ from equation 1.2 into equation 1.5 for just the numerator we get:

$$\vec{v}_\nu = \frac{1}{|\vec{l}|^2}\big(\frac{\vec{p}}{|\vec{p}|}|\vec{l}|^2|\vec{v}_\nu|\sin\theta_{v_\nu,l} + \vec{l}\cos\theta_{v_\nu,l}|\vec{l}||\vec{v}_\nu|\big) \tag{1.6}$$

The last step is to now divide $|\vec{v}_\nu|$ from both sides and distribute:

$$\frac{\vec{v}_\nu}{|\vec{v}_\nu|} = \frac{\vec{p}}{|\vec{p}|}\sin\theta_{v_\nu,l} + \frac{\vec{l}}{|\vec{l}|}\cos\theta_{v_\nu,l} \tag{1.7}$$

which finally gives us the form for finding the incoming direction of the neutrino [11].

$$\hat{\vec{v}}_\nu = \hat{\vec{p}}\sin\theta - \hat{\vec{l}}\cos\theta \tag{1.8}$$

Here I dropped the subscripts from θ which is the viewing angle of the received radio signal with respect to the shower axis and converted the quantities to unit vectors by definition. From equation 1.8 it is clear that the neutrino direction depends on the polarization, viewing angle, and radio signal's launch direction. Therefore the resolution a detector can achieve on reconstructing the neutrino direction depends on how well a detector can reconstruct these three quantities along with modeling how the ice effects the signal during propagation.

In order to be able to measure radio signal's direction, polarization, and viewing angle, there are requirements on the detector. At least three antennas, or two antenna pairs are needed to use the time delay between antennas in order to calculate the direction of the signal. Further, the detector should have orthogonal antennas to capture the different components of the electric field and hence make a measurement of the polarization. Additional pairs allow for an over-constrained solution, which theoretically will reduce systematic uncertainties such as in antenna positions or orientations. The viewing angle can be found by fitting the frequency spectrum of simulated neutrino induced radio signals to the detected event and as a consequence requires a good model for particle shower physics. The last requirement that

is not immediately obvious, is having a good understanding of the ice density as a function of depth. Since a detector measures signals at its antennas and not at the location in ice where the radio signal was produced, a detector needs to be able to backtrack the prorogation of the radio signal from detector to source. The backtracking can be done through using Fresnel equations, and Snell's law when experimental data of the ice profile is provided.

The focus of this thesis is on making a prediction of the resolution ARIANNA can achieve for the neutrino direction and energy. Therefore, throughout this work and in the past, *in situ* and simulated experiments have been performed to quantify the resolution of the key ingredients; radio signal's angular direction, polarization, viewing angle, and ice modeling. The last chapter provides a full reconstruction of neutrino direction and energy and presents the first resolution estimates made for neutrino direction reconstruction using the ARIANNA detector.

Chapter 2

The ARIANNA Detector

2.1 Features of Radio Based Neutrino Detectors

Several authors [33] have shown that the radio Cherenkov technique is superior to optical techniques for neutrino energies in excess of 10^{16} eV (UHE neutrinos). Experimental upper limits on the flux of neutrinos above this energy require that a radio based detector has a volume on the order of 1000 cubic kilometers to have a significant chance of detecting UHE neutrinos. Constructing a fully instrumented detector of this volume is not economically feasible. Instead, radio based detector designs utilize dense dielectric medium with kilometer long attenuation lengths for radio propagation, such as cold Antarctic ice. This allows the UHE neutrino detector to be comprised of many relatively compact, independent stations that are separated by 1 km while still achieving the kilometer scale effective volume per detector station. Therefore, many neutrino detectors have focused their efforts on the polar regions of Earth (i.e. in Antarctica and Greenland). Further, due to relative lack of human activities, Antarctica provides a pristine radio-quiet environment which allows a radio detector to run without interference (of course, the exception is near a populated re-

search station, but even then the radio interference is far below levels found over most of the planet). For example, the ARIANNA site at Moore's Bay has been measured to have the lowest anthropogenic noise level on earth. At this site, the primary source of noise is due to unavoidable thermal motion of the electrons in the ice itself (and instrumental contributions). One consequence of this characteristic of the Antarctic environment is that detectors can operate with very low threshold requirements - typically only a factor 4 larger than the root mean square (RMS) noise value. Unfortunately, there is another source of RF noise, which arises during the relatively infrequent episodes of high winds. At wind speeds in excess of 10 m/s, it is thought that blowing snow particles will charge up surface snow and local metal towers until static discharge, creating impulsive radio noise.

It is desirable to compare the flux of neutrinos measured by independent techniques. Over much of the energy regime targeted by ARIANNA, another technique has been developed that installs antennas between 100 m and 200 m beneath the snow surface. The deep ice technique provides more volume per station, but more limited options for antenna receivers (since constrained to fit in a relatively narrow hole) and highest cost per hole. The deep ice relies on a volumetric reconstruction that differs from the ARIANNA technique that relies on area based reconstruction using directional LPDA antennas.

At lower energies, it is conceivable that radio techniques will overlap with optical neutrino detectors, especially if the next generation of larger optical Cherenkov detectors are constructed. Not only would a detailed comparison between the two detector architectures be immensely valuable in boosting confidence in the radio results, but radio could complement optical by providing better angular resolution for sources in the southern sky.

It is notoriously difficult to predict the antenna response over all angles and frequencies when it is embedded in a non-uniform medium. The upper 100 m of Antarctic ice varies in density with the largest gradients near the surface. In addition, nearby discontinuities from the air-snow boundary will create additional challenges to modeling the antenna response. The

ARIANNA station was designed to minimize many systematic issues associated with antenna responses by installing the receivers in a symmetric geometric layout. Many systematic errors associated with antenna responses are eliminated in the measurement of time delays between parallel antennas using a cross-correlation technique that requires that both waveforms show similar shapes. The antenna layout has an important impact on the resolution of measurable quantities such as angular direction of the radio pulse, the vertex resolution or neutrino angular resolution. The same argument holds for the rest of the front end signal chain such as amplifiers, cable effects, and readout electronics. The 4 fold symmetry provides two parallel measurements for two orthogonal polarization directions, minimizing the effects of systematic uncertainties in the response functions. Though the angular direction of the radio pulse can be triangulated from just three antennas, the antenna effects in mixed media near a discrete boundary must be understand with excellent precision.

An orthogonal geometry of antennas allows for the measurement of multiple polarization components and provides the ability to reconstruct the electric field. A vertically orientated dipole antenna that is at a depth of around 10 m can also provide an important measurement of a separated direct and surface reflected signal within the same time record. Timing delays between the direct and reflected signal allows for a measurement of distance to the source of the event. The timing resolution between direct and reflected signals was measured to be 100 picoseconds because the effects of the antenna model, channel to channel time delay offsets, and amplifier response is again completely removed when measured by a common antenna.

As mentioned, the density of the upper 100 m of snow surface increases with depth. To a very good approximation, the index of refraction for radio frequency electromagnetic (EM) waves increases in direct proportion. EM waves originating from within the bulk ice will refract to more horizontal trajectories. Due to the gradient in the index of refraction, EM waves will begin to travel downwards even though the initial direction is upward toward the

surface. It is not hard to see that this phenomena will restrict the geometric locations that can produce signals that reach the surface. We use the term "shadow zone" to describe the region where signals cannot propagate to the surface. To compensate for this restriction, we place the ARIANNA detector station on the surface of the Ross Ice Shelf, the largest in Antarctica and the planet. A radio detector installed on the surface of an ice shelf will observe signals reflecting off of the bottom ice/water interface, which acts as a near perfect reflector. This increases the effective volume that a detector can achieve, and allows for the detection of downward traveling neutrinos. Due to the unique feature of the ice shelf (which is a block of ice floating on water, like a very large iceberg), an ARIANNA detector can view UHE neutrinos from the entire Southern Sky. In contrast, a detector without the water-ice reflector is limited to viewing nearly horizontally propagating neutrinos. For surface detectors, the range of zenith directions is within 20 degrees of the horizon. For detectors at 200 m, the range of observable zenith angles extends to 40 degrees below the local horizon.

The Antarctic Ross Ice Shelf ANtenna Neutrino Array (ARIANNA) is a surface based radio detector that utilizes all of these design features in order to achieve excellent neutrino direction and energy reconstruction.

2.2 The ARIANNA detector

ARIANNA searches for the highest energy neutrinos (between the energies of 10^{17} eV and 10^{20} eV) through the radio signatures that they produce when they interact in the large sheets of ice found in Antarctica [34]. ARIANNA is one of three currently-operating radio based neutrino detectors in the southernmost continent, the other two being the Askaryan Radio Array (ARA) and the Antarctic Impulsive Transient Antenna (ANITA). What makes ARIANNA unique from the other two detectors is that the entire ARIANNA detector lies near the surface of the ice. By contrast, ARA [35], and it's pioneering predecessor, the Radio

Ice Cherenkov Experiment (RICE) [36], deploy antennas up to depths of 200 m at the south pole. ANITA is carried aloft by a balloon, reaching elevations around 35 km - 40 km to search for neutrino signatures that propagate from Antarctic ice into the air.

Because ARIANNA is a surface based detector, it has the advantage of being more cost efficient and easier to deploy than ARA, but comes with the disadvantage of having to understand near surface effects on antennas, and the varying ice density in the shallower regions known as the firn (see 2.7). It is also more permanent than detectors borne by a balloon, such as the NASA-sponsored ANITA project. The typical time a balloon spends in the air is about 1 month for "long duration" balloon missions in Antarctica. Also, since balloon payloads involve complicated recovery missions and often traumatic landing operations, balloon payloads typically are not flown every year. ARIANNA instruments are designed to operate continuously for a large fraction of the year, which compared to balloon borne detectors, translates to a longer live-time. ARIANNA operates on a mere five watts of power, which is readily supplied by solar panels during the sunlit summer months. During the dark winters, power is supplied by wind turbines, but there remain significant technical challenges to the goal of winter operation.

Antarctica is an ideal spot for radio neutrino astronomy mainly because of it's vast sheets of radio quiet ice, something that is hard to find elsewhere around the world. ARIANNA's main site is located at Moore's Bay on the the Ross Ice Shelf. Moore's Bay is shielded from human made radio signals coming from the nearest population center, McMurdo station, through two mountain ranges that separate the two sites which are the Minna Bluff Mountains and the Transantarctic Mountains (see fig. 2.1). Moore's Bay is in a sweet spot in the sense that it is still relatively close to McMurdo (the largest support station in Antarctica) making it more accessible, while still being sufficiently radio quite for UHE neutrino astronomy. For a thorough discussion on the noise environment at Moore's Bay see section 2.4. One major disadvantage of Antarctica is its remoteness, although an outsider would be surprised at how

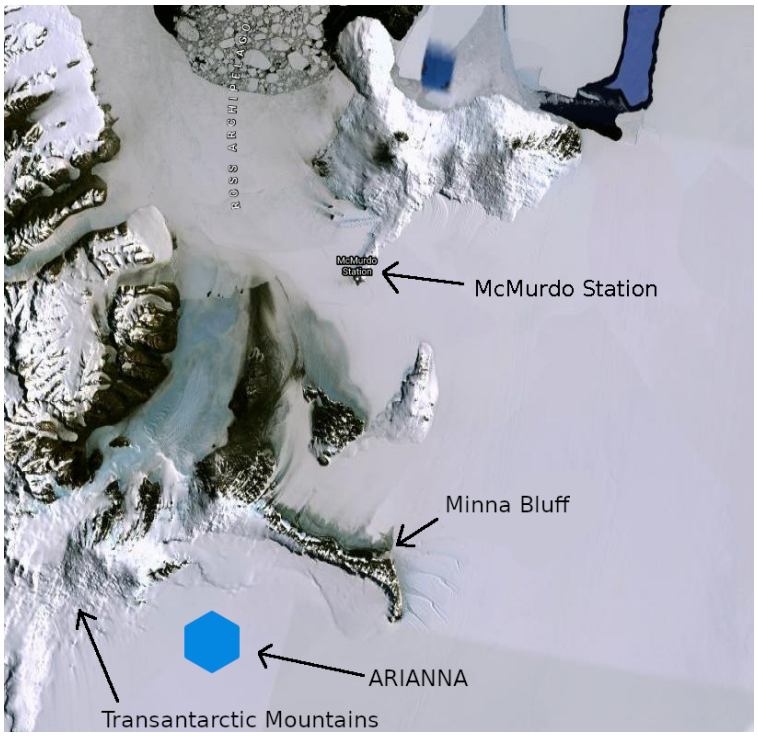

Figure 2.1: Google Maps image of the ARIANNA site located at Moore's Bay [12].

much support science receives throughout the continent.

Other experiments are submitting proposals to take part in the emerging field of radio based neutrino astronomy such as the Radio Neutrino Observatory in Greenland (RNO-G) [37], Giant Radio Array for Neutrino Detection (GRAND) [38], ExaVolt Antenna (EVA) [39], Extreme Universe Space Observatory on a Super-Pressure Balloon (EUSO-SPB2) [40], Taiwan astroparticle radiowave observatory for geo-synchrotron emissions (TAROGE) [41], and Payload for Ultrahigh Energy Observations (PUEO) [42] to name a few.

As of the year 2021, ARIANNA has nine detector stations in Moore's Bay, Antarctica, and two additional detector stations located at the South Pole, all of them are completely autonomous which makes ARIANNA easily scale-able to any number of detectors without the need for additional infrastructure such as a power grid or data grid. The electronics of ARIANNA was designed from the ground up to minimize the amount of power required for its operation. The streamlined design consumes approximately five watts of power on

average, which is readily provided by solar panels. Of course, during the winter months, the sun remains below the horizon, so the stations go into hibernation. The ARIANNA pilot program investigated a variety of wind turbines to generate power during the dark winter months, and one that was designed by our collaborators at Uppsala University in Sweden survived the harsh winter, providing power for several years. Unfortunately, wind speeds at Moore's Bay (and other places such as the South Pole) are not very high. To simplify the goal of continuous operation during the winter by wind turbines, the power consumption by an ARIANNA station was limited to 5 watts. Due to the successful operation of the Uppsala wind turbine, larger units are being fabricated to provide sufficient power throughout the winter, with the goal of reaching 80 percent operation during the winter months.

ARIANNA has recently finished her pilot phase and is working on proposals for a large scale detector that will push the limits of high energy neutrino detection. The rest of this chapter will outline the equipment necessary for a single ARIANNA station.

2.3 The Autonomous ARIANNA Station

Each ARIANNA station is autonomous, being equipped with it's own power system, communications system, set of antennas (buried near the surface), and data acquisition (DAq) electronics. Each station can independently identify neutrino events and reject background. The hardware that makes up a station acts more or less independently, making it easy to modify one piece of hardware such as antenna types, without having to also modify other pieces of hardware such as the communications or power systems. This allows ARIANNA to make variations to it's stations without having to rebuild the entire detector. For example, the ARIANNA technology can be modified to detect cosmic rays by a simple rotation of (or addition of) antennas (see section 2.5.2). This gives ARIANNA an important advantage over other detector designs by being easily accessible and modified to evolve with the science

goals.

During her pilot phase, ARIANNA consisted of ten stations at the Moore's Bay site in Antarctica, seven of which are part of the original proposed Hexagonal Radio Array (HRA). In December 2019, one of those seven had been decommissioned and returned to the University of California, Irvine. The removal of station 13 was done as a proof of concept that near surface stations can be retrieved from the pristine Antarctic environment. Two people working approximately five hours removed the station from the snow. Since surface stations can be retrieved from the snow when the science mission is complete, this reduces the environmental impact that ARIANNA has on Antarctica.

The seven original HRA stations all shared a common design, while the additional three stations at Moore's Bay were developed with new technological innovations, such as four additional antennas, for a total of eight. The added antennas provided the opportunity to vary the configuration and geometry. For example, four LPDA antennas were oriented to face upward (for cosmic ray identification) and four downward (for neutrino identification). Another variant had two dipoles within a single hole, one at a depth of 5 m beneath the surface and another at 10 m below the surface. Further, there have been two more ARIANNA detectors deployed at the South Pole which serve as a test run for a potential large scale experiment at this alternate site. In fact, the ARIANNA design can be installed at any deep-ice location around the world with little effort (see section 2.6) and because of this, the ARIANNA collaboration has flirted with the idea of setting up a station in Greenland.

2.3.1 Station Layout

The ARIANNA stations have either four antennas (HRA stations) or eight antennas, referred to as channels, which may be scaled to an even larger set in future designs. The antennas consist of log-periodic dipole arrays (LPDAs) and single dipoles orientated in a way to

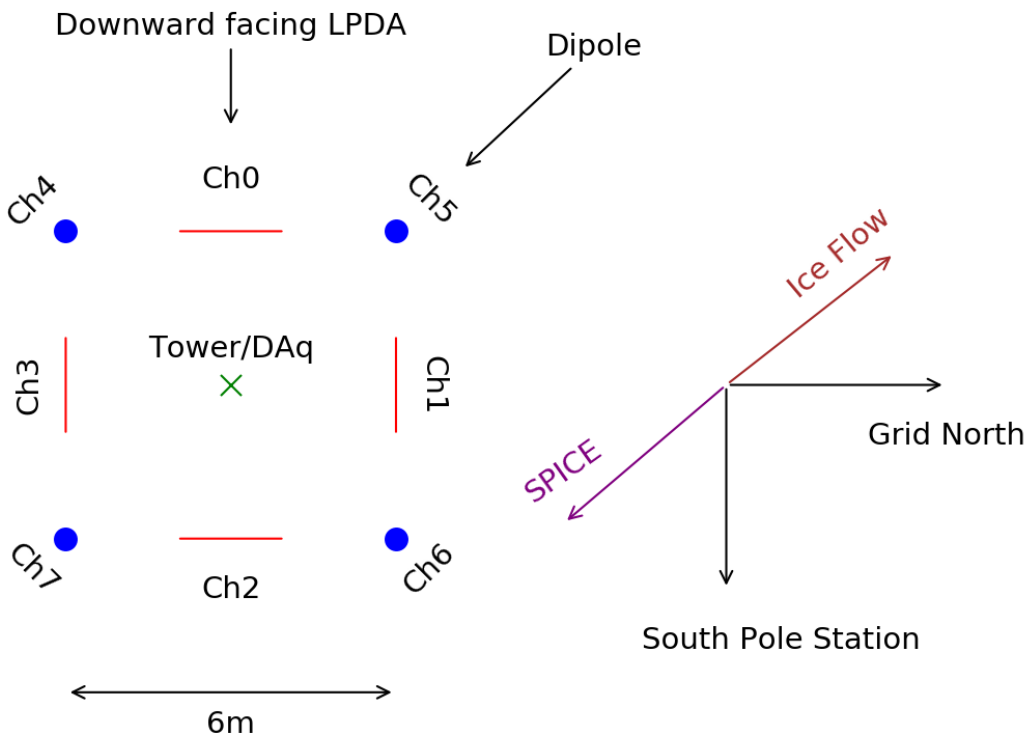

Figure 2.2: Birds eye view of Station 51 layout with direction to the residual hole from the South Pole Ice Core (SPICEcore) Project [13] and direction of ice flow. Channels 0-3 are the four downward facing LPDAs, and channels 4-7 are the four vertically-oriented dipole antennas. The angle between the ice flow and signals coming from the SPICE borehole is 1.4°, an important measurement to quantify birefringence effects. Note that these antennas are buried just beneath the snow surface.

capture multiple polarization's (discussed further in section 2.3.2). The first four channels of a typical ARIANNA station are placed at the center of each side of a square with side length 6 m. If there are eight channels, then the additional last four channels are typically placed on the corners of this square. Figure 2.2 shows a bird's eye view of an eight channel station (known as station 51).

At the center of each station is a DAq box that is split into two chambers. The main chamber, which is typically a 9 x 12 x 9 inch brazed aluminum housing, holds all of the electronics such as the mother board for each station (section 2.3.5), the two communication

radios (Iridium and Afar, see section 2.3.4), a Lithium Iron Phosphate ($LiFePO_4$) battery for storing charge, and a battery management unit (BMU) to maintain safe operational voltage in each cell of the battery (section 2.3.6). The second, smaller chamber, is usually 9 x 12 x 2 inches, bolted on top of the first chamber, and contains low-power amplifiers for each channel (section 2.3.3). The DAq box not only serves as protection for the electronics, but also provides 60dB of RF attenuation. Each DAq box is wrapped in a thermal blanket and a plastic bag before being buried in the ice for protection and insulation against the harsh Antarctic environment.

The stations also utilize a central tower to house 100W solar panels (section 2.3.6), and communication antennas (section 2.3.4). All the separate pieces of hardware are connected via coaxial cables, which range from BNC type cables to LMR type cables. Excavation of a station requires knowledge and care of where the cables are laid out, which are usually buried beneath the surface. To help aid excavation projects, ARIANNA utilized flag poles to mark key features of each station.

2.3.2 Antennas

Typically, the first four channels in an ARIANNA station are equipped with Create CLP5130-2N log-periodic dipole arrays (LPDAs) pointing downward [43]. These LPDA antennas have the length of the longest ($\frac{\lambda}{2}$) dipole at 1.45 m, and a length ratio of 0.83 for adjacent dipoles. The boom holding the dipoles in place has a length of 1.385 m, and the cable feed point is at the end with the shortest dipole referred to as the nose of the antenna. LPDA's are directional by design (see figure 2.3). They are more sensitive to signal arrival directions along the nose of the antenna, and with a polarization in the direction of the main symmetry axis of the dipoles. For the downward nose pointing LPDAs in ARIANNA, this would correspond to signals coming from below, and horizontally polarized (parallel to the surface plane of the

ice). Since there are two orthogonal horizontal polarizations that are parallel to the plane of the surface, the LPDA's are buried in two orthogonal pairs to capture each polarization.

In addition to LPDA antennas, more recent ARIANNA stations have been equipped with vertically-oriented Kansas University bicone antennas such as station 51 which contains four bicone antennas located at the corners of a 6 m square roughly centered on the station's DAq box. (fig. 2.2). The dipoles are 0.52 m in length, with the cable feed point at the top of the dipole closer to the surface. The dipoles are sensitive to signals arriving perpendicular to the main symmetry axis, with a polarization along the main symmetry axis. For the vertically orientated dipole antennas used in ARIANNA, this corresponds to horizontally propagating signals with vertical polarizations (orthogonal to the plane of the surface), which therefore captures the third polarization that the two orthogonal LPDA pairs are not sensitive to. Being able to measure the polarization is crucial for the reconstruction of neutrino properties such as direction and energy [11].

Most of the ARIANNA antennas are buried just beneath the snow surface (within 1 m from the top of the antennas), however there are some exceptions with LPDA's being placed just above the snow surface to capture atmospheric signals such as air showers produced from cosmic rays or tau double-bangs occurring from a nearby mountain (see section 2.5.3). Further, for the buried antennas, it is important to keep in mind that the surface elevation is a dynamic quantity in Antarctica, so the antennas are slowly being buried further into the snow/ice as time goes on. The snow accumulation at the surface can be accurately determined by using a heartbeat pulser and measuring the time delay between the direct and surface reflected signal in a dipole channel (see section 2.7 and figure 2.16).

To be able to reconstruct the electric field of an event, ARIANNA needs to be able to model the response of each antenna in her stations so that these can be deconvolved from the voltage traces. ARIANNA utilizes WIPL-D software [44], which is a powerful antenna simulator, able to model antennas embedded in various media as well as near interfaces.

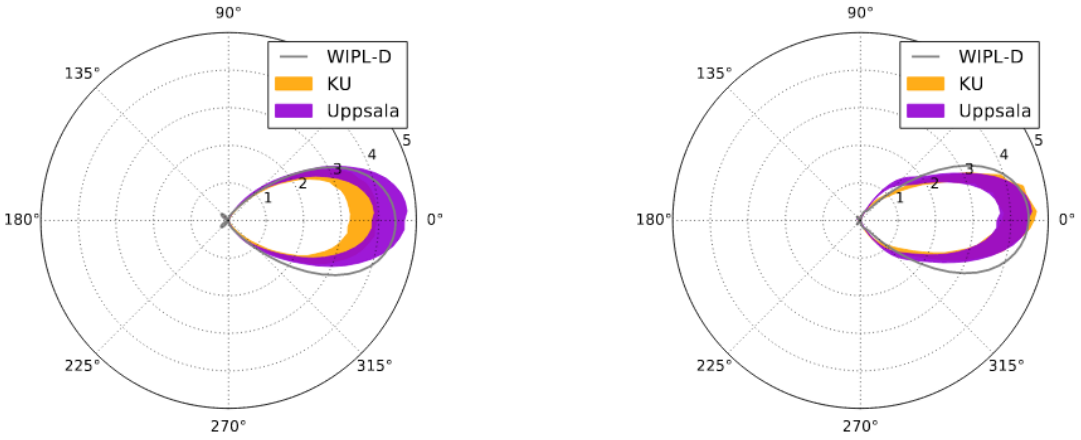

Figure 2.3: LPDA antenna response as a function of direction in the plane of the antenna tines. Left figure is at 330 MHz and right figure is at 400 MHz. The largest gain can be seen at 0° which corresponds to a signal arrival direction from the nose of the LPDA (the boom holding the dipoles in place and on the side with the smaller tines). This figure was taken from [14]

.

WIPL-D has been tested against anechoic chamber measurements performed separately at Kansas University and Uppsala University for an ARIANNA LPDA with all three responses plotted in figure 2.3 [14]. The results show great agreement between WIPL-D and anechoic data which provides confidence in the accuracy of the WIPL-D software.

An LPDA and bicone response for a particular arrival direction using WIPL-D is shown in Fig. 2.4 and Fig. 2.5. These responses are constructed for South Pole station 51 (fig. 2.2), which is conveniently placed to be able to measure *in situ* radio experiments from the nearby SPICE borehole (whose data is used to quantify the radio direction and polarization reconstruction capabilities of ARIANNA in sec 4.3). For deep pulser events in SPICE, a typical signal arrival direction at station 51 is 135 degrees in zenith and 312 degrees in azimuth with respect to grid east, and is therefore the arrival direction chosen for Fig. 2.4 and Fig. 2.5.

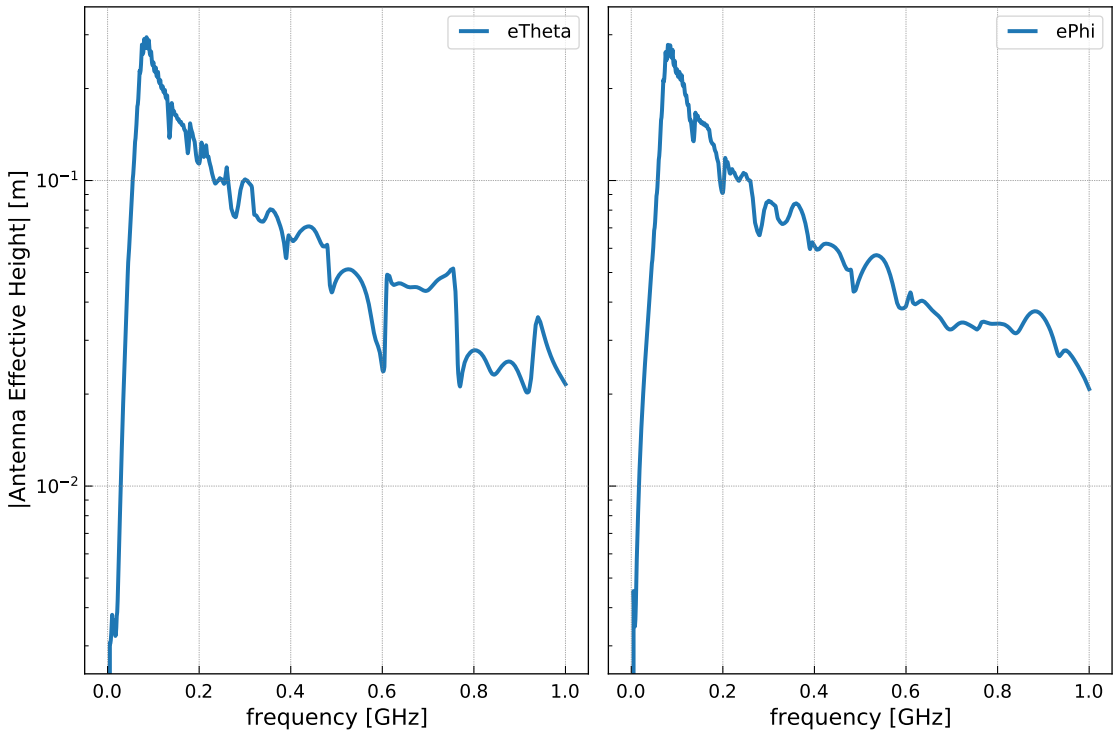

Figure 2.4: WIPL-D simulation of an ARIANNA LPDA antenna with a typical arrival direction from the SPICE borehole to ARIANNA south pole station 51. The left figure shows the antenna response to the theta polarization, and the right shows the response to the phi polarization. The LPDA antenna is orientated with it's nose pointing down (zenith at 180 degrees) and azimuth at 0 degrees which corresponds to the orientation of a typical channel 0 LPDA. The arrival direction is 135 degrees in zenith and 312 degrees in azimuth.

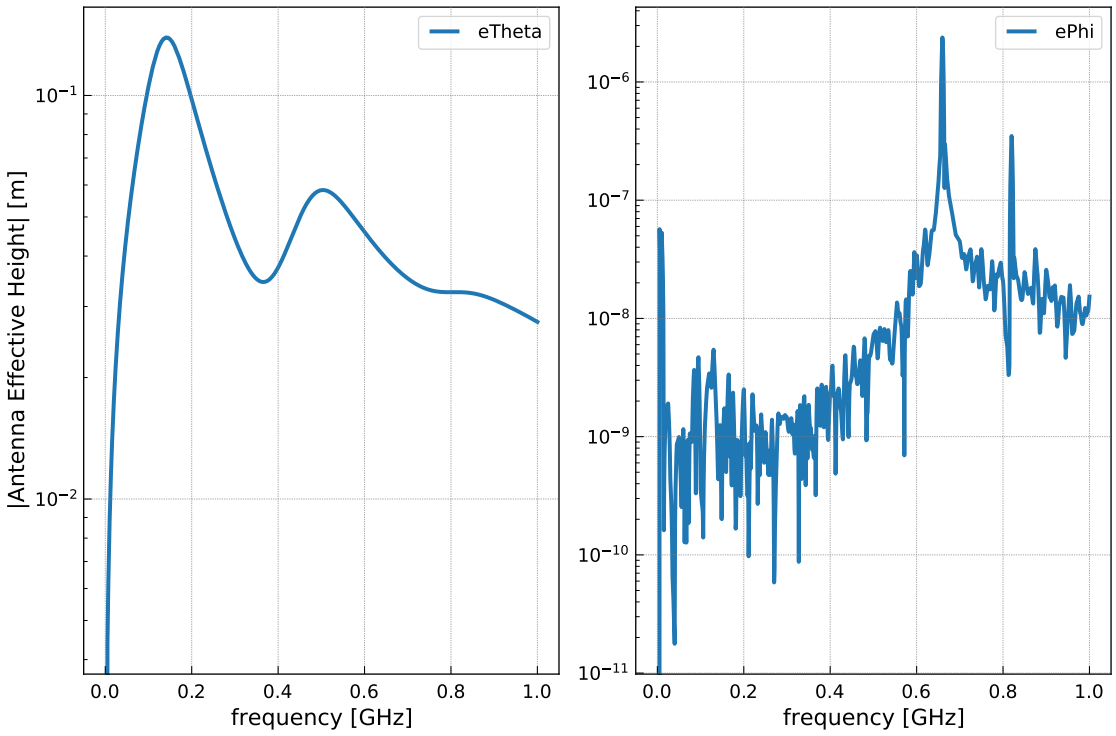

Figure 2.5: WIPL-D simulation of a Kansas University bicone antenna with a typical arrival direction from the SPICE borehole to ARIANNA south pole station 51. The left figure shows the antenna response to the theta polarization, and the right shows the response to the phi polarization. The bicone antenna is orientated with its main symmetry axis aligned vertically. The arrival direction is 135 degrees in zenith and 312 degrees in azimuth.

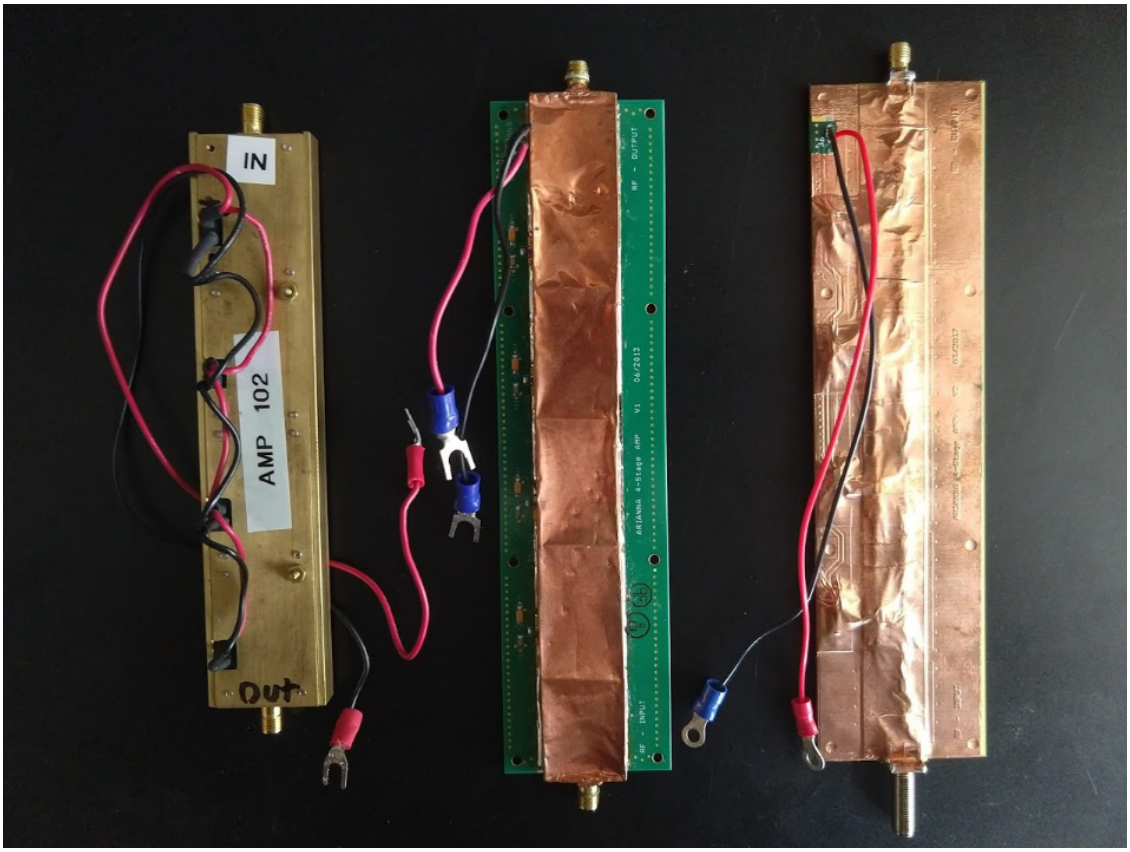

Figure 2.6: Image of the 100, 200, and 300 series amplifiers from left to right used in the various ARIANNA stations. Photo credit is given to Christopher Robert Persichilli.

2.3.3 Amplifiers

Each channel in an ARIANNA station is equipped with custom designed amplifiers by Thorsten Stezelberger at Lawrence Berkeley National Laboratory (LBNL) with production occurring in the engineering lab at the university of California, Irvine (UCI). They were designed specifically to run at minimal power, roughly 0.25 W per amp. There have been three iterations to date on the amplifier design that were deployed in the various ARIANNA stations. These are the so-called 100 series, 200 series, and 300 series amplifiers. A picture of the three different amplifier types is presented in figure 2.6. These amplifiers differ mainly by their gain. Figure 2.7 shows the gain for each of the three series amplifiers.

Each amplifier type has roughly 60 dB of gain and each individual amplifier is shielded in

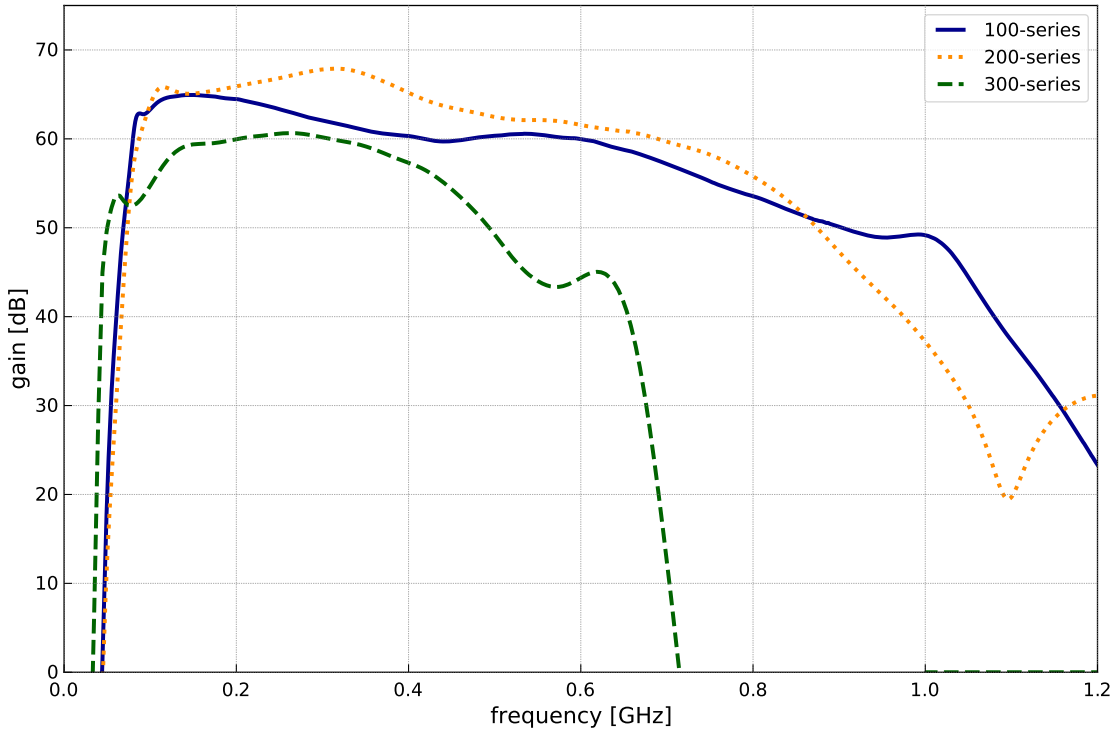

Figure 2.7: Amplifier response for the various amplifier types used in the ARIANNA stations. Blue curve is the first set of amplifiers (100 series) deployed with ARIANNA. Orange curve is the second set of amplifiers (200 series). Green curve is the third and most recent set of amplifiers used (300 series).

order to prevent cross-talk through radio frequency pickup. The 300 series amplifiers have a more narrow bandwidth, which was designed for the eight channel stations where the DAq systems operate at a 1 GHz sampling rate as opposed to the 2 GHz sampling rate used in the 4 channel stations (see 2.3.5). Each amplifier is limited to ≈800 mV to prevent damage to the DAq electronics which was accomplished through a series of RF attenuators and a 1V limiter. The 100 series amplifiers differ from the 200 and 300 series in that the attenuation and limiting was done outside of the amplifier board on the output which composed of a 3 db attenuator followed by a 1 V limiter followed by another 3 db attenuator. Further, the 100 series amplifier included a band pass filter between 100 MHz and 1 GHz which was performed on the input. All filtering and limiting was done by on-board circuitry for the 200 and 300 series amplifiers.

2.3.4 Communications

The ARIANNA stations at Moore's Bay are equipped with two modes of communication, Afar and Iridium, whereas the stations at South Pole are only equipped with Iridium due to radio noise restrictions placed on the dark sector of South Pole (the sector that the ARIANNA stations are located).

The Afar communication mode is a 2.4 GHz high speed Ethernet connection capable of transferring data at a rate of 200 kB/s. In each Moore's Bay station, the Afar router connects to a relay on the nearby summit of mount discovery or to another station's Afar router if that station's connection to mount discovery is stronger. The data is then linked to an Afar at McMurdo Station, Antarctica which in turn is connected to the internet. This communication mode is handled by an active listener script hosted by a server at UCI.

The second mode of communication is through Iridium, which is more reliable during severe weather but has a slower rate of data transfer, roughly one event every two to three minutes.

The communications are handled through the short burst data (SBD) protocol. SBD transfer is performed by sending individual 300 byte e-mail messages to an Iridium satellite that is then transferred over to UCI. This communication mode is also handled by a listener hosted on a server at UCI.

SBD sends and receives commands to the ARIANNA stations such as requesting missing files of data or changing the station's configuration. The station operates in two modes, a data taking period, and a communication period which can be adjusted in real time through the station's configuration. Typically a station is set to communicate every 30 minutes and will time out after 10 minutes if communication has not successfully finished.

2.3.5 Data Acquisition System

Each ARIANNA station has its own Synchronous Sampling plus Triggering (SST) chip which was developed by Prof. Klienfelder's electrical engineering lab at UCI. The motherboards for ARIANNA stations were designed around this SST chip which was specially made to handle a simplified calibration procedure, low power consumption, and a robust power protection [45, 46, 47]. The SST chip has a power consumption of 1.7 W.

The four channel DAq boards have a sampling rate of 2 GSa/s with a 256 sample record per channel while the eight channel boards have a sampling rate of 1 GSa/s with a 512 sample record for each channel. These two boards can be seen in figures 2.8 and 2.9. The measured voltages are held in a circular buffer and when a trigger occurs, the record is digitized by a 2.5 V, 12-bit ADC. The SST in each station is controlled by a Xilinx Spartan 4 FPGA which controls the triggering mechanism and the event readout.

The core triggering logic in the ARIANNA stations is handled in analog and generally is performed via a dual-threshold two of four majority logic trigger. The dual-threshold re-

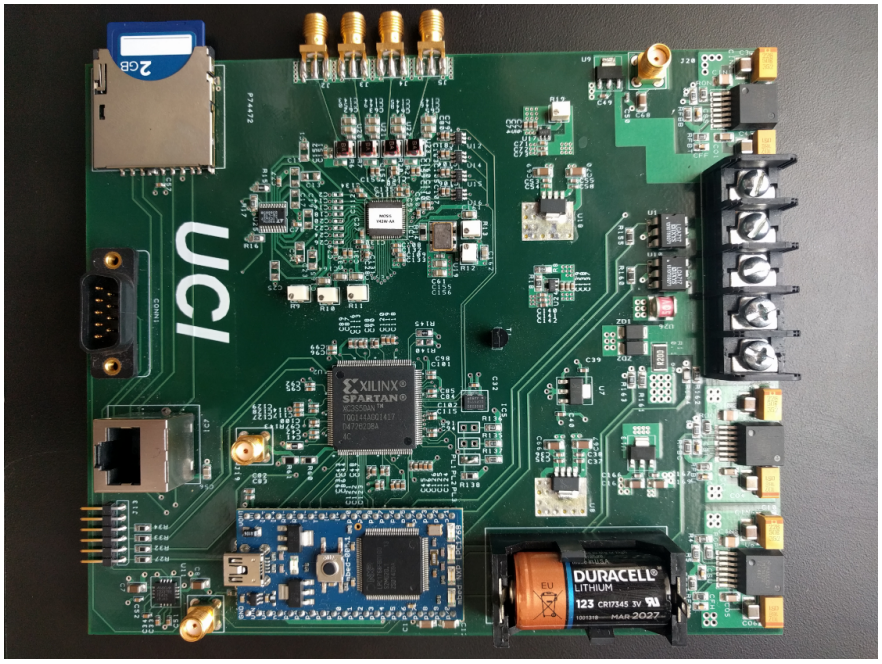

Figure 2.8: The 4 channel motherboard for an ARIANNA station.

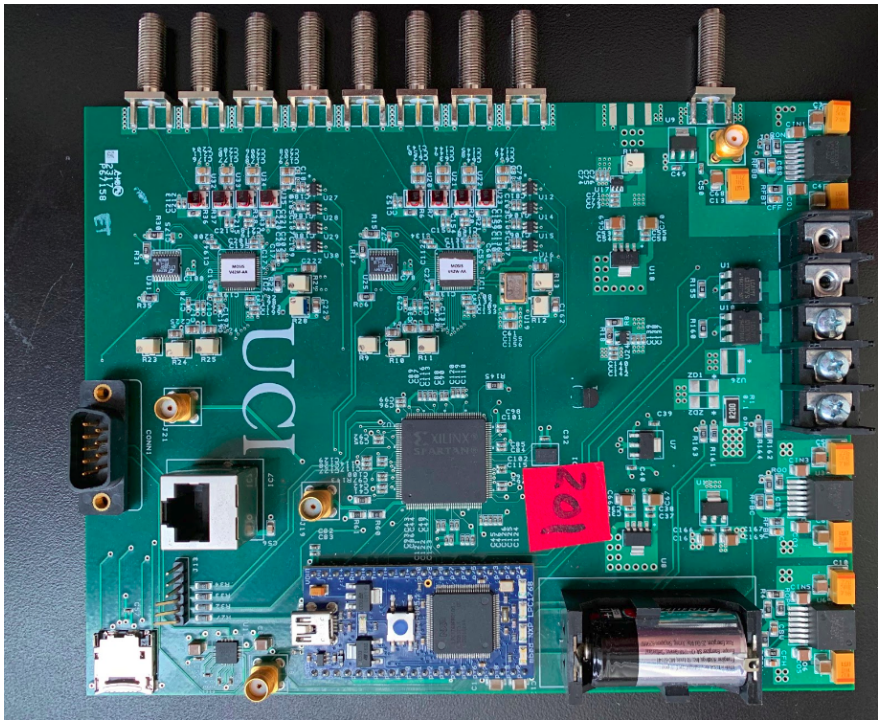

Figure 2.9: The 8 channel motherboard for an ARIANNA station.

quirement was designed by Tarun Prakash [46], and works by requiring the signal to pass both a high and low threshold within a 5 ns window, which corresponds to a signal frequency of at minimum 100 MHz, reducing the trigger rate of thermal noise. In addition to the dual threshold, ARIANNA requires that two of the four channels meet the dual threshold requirement within 30 ns of each other which takes advantage of the fact that two parallel channels with the same antenna type should see nearly identical signals. For an eight channel board, the requirement is typically restricted to the first four LPDA channels. 30 ns corresponds to the propagation time between two parallel channels with a plane wave approximation in an index of refraction of $n = 1.3$, which is 26 ns for a 6 m antenna separation. A plane wave approximation for RF signals is generally valid for sources that are much farther in distance than the separation distance between antennas, and rounding from 26 ns to 30 ns provides a buffer for this assumption. Adding this constraint significantly reduces the trigger rate of thermal noise.

Further triggering logic can be provided by a high-level control system (MBED LPC1768 micro-controller) that each station is equipped with. The MBED monitors current, voltage and temperature, sets trigger thresholds, and switches the power to the different peripherals. The most used additional triggering logic, managed by the MBED, is the L1 trigger. The L1 trigger vetoes continuous wave noise, often seen from radio communications such as from planes flying over the station. The L1 trigger works by removing signals that have a strong peak in a single frequency bin and is defined by the max power in the FFT divided by the remaining power in the FFT:

$$L_1 = \frac{max(\mathcal{V}(f))^2}{\sum_i^n (\mathcal{V}(f)^2) - max(\mathcal{V}(f))^2} \tag{2.1}$$

When L1 is greater than 0.3 the event is vetoed. This removes a fair amount of triggers on

anthropogenic noise.

2.3.6 Power

The ARIANNA stations are completely autonomous and thus each station provides its own power. The majority of the ARIANNA stations are only equipped with a 100 W solar panel which restricts the live time of each station to the austral summer period (since winter brings complete darkness). Some stations are equipped with multiple solar panels while others have only a single solar panel. The live time of each station only increases marginally when including additional solar panels. This is because a single 100 W solar panel is sufficient to power a station during the summer months, and additional solar panels only help during the relatively shorter transitions between summer and winter.

ARIANNA station 15 located at Moore's bay, Antarctica, is also equipped with a wind generator constructed by Uppsala University in Sweden. The wind generator is still in an iterative phase to maximize livetime during the austral winter season of Antarctica where there are periods of high winds with no sun light. Preliminary versions have proved reliable livetime of around 23 % during the austral winter.

In addition, each station contains a 20 Ah battery composed of 36 ($LiFePO_4$) cells (arranged into 4 series of 8 cells each), which was constructed by A123 systems. Each of the 4 series in the battery has a nominal voltage of 3.3 V making the overall nominal battery voltage 13.2 V. The battery boosts the livetime of each station by allowing the station to operate during insufficient periods of sunlight or wind. For example, when the sun starts to set, the solar panels no longer provide continuous, all day power to the stations. During this period, the solar panels provide enough power to charge up the battery for a fraction of each day, and the battery is sufficient to power the station for the rest of the day.

The power to the station is handled by a Texas Instruments bq40z60EVM charge controller referred to as the battery management unit (BMU). The BMU is configured to manage the power supplied to the DAq electronics while maintaining a safe operational voltage for the battery. When the solar panel or wind generator no longer provides sufficient power to the station, the battery will kick in until the voltage across one of the 4 cells in series drops below a cutoff voltage to prevent hysteresis loops in the BMU. The BMU also maintains equal voltages across each of the 4 cells in the battery

2.4 Background Noise

Moore's Bay is an excellent site for the main ARIANNA array because it sits in a valley created by the two mountain ranges, the Minna Bluff Mountains and the Transantarctic Mountains, which provides shielding from human made radio signals coming from the nearest population center, McMurdo station. A measurement of the atmospheric noise near the surface within the bandwidth relevant for an ARIANNA station is shown in figure 2.10. This measurement is pessimistic as it uses a directional antenna placed above the surface and pointed at McMurdo station. From figure 2.10, it can be seen that the biggest source of noise from McMurdo at Moore's Bay originates from communications. Further sources of noise include the very few aviation flights flown over Moore's Bay and from the ARIANNA team itself during onsite maintenance periods which include *in situ* experiments and communications. Some natural sources of radio background include cosmic rays, auroras, and the Galactic plane, which are therefore necessary for ARIANNA to be able to distinguish from neutrinos. An example of a cosmic ray signal seen in an HRA station (four channels of downward facing LPDA pairs) is shown in figure 2.11 which was taken from [14]. Cosmic rays are perhaps one of the most problematic background sources as they have similar signatures to what neutrinos would produce. However, simple pointing should be able to break

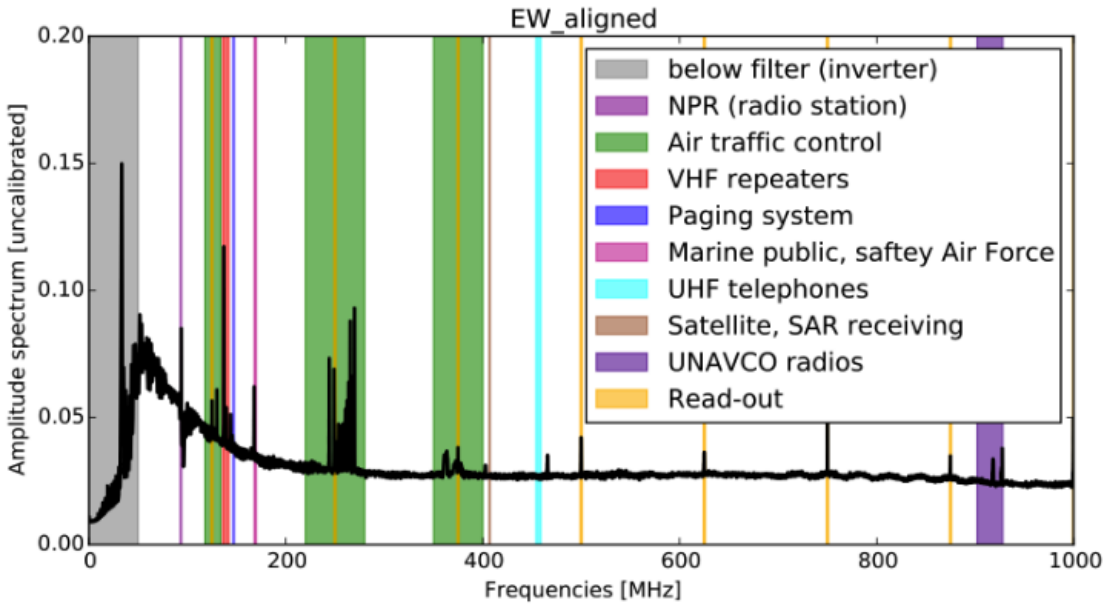

Figure 2.10: Background noise at Moore's Bay measured with an ARIANNA LPDA antenna (see section 2.3.2) and a 4 gigasample per second oscilloscope. The directional LPDA was pointed at McMurdo station above the snow surface and thus is an overly pessimistic estimate of the background events that a buried ARIANNA station might see. Taken from [15].

this degeneracy by determining if the signal is coming from below (neutrino radio signal) or from above (cosmic ray radio signal). Some newer ARIANNA stations have been equipped with upward facing LPDA antennas that are sensitive to down going cosmic rays in order to better quantify this background (see section 2.5.2). A lot of the other noise sources have narrow band signatures unlike the characteristic broadband neutrino signal and therefore the ARIANNA L1 triggering scheme can be used to eliminate these (see section 2.3.5).

2.5 Station Variations

2.5.1 South Pole Stations 61

Station 61 is unique in that it has six LPDA antennas, two of which are above the surface and pointing up in order to scan the sky for cosmic rays. The first four channels are the

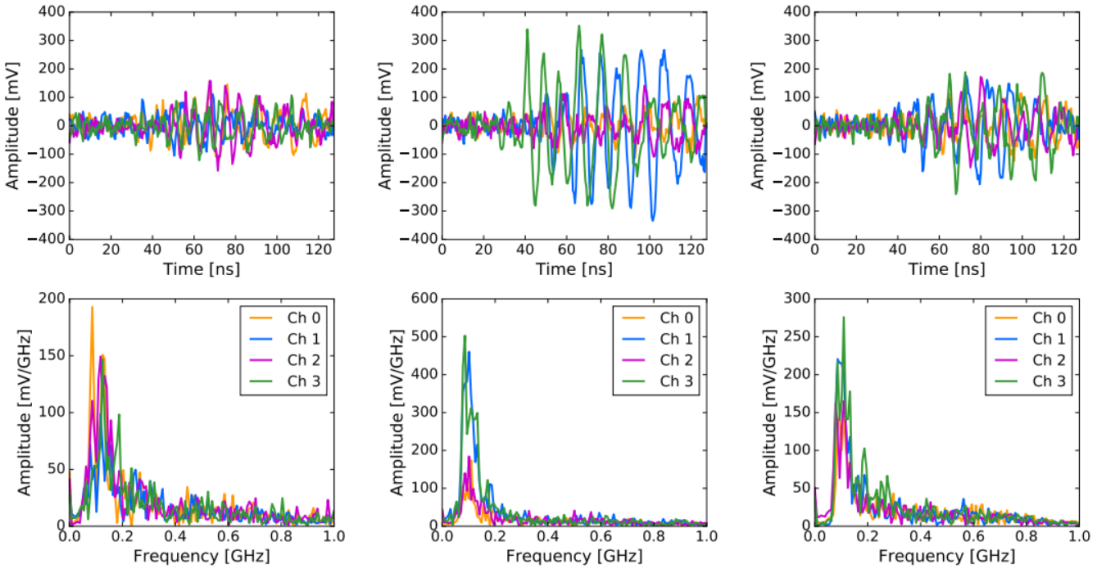

Figure 2.11: Three cosmic ray events seen in an ARIANNA HRA station which was tagged by time coincidence with a cosmic ray event seen in a dedicated cosmic rays station. Top row shows waveforms as a function of time and bottom row shows the corresponding frequency spectrum. Taken from [14]

nominal four LPDAs orientated at the center of the edges of a 6 m square. Additionally, there are two dipoles installed just beneath the surface to capture the vertical polarization of RF signals. A schematic of station 61 can be seen in Figure 2.12.

2.5.2 Cosmic Ray Station

One of the hardest backgrounds to distinguish from a neutrino is a cosmic ray. They both have very similar radio signatures. Luckily, cosmic-ray signatures will almost certainly be coming from above the detector and neutrinos from below. So by having a dedicated set of antennas that are sensitive to downward going signals, ARIANNA can apply a veto mechanism to look for signals that dominate in these antennas and flag them as cosmic rays. LPDA antennas are not sensitive to signals coming from the back lobe, and therefore can be used as directional antennas. The original ARIANNA cosmic ray station used 4 LPDA antennas with the nose pointing upwards in order to be sensitive to cosmic rays. This station

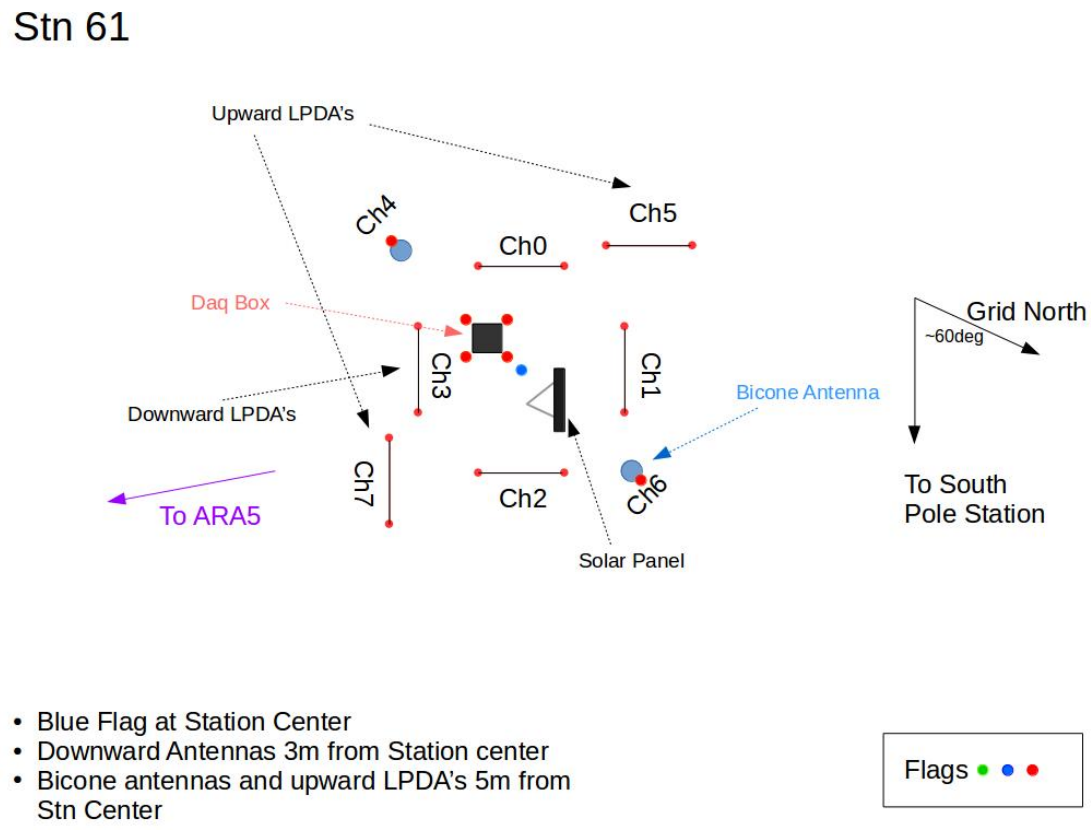

Figure 2.12: A layout of station 61 at the South Pole. Credit is given to Christopher Robert Persichilli for making the figure.

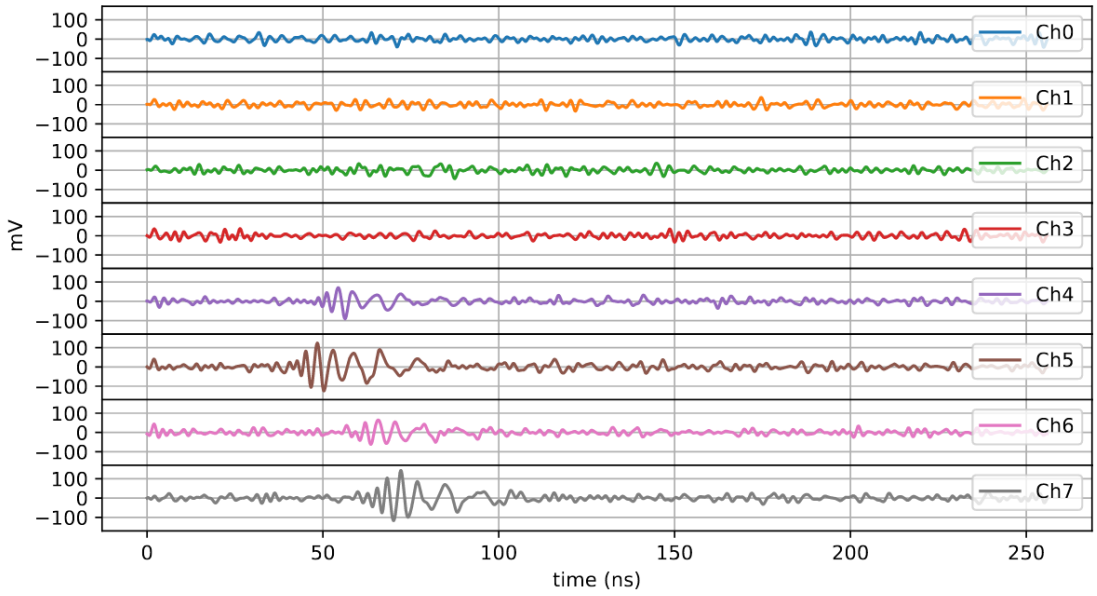

Figure 2.13: A cosmic ray event seen in a dedicated eight channel ARIANNA station. Channels 0-3 are downward pointing LPDAs, where as channels 4-7 are upward pointing LPDAs. Taken from [15]

has since been modified with an additional 4 LPDA antennas that are pointing down into the ice to model what a neutrino station might see with a set of dedicated upward facing LPDAs. The idea is to test the directional abilities for vetoing cosmic rays in an LPDA. A cosmic ray signal should be dominant in the four upward facing LPDAs while being unseen in the downward facing LPDAs. This idea can be seen in the example cosmic ray event, triggered by this station, shown in figure 2.13.

2.5.3 HCR Station

The Taiwan Astroparticle Radiowave Observatory for Geo-synchrotron Emission (TAROGE) has used the ARIANNA station design as a prototype to finding tau neutrinos (ν_τ) [48]. The idea is to use the ARIANNA system, with a series of LPDA antennas above the surface, mounted to a tower, and pointing towards a mountain range, to look for air showers produced through a tau double-bang process. This process can occur when a ν_τ interacts within the

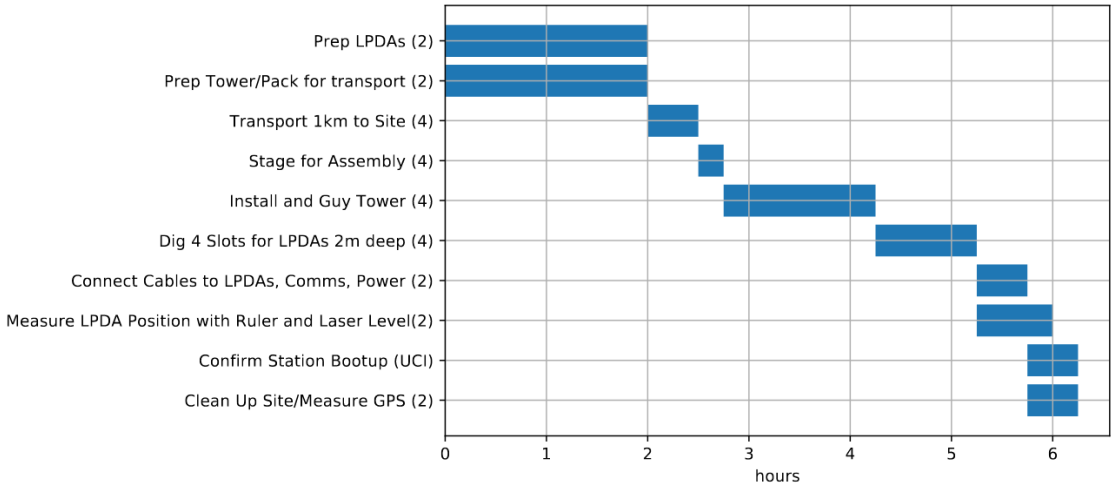

Figure 2.14: Gantt chart of installing a 4 channel station at Moore's Bay with a four man team. The numbers on the y axis represent the number of people involved in that particular task. Taken from [15].

nearby mountain to produce a secondary tauon, which then decays and produces air showers that have a radio signature.

TAROGE has a dedicated station in Moore's Bay called the Horizontal Cosmic Ray (HCR) station. The station originally used a 4 channel board with 4 LPDA's, but has since been upgraded to an 8-channel board with 8 LPDA's utilizing an additional polarization measurement for better azimuth reconstruction.

2.6 Deployment

Each ARIANNA detector can be placed essentially anywhere around the world with arguably little effort. ARIANNA has utilized this idea to establish a couple detectors at the South Pole. There is also ongoing discussion of deploying a station in Greenland. Through my own personal experience, a station can be fully deployed and operational within roughly six hours utilizing a four-man team with hand tools (see Gantt chart in figure 2.14).

2.6.1 The pilot Array in Moore's Bay

The ARIANNA pilot phase began deployment in 2012 with it's final season in 2018. The first 3 stations of the original 7 station array was deployed in 2012, with the remaining 4 deployed in 2014. Since the ARIANNA station is modular and self contained, three additional stations were added in Moore's Bay for further testing, making a total of 10 stations at Moore's Bay. ARIANNA has also deployed 2 additional stations at the South Pole, one in 2017 and another in 2018. In 2018, I had the honor of leading the ARIANNA Antarctic expedition, which included station maintenance, *in situ* horizontal propagation measurements, and installing a second South Pole station. The ARIANNA team replaced solar panels and BMUs, upgrading station 52's antennas, and dismantling station 13 as a proof of the minimal impact that the stations have on the Antarctic environment. The tower containing the solar panels and communication antennas was removed and the DAQ box was removed. Due to the 4 m depth of the LPDA and coax cables, they were difficult to retrieve, and remained in the snow.

2.7 Ice Properties

The Antarctic ice is an essential part of the ARIANNA detector. It is where a neutrino interaction will occur, and the resulting radio signal will propagate through to one of the detectors. The ice will affect the shape and amplitude of the signal. Therefore, it is crucial to be able to understand the impact of ice on radio signals. The propagation of the RF pulse depends on properties such as density variations with depth, reflection layers, snow accumulation, and ice attenuation. Uncertainties in these properties limit the reconstruction capabilities of the ARIANNA station.

2.7.1 Density Profile and Reflections

For dielectric materials such as snow and ice, the signal speed is determined by the local index of refraction (n), and can be approximated with a linear relation to the specific gravity by the Schytt model (see eq. 2.2) [16, 49].

$$n \approx 1 + 0.78\frac{\rho}{\rho_{ice}} \tag{2.2}$$

Where n is the index of refraction, b is a constant equal to 0.78 for ice, and ρ is the specific gravity with ρ_{ice} being the specific gravity of solid ice. The specific gravity of ice is reasonably expressed as an exponential form via equation 2.3

$$\rho(z) = \rho_{ice} + (\rho_0 - \rho_{ice})e^{-z/z_0} \tag{2.3}$$

Here, ρ_0 is the specific gravity at the surface, z is depth and is negative below the surface, and $z_0 = g\chi_0\rho_s$ is a constant that depends on gravitational acceleration, and the density/volumetric compressibility of snow. Because of the linearity between density and index of refraction, equation 2.3 can be reworked to express the index of refraction as a function of depth as in equation 2.4.

$$n(z) = n_{ice} - \Delta n e^{\frac{z}{z_0}} \tag{2.4}$$

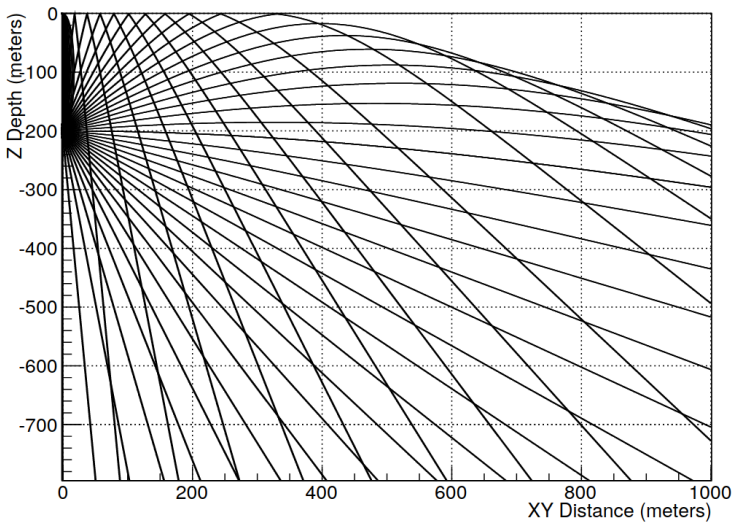

Figure 2.15: Ray tracing solutions for various launch angles with an emitter located at a depth of 200 m. The shadow zone is represented as the solid white region in the upper right of the figure, where ray bending creates a blind spot in the ice. A receiver at a distance of 800 m and a depth of 100 m would not trigger off of this emitter from classical ray tracing. In the presence of impurities around 100 m, reflection layers could result in horizontally trapped rays that could alleviate the blind spot for this receiver. Taken from [16].

Where n_{ice} is equal to 1.78 which is the index of solid ice, and Δn is the difference between the index of solid ice and at the surface.

The relevant depths for equation 2.4 are the upper 60 m in Moore's Bay, and the upper 200 m at the South Pole which has a mixture of snow and ice known as the firn. The index of refraction below the firn is nearly constant at 1.78. Since the density increases with depth, the wave speed therefore decreases with depth resulting in curved trajectories following Fermat's principle. For transmitters/receivers deployed on or near the surface, sufficiently large horizontal propagation angles may be refracted downwards before triggering the receiver. These regions are known as shadow zones and limits the effective area that a detector can survey. Figure 2.15 highlights this concept.

Unlike the South Pole, Moore's Bay is located on an ice shelf and therefore the bottom most layer of the ice shares a boundary with liquid water. Since solid ice is substantially denser than liquid water, a vast majority of incident angles will totally internally reflect back up

through the ice. This increases the effective volume of an ARIANNA detector as it can now detect signals that are traveling downward into the ice through their reflection back upward.

Further, local impurities in the density profile may cause local reflection layers that can trap light horizontally through total internal reflection known as horizontal propagation, and can break some of the blind spots from the shadow zones. The results of horizontal propagation has been studied and is reported in [16].

2.7.2 Snow Accumulation

The surfaces of Moore's Bay and the South Pole are constantly rising. Moore's Bay is located at an accumulation zone and the ARIANNA site there sees roughly a rise of 0.6 m per year due to snow. The South Pole gets roughly one foot of snow accumulation yearly. These changes are important to understand for antennas near the surface, where boundary effects aren't negligible. This typically means that the modeled antenna response will improve with time as the antennas become buried deeper into the ice and the hard to model boundary effects become minimized.

Snow accumulation can be measured by an ARIANNA detector with an additional dipole attached to the heartbeat pulser technology that each ARIANNA SST board is equipped with. By emitting a heartbeat pulse at a reasonable distance from the detector and measuring the time delay between the direct and surface reflected pulses in a dipole channel, one can determine the local changes in the surface elevation.

One such station equipped to measure snow accumulation is station 52 at Moore's Bay. Station 52 has a heartbeat dipole located 40 m away from the station center and at a depth of 15 m, along with a dipole channel located at depths of 20 m. This is sufficient separation to capture the direct and reflected pulses without interference.

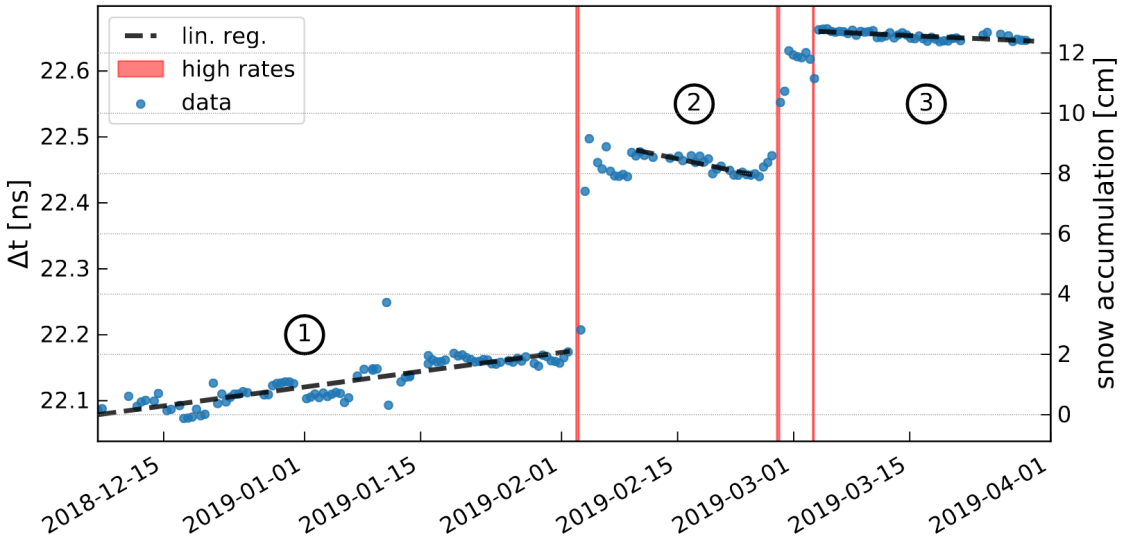

Figure 2.16: Snow accumulation measurements through the time differences from direct and reflected pulses. The relation between the time difference and the snow accumulation is shown on the left and right axis. The red zone highlights regions of extended high trigger rates which is an indicator for a stormy period. The black dashed line shows the linear regression of the blue data points. The long time periods between storms are labeled by the circled number in each region. Taken from [17]

The heartbeat pulser can be activated remotely and was set to run at 0.5 Hz every 12 hours for 5 minute periods from December 2018 to April 2019. Figure 2.16 shows the results of snow accumulation using this technique. The estimated precision of this technology is on the order of millimeters, a competitive resolution to other techniques for measuring snow accumulation [17].

2.7.3 Ice Attenuation

RF signals in ice are thought of as isotropic radiators. Using geometry in 3 dimensions, the power of an RF signal that is isotropic falls off with distance, r, as $\frac{1}{r^2}$ and because power is proportional to the square of the amplitude, the amplitude falls off with distance as $\frac{1}{r}$. Therefore it is important to be able to measure the propagation distance from the source to the detector if one would like to make a measurement of the amplitude or energy of the

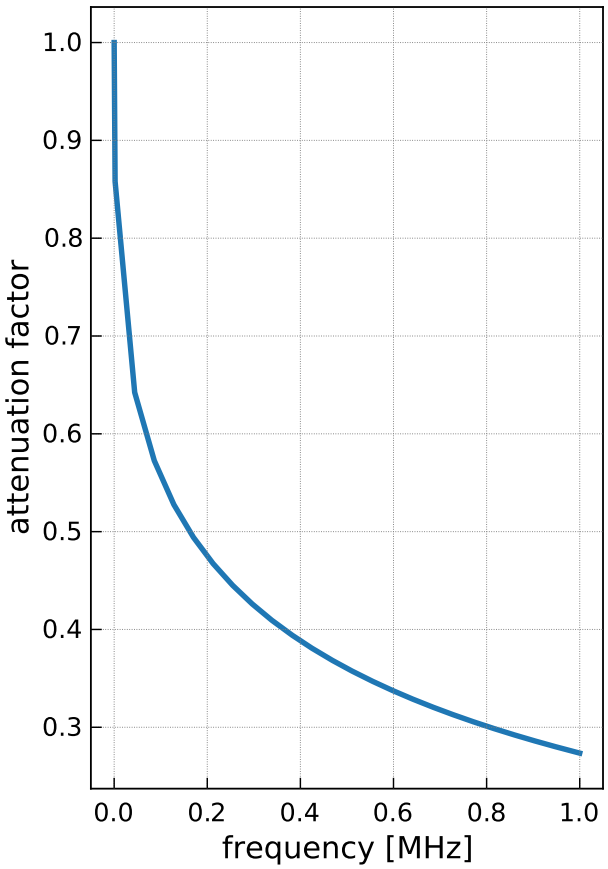

Figure 2.17: Frequency dependent ice attenuation factor for an emitter at 1200 m depth and 653.8 m away from ARIANNA station 51 at the South Pole. This attenuation was used in the construction of figure 4.10.

signal at the source. This is ultimately important for backtracking the signal energy from a detector to measure the neutrino energy.

The ice itself also provides frequency dependent attenuation for RF signals. This attenuation was quantified through RICE data gathered in 2004 [16]. An example of the attenuation factor for the relevant frequencies in an ARIANNA detector, and using a transmitter at the South Pole SPICE hole with a depth of 1200 m and ARIANNA station 51 as the receiver is shown in figure 2.17. This particular setup was chosen as it corresponds to a launch angle of 30 degrees which is one of the anechoic chamber measurements taken for this transmitter and also is the attenuation used to create the electric field comparison in figure 4.10.

2.8 Future Outlook

The ARIANNA design has proven to be cost and time efficient, along with achieving excellent reconstruction abilities such as neutrino direction and energy. The surface design has had a huge impact on ARIANNA's accomplishments. A surface station is easier to deploy and takes less resources, but also antennas that are buried near the surface can detect surface reflected signals or firn refracted signals. Time delays between primary and secondary pulses can be used to measure vertex distance with competitive precision. The ARIANNA LPDA antennas are great directional antennas and are sensitive to a broader range of frequencies than a dipole. LPDA's are awkwardly shaped and therefor it only make sense to be deployed in a shallow station. All of these advantages of a shallow station have been heard and accepted by the scientific community. The IceCube Gen2 proposal is pushing a hybrid design of hundreds of stations in square lattice. Alternating layers of the lattice will either be comprised of entirely a shallow station or a combination of shallow and deep stations.

Chapter 3

ARIANNA Software

ARIANNA uses two main coding environments for studying radio based neutrino detectors. Both of them are publicly available on Github [50, 51]. The first is so-called NuRadioReco [21], which is a framework used to process and analyze events that triggered a detector (see section 3.1). The second is titled NuRadioMC [8], which is a Monte Carlo simulation framework used to produce event data sets such as a large set of neutrino signals (see section 3.4). These two frameworks have been designed with a large emphasis on modularization, making them flexible to a wide range of studies. For example, in NuRadioReco, the detector description has been completely separated from the rest of the framework, which has the great benefit of generalizing NuRadioReco to be used to analyze any radio based detector, not just an ARIANNA surface station.

Both of these frameworks are used in this thesis to make a prediction of the resolution on neutrino direction which requires a measurement of the radio signal direction, polarization, and viewing angle along with the ice profile for in ice detectors (see equation 1.8). NuRadioReco was adapted to process and study *in situ* data which resulted in the quantification of the RF direction and polarization resolution for an ARIANNA detector [52]. Viewing

angle reconstruction is not as easy to study because we can't generate an Askaryan like pulse in an *in situ* measurement (i.e. emission on a Cherenkov cone and with the right frequency spectrum). So to quantify the viewing angle reconstruction, the Monte Carlo simulator, NuRadioMC, was used to simulate hundreds of UHE neutrino events that triggered an ARIANNA detector. These simulated events were then processed using NuRadioReco with a dedicated module that I had constructed, resulting in a prediction of the viewing angle resolution and ultimately the resolution on neutrino angular direction and energy.

This chapter first provides a general discussion of how NuRadioReco and NuRadioMC is structured, and follows up with the specific modules in each framework that are important for the analysis of this thesis. The results of these analyses are discussed in chapter 4 and chapter 5. Further, the steering scripts for using these two frameworks along with other useful tools for the ARIANNA detector have been grouped into an open sourced Github repository called ARIANNAanalysis [53]. The details of this repository are discussed in the appendix.

3.1 NuRadioReco

NuRadioReco tackles the generalization of event reconstruction to any radio based neutrino or cosmic ray detector through separating the code into three branches which are the detector description, event data, and the processing modules. The event data and detector description are completely decoupled and only indirectly communicate through processing modules. This provides the ability to use identical processing modules in order to compare an event triggered by different detector designs. Scientist who try to study differences between say deep and surface stations obtain a more direct comparison when utilizing the structure of NuRadioReco where differences due to software implementation is removed.

The framework of NuRadioReco is written in python to keep the difficulty of installation across various platforms to a minimum. Python is a scripting language meant to read like a book. Using python simplifies data analysis and visualization, however for large systems, python under performs compared to other high-level programming languages such as C. To enhance the performance of NuRadioReco, numpy [54] objects are used when applicable. Numpy is a python package that improves performance because the software is written in C and then wrapped in python. It often runs multiple sub tasks in parallel, and forces arrays to have specific data types which makes the memory storage more compact.

NuRadioReco strives on having a diverse set of input modules, allowing different file formats to be read such as the raw ROOT files of an ARIANNA detector, and also comes with it's own file type with the extension of ".nur". Nur files are great to work with, they require no additional software to be installed and the events can be saved at any step during the data processing. This greatly improves the time-efficiency as some modules only need to be performed once such as the RF direction reconstruction. NuRadioReco also provides the ability to view the reconstructed data on a web server utilizing python's Dash package to create responsive and customizable web servers [55].

3.1.1 Detector Description

The detector description needs to be able to support all relevant details of the detector required for event analysis such as the antenna responses, positions, and orientations. Also, ARIANNA stations often get hardware upgrades such as new antennas and amplifiers in order to study and meet new science goals. So each autonomous station needs to have its own time dependent detector description in NuRadioReco. This is done using a MySQL database with a hierarchical structure.

Each detector such as ARIANNA has a table of the individual stations, which include all the

details of that station such as installation date and location, except for the details about the channels. The channels are stored in a separate table and linked to each station through a station id. Each channel has it's own cable, antenna, and amplifier which are further stored in their own tables and referenced through a channel id. Separating these components into their own tables is less prone to bugs. In particular, a lot of channels use the same amplifier or antenna properties, and therefore, a lot of channels reference the same row of the respective tables. Changes or improvements on the amplifier or antennas description will only need to be made once in order to effect all channels linked to that respective piece of hardware. This is not only time efficient, and clean, but reduces human error. If only a single channel needs to be updated, perhaps through the installation of an entirely new antenna, there is flexibility in making a channel specific row for that antenna, or any other components linked to that channel.

MySQL is an online database, so this process requires an internet connection, which can be slow, and is limited in the number of simultaneous queries. This was taken into consideration during the initial construction of NuRadioReco and resulted in two methods to get around these disadvantages. First, the database is buffered at the beginning of execution so that multiple readings of the detector do not correlate with multiple queries of the MySQL database. Second, there is an option to convert the MySQL database to a JSON file for complete offline analysis. The conversion requires an Internet connection, but after this, the entire detector description will be saved locally. This is convenient, however the online database insures everyone pulls from the most up-to-date layout and therefore it is recommended to use the online database over locally saved detector descriptions.

MySQL is a great tool for storing and sharing detector descriptions with many clients. The database does not get modified during queries, and so there is no worry in corrupting a stations configuration. If temporary adjustments need to be made to a detector description, NuRadioReco is capable of modifying the buffered detector during execution of the code.

This allows for testing systematic uncertainties such as antenna positions, and orientations.

3.1.2 Event Data

NuRadioReco has dedicated methods for reading in various data files. These methods convert input data into a customized event data structure native to NuRadioReco. This limits the amount of differentiating code between unique research groups as only the conversion method needs to be constructed in order to utilize the processing modules within NuRadioReco.

The event data structure is built into three layers. It is expected that a neutrino event for the ARIANNA detector would only trigger a single station within the hexagonal lattice of stations with a primitive length of 1 km. However, multiple stations may trigger if the neutrino has high enough energy or if a tau double-bang is observed (see section 2.5.3), and also is the case when detecting UHE cosmic rays. Therefore, the first layer in the event data structure is the event as oppose to being a station. The station sits at the second layer as each event has the option to contain numerous stations. Each station is comprised of many antennas, and so the final layer of the event data structure is the channel layer. A triple loop across these three layers is sufficient to gain access to all the information stored in a set of events.

An outline of the event data structure is presented in figure 3.1 which was taken from [21]. Each layer of the data structure contains extra attributes that are most relevant at that layer such as the event id, or the trigger type for that station. Further the station objects can contain a simulated station that acts similarly to a station object on it's own but has prepopulated fields due to the event coming from a simulation rather than a deployed detector. The simulated station is a great tool for research and development, allowing measurements on the reliability of processing modules within NuRadioReco.

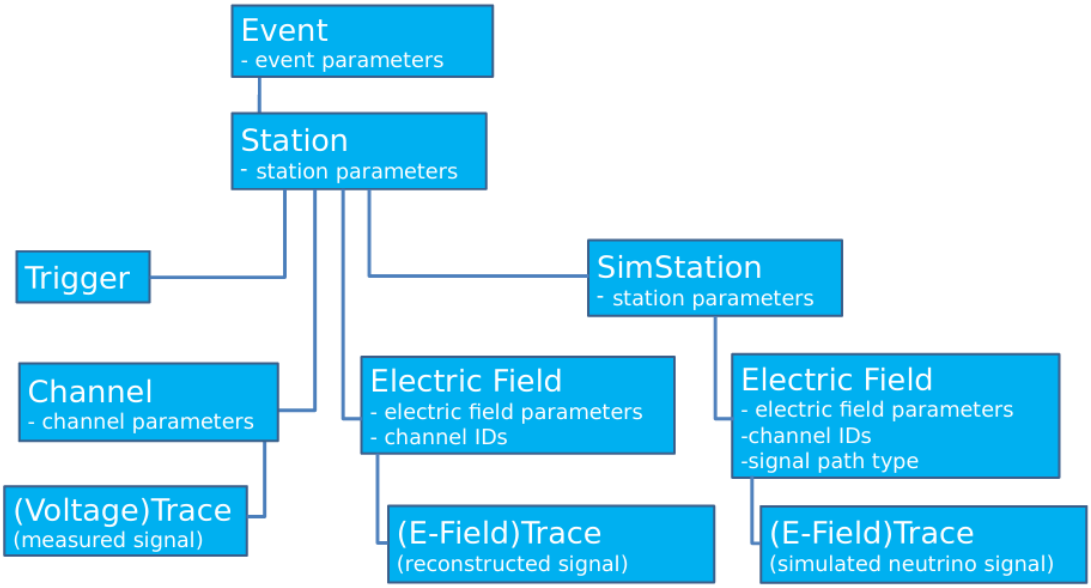

Figure 3.1: Event data structure, which can contain multiple stations, each with a detector description from either true events or simulated events and further breaks down into the channels for each station.

3.1.3 Processing Modules

The event reconstruction is split into numerous modules that work independently from each other. Each module is set up as it's own class, with a constructor, begin, run, and end methods. The constructor is used to create the module instance, while the begin method initializes any constants throughout the event reconstruction such as input files or a debugging state. The run method is executed on an event by event basis, whereas the end method can be used to deconstruct the module after the last event.

Reconstructing an ARIANNA event with NuRadioReco is like reading a book. The modules are performed in sequence, each with a name matching it's implementation. The typical modules used to process an ARIANNA event in this current research utilizes the following:

1. **channelStopFilter:** At the beginning and end of each ARIANNA event, there is a glitch caused by the stop signal in the electronics. The channelStopFilter smoothly

filters the beginning and end of each trace with a tapered cosine window to remove this glitch.

2. **channelBandPassFilter:** The frequency content of the events can be restricted. The input accepts a filter type and a pass band making the module highly general. A band pass filter can be great for reducing out-of-band noise.

3. **hardwareResponseIncorporator:** This module deconvolves out the gain and phase from the amplifier responses associated with each channel within a station. Further, it removes time delays due to each channel's cable lengths. Since each detector may utilize different types of hardware, this module is detector specific so that each detector type requires it's own module to factor out the hardware specific responses of that detector.

4. **channelSignalReconstructor:** Computes and stores the basic signal properties such as maximum voltage, and signal to noise ratio. Having a module for this reduces bugs between different researchers as they all utilize the same method to calculate their signal quantities, and any bug fixes will be propagated to everyone's work.

5. **channelResampler:** NuRadioReco is equipped with up and down sampling capabilities. This can be used to provide a more precise measurement of the time delay between multiple signals, which would normally be limited by the original sampling rate of the data. Down sampling is provided to reduce the file sizes after correlations and study single channels with the precision at which it was recorded.

6. **channelTimeWindow:** In addition to a frequency dependent band pass filter, NuRadioReco has a dedicated module for a time filter. This additional filter is useful when correlating signals between channels because it allows the isolation of a main pulse. This isolation reduces correlations on noise and also for example between one primary and one secondary pulse.

7. **correclationDirectionFitter:** The correlation direction fitter is used to predict the

arrival direction of the triggered event. This procedure is discussed in more details in section 3.2 as it is the core method in finding the RF angular direction and further in quantifying it's resolution.

8. **voltageToEfieldConverter:** This module factors out the antenna response from the signals which reconstruct the electric field. This is the key method for making a polarization measurement and therefore it is discussed in the dedicated section 3.3.

9. **electricFieldBandPassFilter:** In NuRadioReco, an electric field is treated as an independent data structure from the voltage traces mainly because the electric field is a vector and therefore requires a three dimensional array of traces to represent and often the number of electric fields per event does not correlate with the number of channels in the station due to either a centrally defined electric field, or multiple signals contributing to a particular voltage trace. It was decided to be more readable if there was a separate band pass filter method built specifically for the electric field data structure in NuRadioReco. The electric field band pass filter reduces noise influences on electric field properties such as a polarization measurement.

10. **voltageToEfieldAnalyticConverterForNeutrinos:** This module contains a minimization method for reconstructing the neutrino angular direction and energy given the ice profile, Askaryan parameterization, and band pass filter. Details of this method are discussed further in section 3.5.

3.2 Direction Reconstruction using NuRadioReco

The angular direction of an incoming radio signal can be computed by comparing the time delays between different antennas to theory. The theoretical expectation is found purely from geometry and the assumption of a plane wave, which is sufficient for the typical source

distances to an ARIANNA station along with the compact arrangement of the ARIANNA antennas. Given a particular arrival direction, time delays between antennas are calculated using the speed of light in some medium such as ice and finding the path length differences between each antenna. Going through a set of input arrival directions, and performing a chi-squared minimization between the true time delays and the best theoretical time delays, allows for the reconstruction of the radio signals angular direction.

The module that performs all of this in NuRadioReco is called the cross correlation method. This name is suiting as the time delays that are minimized on are found by correlating traces from parallel channels together, which should see identical signals. This requires multiple channel pairs in order to break degeneracies produced from just a single pair. For example, a signal arrival direction of 45 degrees in azimuth, and 135 degrees in zenith (180 degrees is arriving from directly below the detector), will give the same time delay as an arrival direction of 135 degrees in azimuth, and 135 degrees in zenith. Having an additional channel pair, that is orthogonal to the first pair, provides the determination of a single zenith and azimuth solution.

This method relies on an accurate ice profile (see section 2.7) because the ice profile dictates the propagation paths of the ray tracing solutions. Further, the antenna positions, orientations, and cable delays need to be known with sufficient precision and accuracy. Uncertainties in any of these parameters will add to the uncertainty in the time delay which can become the bottle neck in the RF direction resolution of that particular ARIANNA station. One advantage of this method is that uncertainties in the antenna response cancels out because of the use of identical parallel antennas. Another source of uncertainty on the angular direction arises from the choice of minimization. The scipy [56] optimize package with method brute is used, which essentially loops through a range of input angles and returns the closest match. Therefore, the precision is only as good as the step size in the minimization input. The brute method provides an option to use a finisher method in order to polish the global

minimum originally found from the grid input. The particular finisher method used is the fmin option provided by the scipy package [56]. Of course the input grid could simply be made to be finer, but the cost is in time efficiency and it can quickly become a problem when working with a large set of events. The analysis of the RF direction resolution is presented in chapter 4.

3.3 Polarization Reconstruction using NuRadioReco

To measure the polarization, a detector needs to be able to measure the electric field using at least two perpendicular antennas. ARIANNA utilizes two pairs of orthogonal LPDAs to achieve this. Having performed the required measurements, the voltageToEfieldConverter module is then used to reconstruct the electric field. This is performed by solving the following system of equations which relates the electric field $\mathcal{E}^{\phi,\theta}$ to the voltage output $\mathcal{V}_i$ of an antenna i in Fourier space as:

$$\begin{pmatrix} \mathcal{V}_1(f) \\ \mathcal{V}_2(f) \\ ... \\ \mathcal{V}_n(f) \end{pmatrix} = \begin{pmatrix} \mathcal{H}_1^{\theta}(f) & \mathcal{H}_1^{\phi}(f) \\ \mathcal{H}_2^{\theta}(f) & \mathcal{H}_2^{\phi}(f) \\ ... & \\ \mathcal{H}_n^{\theta}(f) & \mathcal{H}_n^{\phi}(f) \end{pmatrix} \begin{pmatrix} \mathcal{E}^{\theta}(f) \\ \mathcal{E}^{\phi}(f) \end{pmatrix}, \tag{3.1}$$

$\mathcal{H}_i^{\theta,\phi}$ represents the response of antenna i to the θ and ϕ polarization of the electric field, $\mathcal{E}^{\theta,\phi}$, arriving from a particular direction and therefore it requires that first the angular direction of the signal be reconstructed. The polarization states, θ and ϕ, are the two orthogonal vectors in spherical coordinates that are perpendicular to the signal propagation direction. For a horizontally propagating signal, $\vec{e}_\phi$ lies in the horizontal plane whereas $\vec{e}_\theta$ is oriented

vertically. Once the electric field is reconstructed, the polarization is then calculated via:

$$P = \arctan\left(\frac{f_\phi}{f_\theta}\right) \tag{3.2}$$

with,

$$f_\phi = \sqrt{\sum_{t=t_m-35\,\mathrm{ns}}^{t_m+35\,\mathrm{ns}} |E_\phi(t)|^2} - f_{\phi,\mathrm{noise}} \tag{3.3}$$

where f_ϕ is the energy fluence for the ϕ component, E_ϕ is the electric field for the ϕ component in the time domain, and P is the polarization. The time t_m is the position of the maximum of the Hilbert envelope of the dominant component of the electric field. The θ component of the energy fluence is defined analogously. The quantity $f_{\phi,\mathrm{noise}}$ is an estimate of the noise contribution which is calculated from a part of the recorded trace that does not contain signal. This definition is general and robust against different experimental configurations such as anechoic chamber data taken from an oscilloscope or ARIANNA data collected from the SPICE *in situ* experiment (see section 4.7), and can also be directly applied to a neutrino event. The analysis of the polarization resolution is presented in chapter 4.

3.4 NuRadioMC

Radio based neutrino experiments are still in the development years. In order to have any significant chance of detecting a neutrino, a full scale experiment of 200 surface stations will have to be realized [32]. However, many questions need to be addressed in order to plan for a large scale experiment such as the neutrino direction and energy reconstruction capabilities of a single station and what modifications should be made to improve these measurements.

Some of these questions can be partially answered through *in situ* measurement campaigns, but to get a fully detailed picture, a large data set of neutrino events is necessary. The only way this can currently be achieved is through a Monte Carlo simulation. NuRadioMC does exactly this. Similar to NuRadioReco, NuRadioMC is completely modularized and is built to work hand in hand with NuRadioReco. For example, the detector setup of NuRadioReco is used in NuRadioMC during the triggering and ray tracing stages, and the resulting voltages, and electric fields for each event are stored as a .nur file ready to be processed using NuRadioReco. NuRadioMC splits the Monte Carlo modeling of neutrino detection into four independent models, the so-called four pillars [8]. These include event generation, signal generation, signal propagation, and detector simulation.

Separating these four stages has many benefits. One is that it takes many neutrino events in order to get a single detection, and therefore the neutrino event generation can take much longer than the rest of the simulation. By generating the neutrino events separately and then storing this in an HDF5 table, allows this process to run a single time, and provides a data set that can be used for multiple detector setups, ice profiles, neutrino parameterizations, triggering methods, and so forth. For a more detailed discussion about NuRadioMC, see [8]
.

3.4.1 Event Generation

The event generator creates a specified number of neutrino interaction vertices within some set volume and with a set energy range. The output is a HDF5 file that contains all the relevant properties for neutrino detection. The earth becomes opaque for UHE neutrinos, and therefore neutrinos with arrival direction from below the detector have a smaller likelihood of reaching the ice and creating a shower versus neutrinos coming from above. To account for this, neutrinos are first simulated with an equal probability within the specified volume, and

then the output includes a weight that is based off the probability of the neutrino reaching the simulation volume. The neutrino and anti-neutrino flavors are simulated with equal probability according to the general understanding of neutrino production in sources [8, 57]. Further, the probability of a charged current versus a neutral current interaction is dictated by the ratio of $CC : NC$ 0.7064 : 0.2936 according to the CTEQ4-DIS cross sections for neutrino energies between 10^{16} eV and 10^{21} eV [58].

3.4.2 Signal Generation

The signal generation performs the shower physics and creates the appropriate Askaryan signal. The shower physics can be simulated though either a frequency-domain parameterization or through semi-analytic calculation each retrievable with a dedicated function. For example, the spectrum produced from the Alvarez 2000 parameterization [18] can be specified given the shower energy and the viewing angle that the radio signal makes relative to the shower axis. Therefore, one can determine the viewing angle and shower energy by performing a chi-squared minimization against this parameterization (see section 3.5). Figure 3.2 shows how the Alvarez 2000 parameterization depends on the viewing angle for 10^{18}eV neutrinos for both hadronic and electromagnetic showers (taken from [8]).

3.4.3 Signal Propagation

The signal propagation module is essentially the ray tracing code used to find the path that the Askaryan signal would follow to reach a particular antenna. This includes ice effects such as the bending of the signal in the firn, and the frequency dependent ice attenuation. There can be many ray tracing solutions per antenna each with different viewing angles depending on the geometry. For example, a surface reflection or refraction provides a second ray tracing solution, and at Moore's Bay, where bottom reflections become important, there

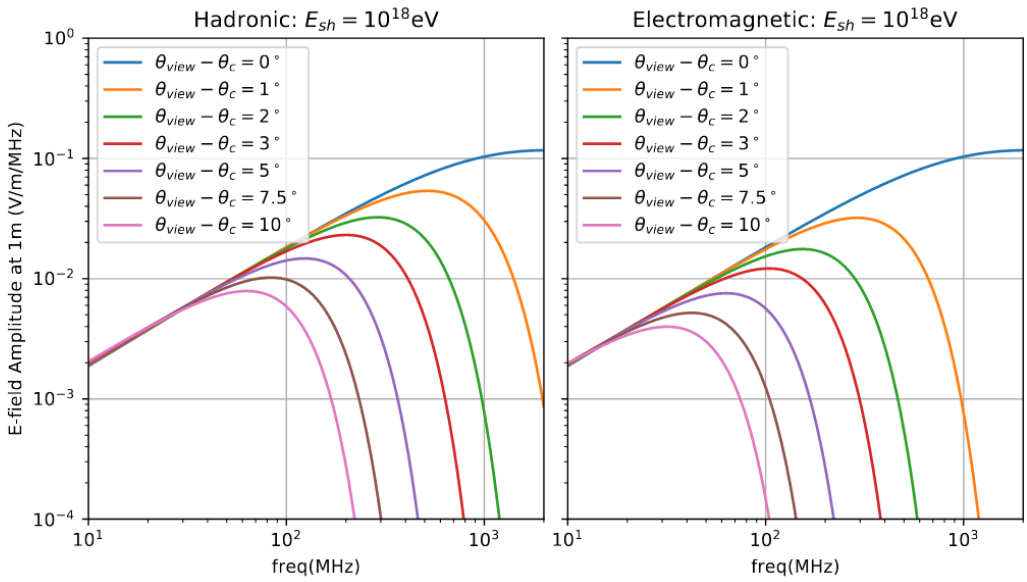

Figure 3.2: Frequency spectrum of an Askaryan signal for 10^{18}eV neutrinos when viewed at different angles relative to the Cherenkov cone using the Alvarez 2000 parameterization [18]. The left plot shows the dependence for hadronic showers, and the right plot shows the dependence for electromagnetic showers. Taken from [8].

can be more ray tracing solutions through multiple reflections between the surface and the bottom layer. The ray tracing module provides solutions for each channel separately, and stores information such as the launch directions and viewing angles for each solution within each channel.

3.4.4 Detector Simulation

The detector simulation takes the electric field at each receiver and applies a triggering mechanism to determine if that event will be stored. If the signal triggers the detector, then it undergoes a convolution with the detector response such as the antennas, amplifiers, and cables. The detector simulation works coherently with the detector description used in NuRadioReco (see section 3.1.1). For example, the same antenna models stored in NuRadioReco are used to determine the antenna response for various arrival angles. The event that is ultimately saved is stored in a .nur file with the same data structure as a real event

would have in a particular detector design and includes a simulated station for comparing reconstruction procedures with the simulated values. The compatibility between NuRadioMC and NuRadioReco allows for straight forward analysis of simulated data with new modules developed for processing real data.

3.5 Neutrino Direction and Shower Energy Reconstruction using NuRadioMC and NuRadioReco

To understand the neutrino direction and shower energy reconstruction capabilities, a large neutrino event set is produced using NuRadioMC. Then a dedicated module was constructed to determine these quantities. Given a neutrino event, the subject is placed through a complex minimization similar in design to that for the cross correlation method (see section 3.2). The brute force method is used again with the fmin finisher function. The input is a grid of possible neutrino azimuth and zenith directions along with a range of shower energies.

Before the minimization begins, predefined ray tracing solutions, which only depend on the antenna's locations and the neutrino vertex location, need to be determined. The vertex position is only weakly dependent on the neutrino direction and energy reconstruction. The Neutrino vertex position can be found using a combination of the the Direct and Reflected (D'n'R) technique [17] to measure the distance, and the RF angular reconstruction to determine the direction. The D'n'R technique measures the time delay between a direct and surface reflected or refracted signal measured within a dipole. The correlations between time delay and distance is stored in a table for each vertex direction. The vertex direction can be found with high precision when having an accurate ice profile, and good RF angular direction measurements. Once the vertex position and the ray tracing solutions have been solved, the minimization process can be executed.

The minimization method utilizes a forward folding technique which prevents issues from deconvolving antenna responses arising from directions with little sensitivity. These directions have extremely small gains, and the deconvolution process divides the frequency amplitude by these tiny numbers, amplifying noise and resulting in poor electric field reconstructions. To fix this, as the name suggests, electric fields are first predicted through simulated or semi-analytic methods, and then are convolved or forward folded with the detector antenna layout for comparison with the true voltages of the event.

The minimization process works by simulating the voltage traces that would be seen given a detector description and a neutrino direction and energy as input, then minimizing this against the true voltage traces of a particular event. The following steps are taken for each iteration of the minimization function:

1. A for loop is performed through each antenna

    1.1. A second for loop is used to capture each ray tracing solution for a particular antenna

        1.1.1. The polarization is calculated from the neutrino direction, and the RF signal launch direction by equation 1.1

        1.1.2. The viewing angle is also calculated by definition to be the angle between the RF signal launch direction and the neutrino direction.

        1.1.3. The shower energy, and viewing angle are then used to get the frequency spectrum of the RF signal at the vertex position through some parameterization such as Alvarez 2000 [18] or Alvarez 2009 [59].

        1.1.4. Frequency dependent ice attenuation is applied and the resulting spectrum is convolved with the polarization to get the theta and phi components of the electric field at the antenna.

        1.1.5. Reflection coefficients are taken into account if applicable.

        1.1.6. The electric field is then convolved with the antenna response.

        1.1.7. Additional time delays are added based off differences in antenna positions and cable delays.

    1.2. The option for a band pass filter can be applied after all the ray tracing solutions have been factored in for a particular channel.

2. There may exist a global time offset between the reconstructed and true voltage traces which is found through correlating the channel with the largest signal to noise ratio and then shifting the reconstructed traces accordingly.

3. Finally a chi-squared value is calculated across all channels with equal weight.

This process takes the question of viewing angle resolution and puts it all together with the polarization and RF direction, along with ice effects, to make an overall resolution on the neutrino direction and energy. The analysis of this is presented in chapter 5.

Chapter 4

Polarization and RF Direction Reconstruction

In order to find the resolution that a surface based neutrino detector can achieve on neutrino direction, a measurement of the radio signals angular direction, polarization, and viewing angle is necessary (see eq. 1.8). This section will present results from SPICEcore studies to quantify the angular and polarization resolution of radio signals using the ARIANNA detector [52]. There were previous efforts by the ARIANNA group to quantify the angular and polarization resolution of radio signals either by bouncing signals off of the bottom of the ice sheet in Moore's Bay or by analyzing cosmic ray data. The SPICE data serves as a more realistic setup with a range of incoming arrival directions and vertically polarized signals. The two previous studies will be briefly described first.

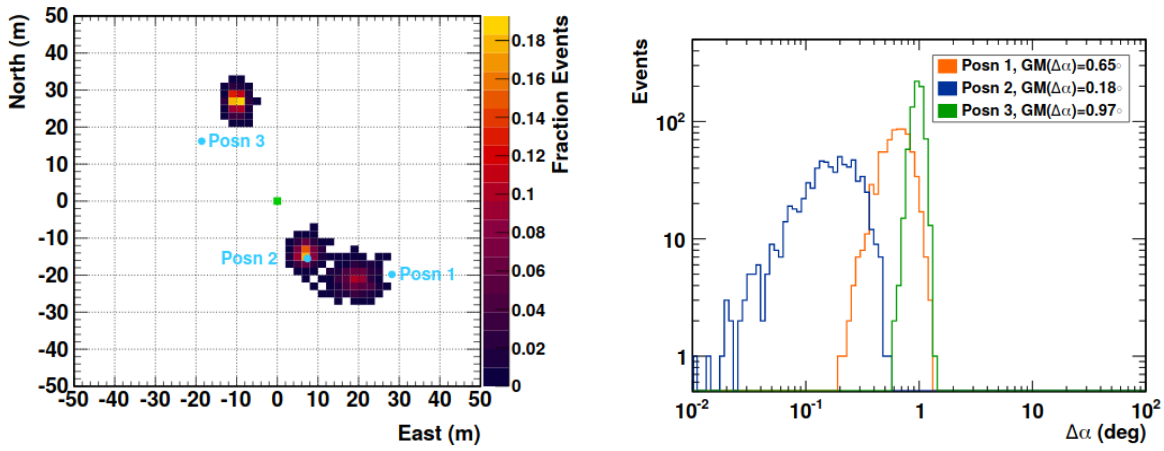

Figure 4.1: Adapted from [19]. Left figure shows three separate test locations (blue dots) where a transmitter was placed. The green dot represents the receiver (an ARIANNA station). The colored blobs are the reconstructed transmitter locations. The right figure shows the angular deviation from the true position to the reconstructed position. The legend shows the geometric means for each of the three test locations.

4.1 Bounce Signals

The angular and polarization reconstruction accuracy of the ARIANNA station has been studied previously for the stations on the Ross Ice Shelf [60]. Calibration transmitter antennas buried slightly below the ice surface emitted radio pulses toward the bottom water-ice interface at Moore's Bay. The absolute measurement of the arrival direction of the reflected signal agreed with expectation to within 1 degree or better (see figure 4.1 [19]). Reflected signals also demonstrated that polarization of the electric field was preserved during propagation and reflection [60]. Though these studies were encouraging, they were mostly confined to nearly vertical propagation. The new data presented in this chapter extends those prior studies to include a range of more representative propagation directions for neutrino-induced radio signals.

4.2 Cosmic Rays

Another test of the angular and polarization reconstruction was performed with ARIANNA by observing cosmic rays [20]. Cosmic ray interactions in the atmosphere generate radio pulses, which are well-understood (e.g. [61, 62]). Hence, such cosmic rays act as an in-situ calibration source. These signals are more representative of neutrinos than the previous study in that the signal-to-noise ratio and frequency-content are neutrino-like. The pulse forms are very similar; air showers and in-ice particle showers both produce short bipolar pulses with frequencies of order $\mathcal{O}(100\,\mathrm{MHz})$. Those ARIANNA stations configured with upward-facing LPDAs reconstruct the polarization and direction of incoming radio pulses over a much broader range of incoming angles and physical conditions than the previous study (see also [11, 20]). A newly developed forward folding technique was used to reconstruct the 3 dimensional electric-field pulse from the measured voltages [21]. Figure 4.2 was taken from [20] and presents the reconstructed polarization with a resolution of 7.06° around the theoretical expectation [11, 20]. That study uses signals from the air, which excludes any effects from the ice. ARIANNA searches for neutrinos coming from the ice, however, and thus a test of the effects of the ice is crucial.

4.3 SPICEcore Measurements

The new data used for an updated radio signal angular direction and polarization measurement was collected by the ARIANNA South Pole station named station 51 during the last week of December, 2018. The signal transmitter (IDL-1 pulser [63]) was connected to a bicone antenna which was lowered to a depth of 1.7 km inside the SPICE hole and was vertically-oriented (to match the form-factor of the SPICE hole) [13]. The IDL-1 pulser broadcasts short duration radio frequency pulses through the bicone antenna with a repeti-

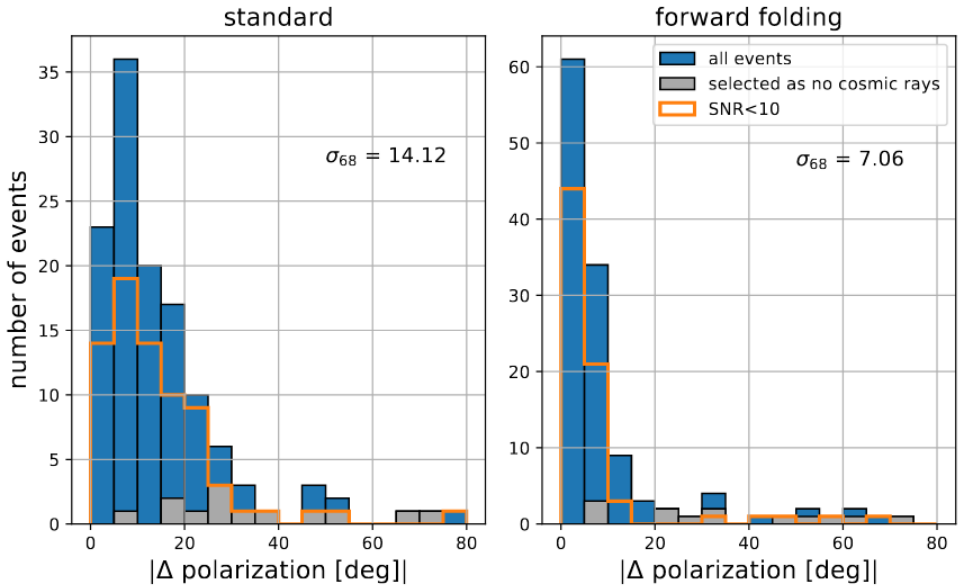

Figure 4.2: Taken from [20]. Distribution of reconstructed polarization of cosmic ray data from ARIANNA detectors compared to expected polarization. (Left) determines the polarization from the electric fields found by deconvolving out the ARIANNA antennas, (right) determines the electric field through a forward folding technique [21]. The blue data represents the set of cosmic ray candidates, which is was not optimized for purity. Therefore, some events that were selected by eye are highlighted in grey, and the measurement of the 68% quantile does not include the grey events.

.

tion rate of 1 Hz, which is then detected by the ARIANNA station. Several thousand pulser events were directly transferred over the Iridium satellite network for offline analysis of the angular and polarization reconstruction capabilities of ARIANNA.

The characteristics of the signal transmitter were tested in an anechoic chamber and combined with simulations of the known ice effects on signal propagation from transmitter to receiver in the SPICE run [8, 16]. This allows for a comparison between the expected and reconstructed electric fields.

4.3.1 Geometry Between SPICE Hole and ARIANNA Station at South Pole

Station 51 is located roughly 1 km from South Pole Station and 0.65 km from the SPICE hole. Recent data collected by Emilie Sinkler and Delia Tosi in 2020 reports that a tilt of the SPICE hole starts to occur at a depth of 1 km [22]. The radio signal's angular reconstruction results are first presented assuming no tilt in the SPICE hole as was reported in [52] and then an update on the radio signal's angular direction with the tilt profile measured in 2020 is discussed in section 4.6. The results of the tilt profile improve the angular reconstruction results minimally. Uncertainties in the SPICE hole translates to a systematic uncertainty in the relative position of the emitter with respect to the detector station, which in turn results in a systematic uncertainty in the predicted signal arrival direction. Station 51 is equipped with eight antennas, four LPDAs and four bicone antennas (See section 2.3.2 for details on the antennas). A layout of station 51 in provided in Fig. 2.2 of chapter 2.

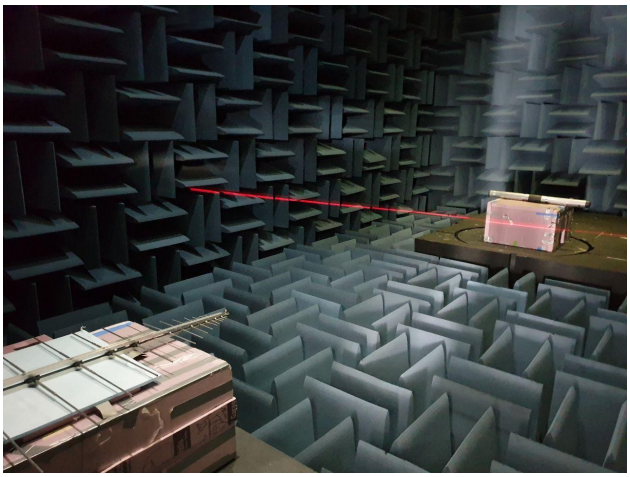

Figure 4.3: Photo of the anechoic chamber experimental setup. The transmitting bicone antenna was rotated horizontally. The receiving LPDA antenna was orientated in two ways for every measurement. The first orientation being what is shown in the photo (tines laid horizontally), and the second orientation had the tines vertically oriented which was stabilized with foam bricks.

4.3.2 Anechoic Chamber Measurement of Signal Emitter

The IDL-1 pulser with the same bicone antenna used in the SPICE measurements, and an ARIANNA LPDA receiver were set up in an anechoic chamber to make a prediction for the polarization expected in the SPICE data. The separation distance between receiver and transmitter in the anechoic chamber was 3 m and the data recorded with a 5 GSa/s oscilloscope. The anechoic chamber has dimensions 11.58 m x 7.29 m x 7.36 m [64]. Fig. 4.3 shows an image of the measurement setup.

To test the polarization calibration as a function of launch angle, the transmitting antenna was rotated between 0° and 90° in the horizontal plane while the receiving LPDA was pointing towards the dipole antenna and orientated either at 0° (tines parallel to ground) or 90° (tines perpendicular to ground). This allowed us to capture the two polarization components of the emitted electric field for a range of launch angles. For each setup, 10 individual measurements were recorded.

The anechoic chamber data are processed in the same way as the SPICE data, as described in

the next section. To account for the difference in dielectric environments, after reconstructing the anechoic chamber electric-field, the frequency content is shifted from an in-air medium to an in-ice medium by dividing by the index of refraction of deep ice ($n = 1.78$). Shifting the frequencies by $\frac{1}{n}$ serves as a first-order approximation since the antenna is wavelength-resonant; to convert from a wavelength to a frequency in a different medium, a factor of n must be applied [21]. After performing this frequency correction, a rectangular band pass filter between 80 MHz to 300 MHz is applied in order to remove unwanted noise. Lastly, the signals are up-sampled to 50 GHz for better time resolution.

An example of a transmitted pulse taken from the anechoic chamber, following these corrections, is shown in Fig. 4.4. This example pulse was emitted at an angle of 60° off the direction of maximal gain (a typical geometry in the SPICE data). The electric field is mainly theta-polarized (polarized along the main symmetry axis of the dipole). This serves as a baseline signal for the ARIANNA polarization reconstruction. Defining the polarization as the angle between the energy fluence of the theta and phi polarization (see Sec. 4.7 for more details), the signal polarization measurement derived from the average of the calculated electric-field magnitudes from the 10 measured voltages for each polarization captured for a given geometry is shown in Fig. 4.5, which shows that the polarization reconstruction relevant for the launch angles in the SPICE experiment are between 8° to 10° (highlighted by the green band).

We note that this calibration signal is more difficult to reconstruct than a neutrino-induced signal for two reasons:

1. **Polarization:** The anechoic signal is almost entirely polarized in the theta direction. Therefore, the noise in the weaker phi component will have a large influence on the polarization reconstruction. For neutrinos, the signals are expected to have comparable theta and phi content.

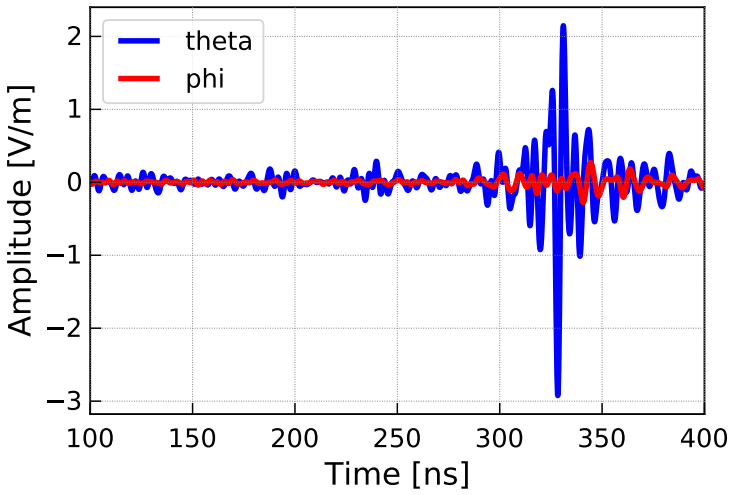

Figure 4.4: Observed electric-field from the IDL-1 pulser at an angle of 30° off boresight and captured inside an anechoic chamber. The LPDA antenna acts as receiver and a bicone antenna was used as the emitter. The LPDA antenna response was factored out of the voltage traces to obtain the electric-field. The theta polarization corresponds to the polarization along the axis of the dipole, while phi polarization is the cross polarized component.

2. **Pulse shape:** The phi component of the anechoic chamber signals have an extended pulse form, and with different frequency content compared to the theta component. A minimum integration window of 70 ns is necessary to sufficiently capture both components. Neutrinos will have signals with polarization projections equal in both length and frequency and differing only in amplitude between the two components. Therefore the polarization reconstruction will not strongly depend on the integration window and frequency cut.

With this in mind, this analysis can be considered a lower bound on the polarization reconstruction capabilities of neutrino signals, which should give cleaner signals.

4.3.3 Calculation of Incoming Signal Direction

Testing the ARIANNA angular reconstruction capabilities requires an accurate model of how ice affects propagation. The density, and therefore the index-of-refraction, changes in the

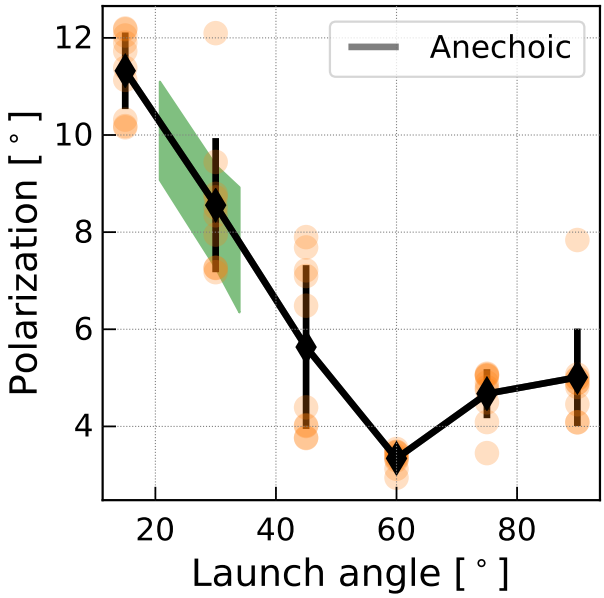

Figure 4.5: Expected polarization angle of the received electric field as a function of transmitted angle with respect to the main symmetry axis of the dipole. The orange data points are the polarization angle's found from using a single pair of voltage measurements. The black data points are the averages of the orange data, with the error bars being the standard deviation of the orange data points. Green shows the relevant transmitted angles for the SPICE data with a 1σ spread based off of the 16% and 84% quantile.

upper 200 m of the South Pole ice sheet from $n = 1.78$ for deep ice to about $n = 1.35$ at the surface. As a consequence, radio signals do not propagate rectilinearly but are refracted as illustrated in Fig. 4.6 [8]. We use an exponential index-of-refraction (n) vs depth (z) profile which provides a good description of $n(z)$ data that was derived from density measurements [16, 65]. The gray shading indicates the range of positions of the transmitter that permit no classical propagation solutions, which is termed the 'shadow zone'. Signals in the shadow zone, bend back into the ice before reaching the ARIANNA detector. However, signals can be seen in the shadow zone through horizontal propagation, likely due to deviations from a purely exponential density profile [16, 66]. These effects are lightly discussed in section 2.7.1.

Three representative allowed solutions are displayed in Fig. 4.6 corresponding to pulser depths of 418 m, 1 km and 1.7 km. The right panel gives the expected arrival and launch

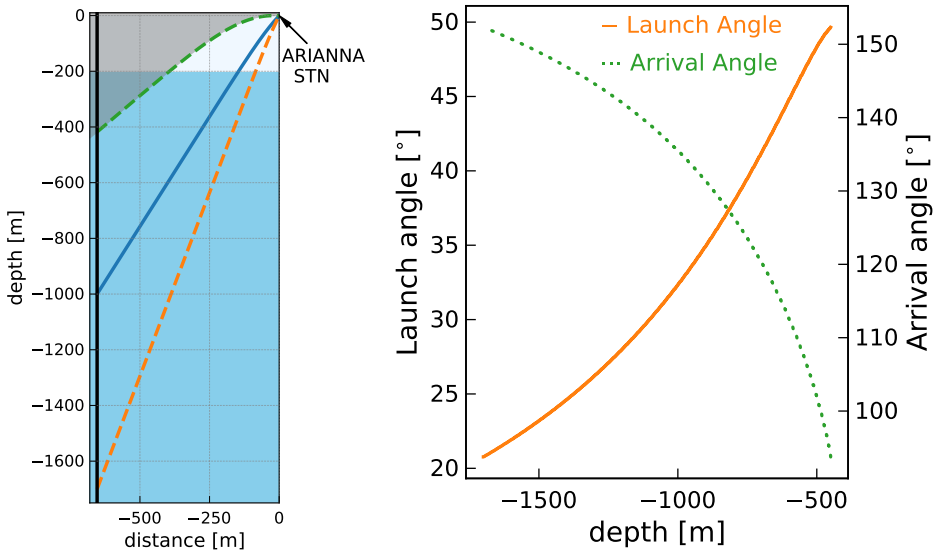

Figure 4.6: (Left) Ray tracing solution from a transmitter at depths 418 m, 1 km and 1.7 km to the South Pole ARIANNA station 51 calculated with the NuRadioMC code [8]. Light blue shaded region above 200 m is the firn layer, over which the ice approaches (within 2%) its nominal density. The grayed area is the shadow zone, from which classical propagation to the station is forbidden. The vertical black line on the y-axis represents the SPICE borehole. (Right) Expected arrival zenith angle and expected launch zenith angle as a function of transmitter depth. 180° corresponds to the nadir.

zenith angle (measured with respect to 0 degrees zenith) at the ARIANNA station as a function of transmitter depth.

4.4 Processing of Data Taken in the Field

This section describes how data from radio pulses emitted by the antenna in the SPICE hole are processed and which additional calibration steps had to be performed to reduce systematic uncertainties.

4.4.1 Main Processing Steps

Four main processing steps are applied to all events from the measurement campaign from the SPICE borehole:

1. **Initial quality cut:** The readout electronics of the ARIANNA station become non-linear when the signal amplitude exceeds 600 mV. During the 2018 SPICE core run, events in the linear regime occur at depths greater than 800 m and only these events are retained for analysis.

2. **Band pass filter:** To reduce out-of-band noise, the frequency content of the events is restricted with a rectangular band pass filter to between 80 MHz (set by the frequency threshold of the receivers) and 300 MHz. This cut also reduces the influence of noise on the time correlations of the signal pulses, improving the accuracy of the direction reconstruction.

3. **Deconvolution of signal chain:** To properly compare measured data from different channels, the amplifier response is deconvolved along with time delays from cables and electronics (as measured in the lab).

4. **Upsampling:** The traces are up-sampled from 1 GHz to 50 GHz, using the Fourier method provided by resample from the scipy package in python [56], to improve the timing resolution. This allows us to correlate the signals to 0.02 ns accuracy.

4.4.2 In-situ Calibration of Cable Delays

The cables in ARIANNA station 51 were measured with a precision of 0.5 ns. We can use the data itself to improve this calibration to about 0.1 ns by the following procedure. For each data point we calculate the expected propagation time from the emitter to each receiving

antenna using the signal propagation (ray tracing) module of NuRadioMC [8]. Also for each data point, we calculate the time differences between the signal pulses received in the antennas (separately for the LPDAs and the dipoles) by cross-correlating the signal pulses against the signal pulse of one reference channel, chosen arbitrarily as channel 3 for the LPDAs and channel 6 for the dipoles. Knowing the source location and the ray trajectories, we then subtract the expected time delays from signal propagation from the measured time delays. We find largely constant time offsets that are compatible within the experimental uncertainties of the station calibration. The distributions are approximately Gaussian with offsets of up to 1 ns between channels and standard deviation up to $\sim$0.1 ns. The variation is much smaller than the mean offset, though there is a slight depth dependence that was not consistent between channels. The mean of the distribution is assumed to be associated with cable delays or other delays along the signal chain. These time offsets (ΔT) are presented in Tab. 4.1 and are added to the cable delays when deconvolving the signal chain (step three above). We note that this procedure does not necessarily center the mean of the expected arrival direction (using all antennas) to the predicted arrival direction since we have used a single reference channel for our calculation of ΔT.

Channel	Reference Channel	Mean [ns]	STD [ns]
0	3	-1.34	0.12
1	3	-0.70	0.09
2	3	-0.16	0.07
3	3	0.0	0.0
4	6	0.11	0.12
5	6	-0.07	0.10
6	6	0.0	0.0
7	6	-0.99	0.09

Table 4.1: Time differences between channels after deconvolution of the hardware response and subtracting the expected time delays for each individual channel. First 4 rows use channel 3 (LPDA) as the reference channel, whereas the last four rows use channel 6 (dipole) as a reference channel. The mean of the time delay offsets from zero can be associated with uncertainties in cable delays.

4.5 Direction Reconstruction and Angular Resolution

The direction reconstruction capabilities of ARIANNA were first reported at the 2019 ICRC [67] and then improved upon in [52]. Below are the angular direction and polarization results of the SPICE data reported in [52].

The incoming direction of a triggered event can be reconstructed through the timing delays between antennas. The NuRadioReco framework [21] is used to reconstruct the incoming direction of a triggered event in the ARIANNA detector. The particular algorithm used is called the *cross correlation method* as it uses the time differences between two parallel pairs of antennas (found through correlating the two signals together) to determine the signal arrival direction. (See 3.2 for details of the reconstruction algorithm.) Correlating two signals together is typically improved with a filter in the time domain, and thus for the angular reconstruction, a Hanning window with a rise time of 20 ns and a width of 50 ns, and for which the filter is centered around the pulse maximum is applied. This aids the reconstruction by reducing the influence of noise and by removing after-pulses and other artifacts that could lead to spurious correlations of the trace not associated with the main signal.

We measure the arrival direction using the four LPDA waveforms; an independent measurement from the four dipole antennas provides a cross-check. In Fig. 4.7, we present the reconstructed signal arrival directions, relative to prediction, as a function of the emitter depth (cf. Fig. 4.6). The full range of SPICE data is included in Fig. 4.7 along with an average of 10 m depths of the reconstructed angular directions. Each point in the averaged data has roughly 30 events. For the LPDAs we apply an additional cut on the data where the reflection coefficient of the firn-air boundary is 50% or less which corresponds to a depth of 938 m. This extra cut is applied to minimize the influence of interference between reflected and direct signals arriving at the receiving LPDAs. We find a resolution in azimuth

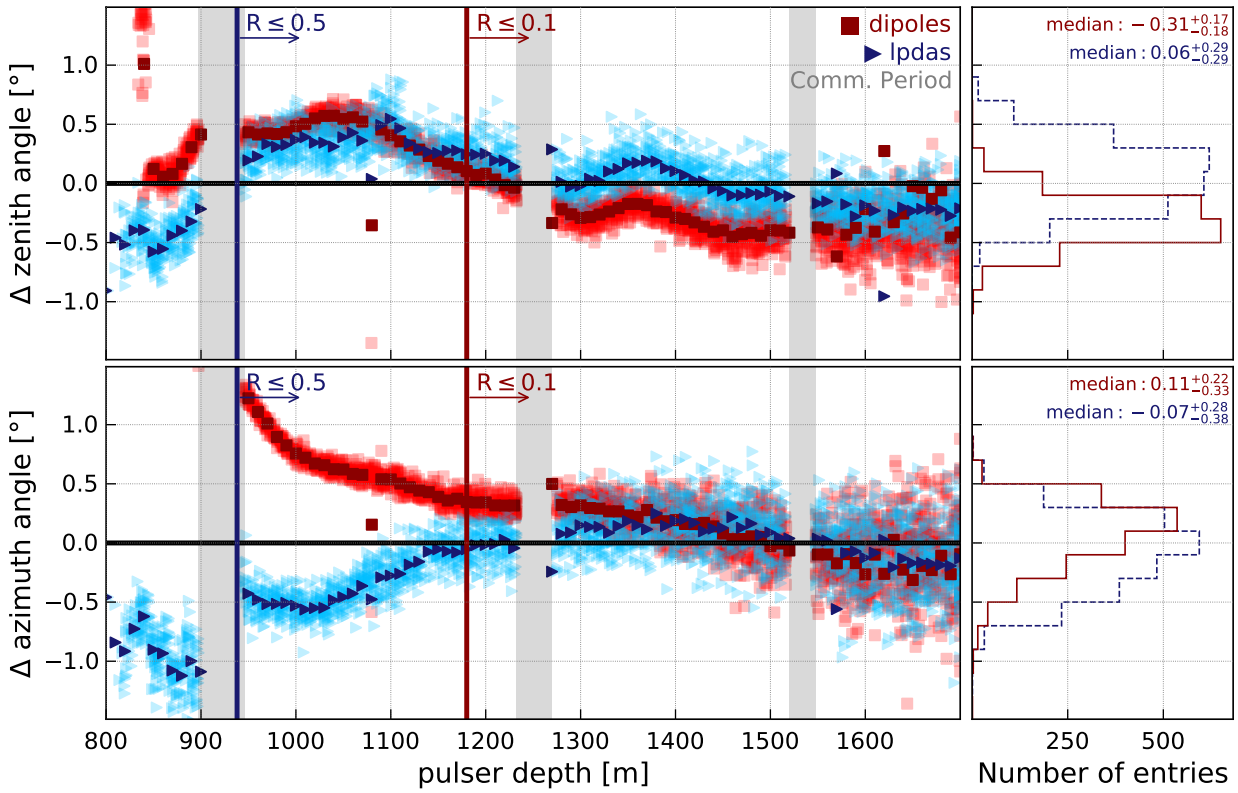

Figure 4.7: Reconstructed arrival direction minus expected arrival direction. Left plots show the depth dependence; histogram projections are shown on the right. This data is corrected for the time differences between channels shown in Table 4.1. The expected arrival direction is found using the NuRadioMC ray tracer while the reconstructed arrival direction is found through the cross correlation method. Light blue triangles show the residuals using the four LPDAs along with a 10 m average shown in a darker blue color. Red squares show the residuals using the four dipoles along with a 10 m average shown in a darker red color. Each average has roughly 30 events. The red vertical line corresponds to a reflection coefficient of 0.1, while the blue vertical line corresponds to a reflection coefficient of 0.5. The gray shaded area indicates the periods where station 51 was in communication mode and thus not taking data. The data in the projected histograms present the residuals on an event-by-event basis (i.e. without the averaging). Blue dashed is used for LPDAs, and red is used for dipoles. For the LPDAs all data-points with $R \leq 0.5$ are included and for the dipoles all data-points with $R \leq 0.1$ are included (see text for details). The mean and standard deviation is reported in the upper right corner of the histograms.

and zenith to better than 0.4° centered around 0.1° and −0.1° respectively. The dipoles are equally sensitive to signals arriving from above and below and were buried just 0.5 m below the surface and therefore the interference between reflected signals and direct signals is more pronounced. Thus, we apply a more stringent cut to the dipoles, requiring the reflection coefficient is 10% or less which corresponds to a transmitter depth of 1180 m. The dipoles give a resolution of 0.2° in zenith with a −0.3° offset and resolution of 0.3° in azimuth centered around −0.1°.

Another Askaryan based neutrino detector, ARA, has looked at reconstructing deep pulser events [35]. The ARA experiment uses birdcage dipoles for the vertical polarization and ferrite loaded quad-slot antennas for the horizontal polarization buried at depths between 170 m and 190 m which greatly reduces firn effects on the signal propagation. ARA reports an azimuthal resolution of 1.3° or better, with an offset of up to 2.0°. Without taking any firn effects into account, ARA reports sub-degree precision of at most 0.4° in zenith, albeit with a systematic offset of up to 4.8° [35].

To estimate the resolution on the ARIANNA directional reconstruction, the 3D angular difference between the reconstructed and predicted arrival direction is calculated. For the LPDAs, ARIANNA achieves a directional resolution of 0.37° whereas for the dipoles ARIANNA achieves a resolution of 0.43°. If we do not apply a depth cut to remove reflections, but instead take all data from when the transmitter was at depths greater than 800 m into consideration, then ARIANNA is able to achieve an angular resolution of 0.41° using the LPDAs and 0.55° using the dipoles. The measurement of the radio incoming direction is important for an accurate reconstruction of the vertex direction and the neutrino direction reconstruction (see [11]).

The slight offset seen in the zenith reconstruction using the dipoles is due to the four dipoles recording slightly different pulse shapes. It was assumed that the 4 dipoles had the exact same antenna response. The offset suggests significant antenna to antenna variations which

we speculate are due to the ∼50 cm proximity of the dipoles to the surface, with additional uncertainties associated with possible slight variations in orientations. Further investigations of the antenna-to-antenna response will hopefully mitigate any variations in the dipole zenith reconstruction.[1]

There are some slight depth dependencies seen in Fig 4.7, which may result from:

- **Ice profile:** An uncertainty in the index-of-refraction profile used to predict the signal arrival direction from the depth of the emitter will affect the prediction of the zenith angle. However, the azimuthal angle would remain unaffected as ice cannot affect the angle orthogonal to signal propagation (under the assumption of a vertical index of refraction profile, without horizontal components). The residuals from LPDAs and dipoles are affected in the same way.

- **Tilt of SPICE hole:** To predict the signal arrival direction we assume that the SPICE borehole is straight down, i.e., only the z-position of the emitter changes. However, the hole was reported to have a tilt starting at 1 km in 2020 [22]. The effects of this tilt profile are studied in 4.6.

- **Antenna position:** Uncertainties in the antenna position can lead to uncertainties in the directional reconstruction that are dependent on the signal arrival direction and therefore depth-dependent. In this case, the residuals from LPDAs and dipoles would be affected differently.

- **Antenna response:** Differences in the antenna response within the separate sets of dipoles and LPDAs can lead to antenna-dependent and signal arrival direction-dependent time delays and pulse distortions. Although mechanical differences are unlikely to cause any significant difference, since the antennas are so shallow, the close

[1] We note that the proposed ARIANNA-200 detector [32] aims to install the same mark dipoles at a depth of at least 5 m, and that the antenna depth will naturally increase with time due to snow accumulation. Thus, we expect that antenna-to-antenna variations will be much smaller than observed here.

vicinity to a boundary is likely to influence the antennas differently. This effect should be mostly visible at signal arrival directions for which the surface becomes reflective. Furthermore, the effect should be mostly visible in the dipoles because they are equally sensitive to upward and downward coming signals, whereas the LPDAs have a reduced gain for signals entering the (downward-facing) LPDAs from above.

We observe the strongest deviations from the prediction for dipoles at signal arrival directions for which the surface become reflective. We attribute this to uncertainties in the antenna response. The scatter of the LPDA reconstruction is also larger when the surface becomes reflective, although the effect is less pronounced than for the dipoles, consistent with this hypothesis. There is no consistent depth dependence between the LPDA and dipole reconstruction which disfavors a dominant influence of the ice profile or tilt of the SPICE hole. In particular, we can conclude that the ice is understood well enough to correct signal arrival directions for the ray bending to better than 1°, an important result for reconstruction of the neutrino direction. [2]

4.6 Effects of SPICE hole tilt profile on Angular Reconstruction

The tilt of the SPICE hole was measured by Emilie Sinkler and Delia Tosi in 2020 [22]. The data suggests a tilt of the SPICE hole starts to occur at 1 km and roughly 15° off of the opposite direction to the ice flow and going counterclockwise. The effects on the vertical alignment of the tilt profile has been estimated and is depicted in figure 4.8, which also shows how this tilt profile translates to the changes in the expected zenith and azimuth arrival directions.

[2] We also note that the antenna-related uncertainties will improve in a future ARIANNA-200 detector [32] by installing the antennas deeper into the ice to reduce interference between reflected and direct signals.

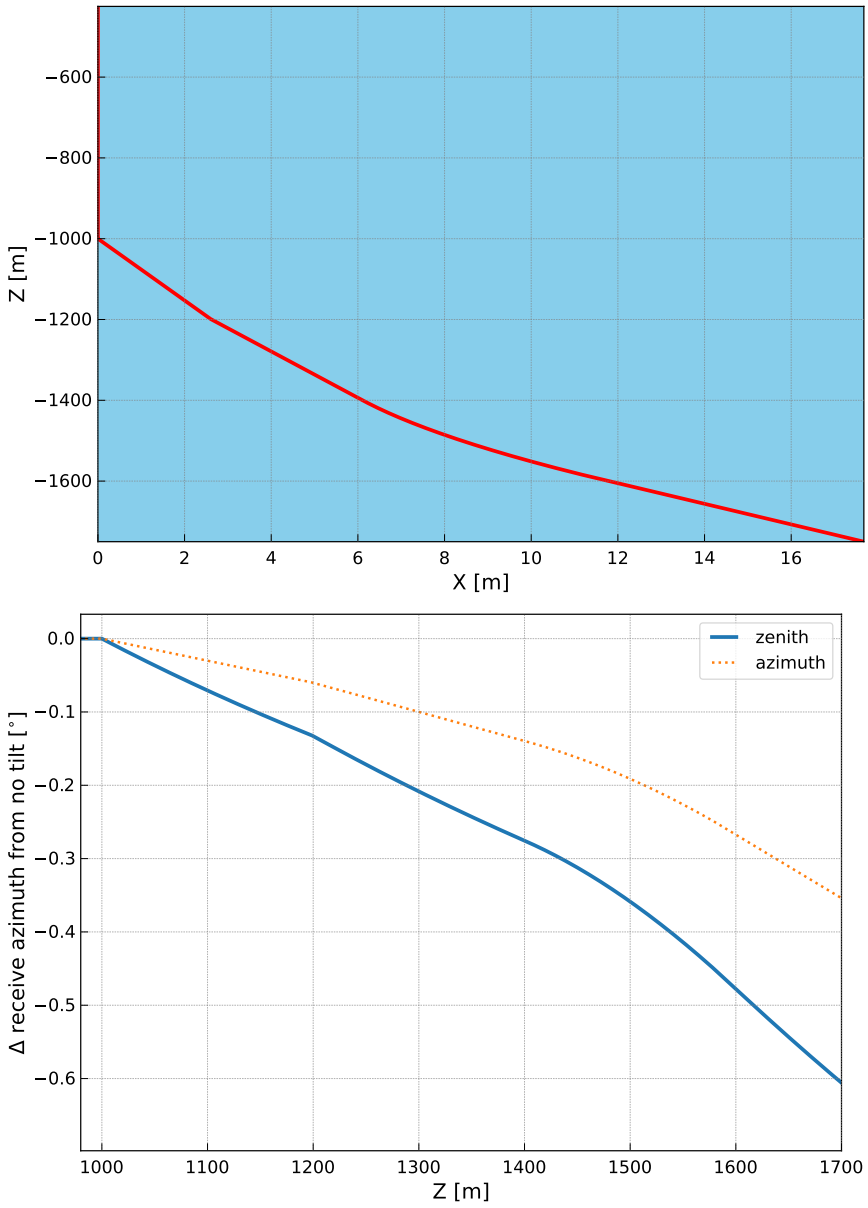

Figure 4.8: (Top) Shows the lateral change in position relative to the surface of the SPICE hole due to the tilt profile recorded in 2020 and taken from [22]. (Bottom) shows the changes in the expected arrival zenith and azimuth angles due to the tilt profile on in the left figure and into the direction of 327.7° with respect to grid east and going counterclockwise.

From figure 4.8 it can be seen that this particular tilt profile has minimal impact on the expected arrival direction (i.e. less than a degree for both zenith and azimuth across all depths). These changes in the expected arrival direction has been incorporated into figure 4.7 and the effects of the results are shown in figure 4.9.

The depth dependent trend of figure 4.9 has flatten with depths greater than 1 km showing consistency with the tilt profile reported in 2020 [22]. For the most part, the zenith and azimuth resolutions have improved for each antenna type by roughly 0.05° with the exception of the upper bound on the LPDA's when reconstructing azimuth, which has worsened by roughly 0.1°. This worsening is due to the data with a reflection co-efficient grater than 0.1 being offset from the data with little to no reflections, suggesting that modeling reflections in the LPDA antenna response accurately could improve the depth dependent resolution. Overall, the tilt profile does not change the general conclusion on ARIANNA's ability to reconstruct the angular direction.

4.7 Measurement and Interpretation of the Signal Polarization

In this section, the reconstruction of the polarization of the SPICE pulser signals is presented. To measure the polarization, ARIANNA needs to be able to measure the electric field using at least two perpendicular antennas. Using the two orthogonally oriented LPDAs, the framework NuRadioReco [21] is used to reconstruct the electric field from the recorded voltage traces (see section 3.3 for the algorithm for reconstructing the electric field).

The SPICE data was measured with 2 pairs of LPDA antennas with orthogonal polarization sensitivity. We apply a linear least square minimization to extract the electric field vector from the overdetermined system of equations (3.1), see section 3.3. The anechoic

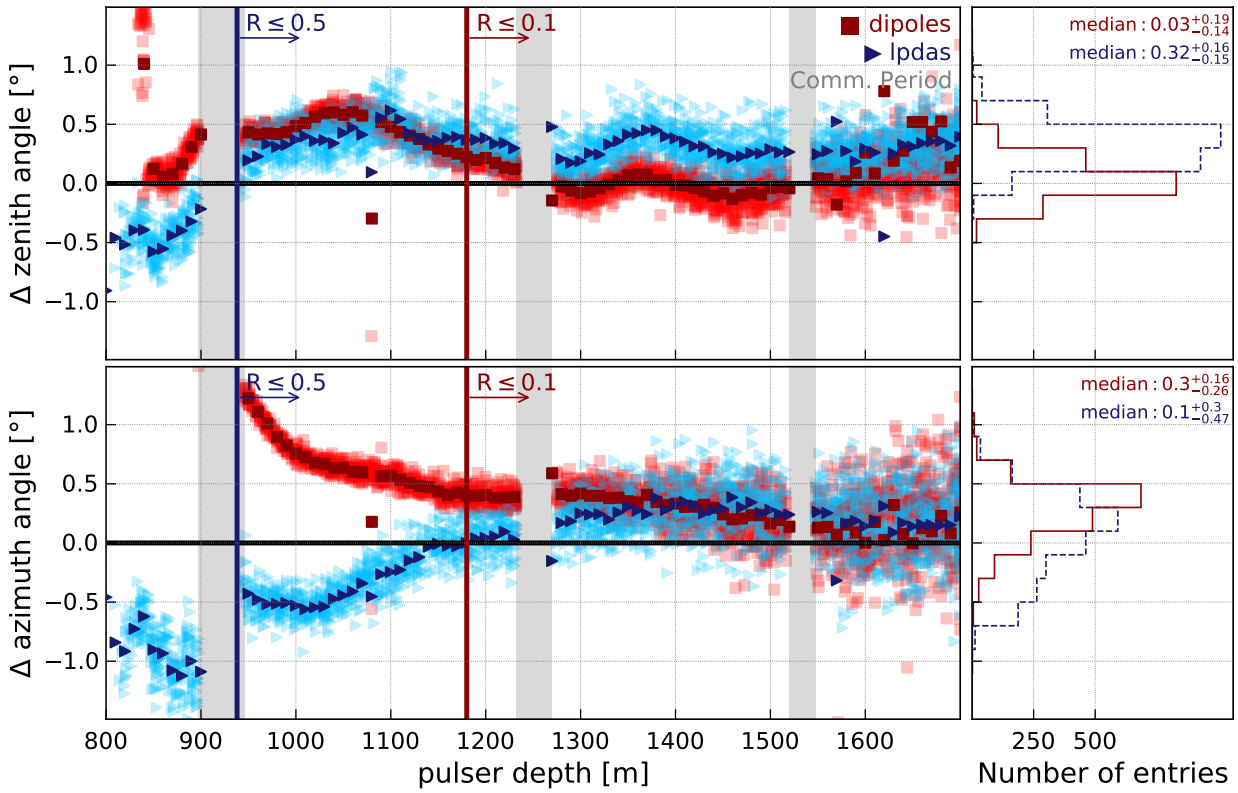

Figure 4.9: Reconstructed arrival direction minus expected arrival direction including the tilt profile from 2020 data [22]. The figure is identical to 4.7 in terms of how the data is presented, but a summary is provided again below. Left plots show the depth dependence; histogram projections are shown on the right. This data is corrected for the time differences between channels shown in Table 4.1. Light blue triangles show the residuals using the four LPDAs along with a 10 m average shown in a darker blue color. Red squares show the residuals using the four dipoles along with a 10 m average shown in a darker red color. Each average has roughly 30 events. The red vertical line corresponds to a reflection coefficient of 0.1, while the blue vertical line corresponds to a reflection coefficient of 0.5. The gray shaded area indicates the periods where station 51 was in communication mode and thus not taking data. The data in the projected histograms present the residuals on an event-by-event basis (i.e. without the averaging). Blue dashed is used for LPDAs, and red is used for dipoles. For the LPDAs all data-points with $R \leq 0.5$ are included and for the dipoles all data-points with $R \leq 0.1$ are included (see text for details). The mean and standard deviation is reported in the upper right corner of the histograms.

chamber measurement was performed with just two orthogonal LPDAs which leads to an exact solution of Eq. (3.1). The θ component is the dominant component used in the polarization calculation. The noise is subtracted by using a part of the trace without signal. The polarization definition in eq. (3.2) is also largely independent of the exact choice of the integration window; this was confirmed by analyzing the data with different choices of integration windows.

4.7.1 Polarization Reconstruction and Resolution

The transmitting angles for the range of depths that was analyzed by ARIANNA in the SPICE data are between 21° and 32° (with respect to the vertical) and which is also highlighted in green in Fig. 4.5. These angles are determined through the ray-tracing solutions found using NuRadioMC as outlined in Sec. 4.3.3. The expected polarization angles for this depth-range are between 8° and 10°, see Sec. 4.3.2. Ice effects, including the bending of the signal, and the frequency-dependent ice attenuation are accounted for in this calculation. The ice attenuation used is the *South Pole simple* model in NuRadioMC [8] and is derived from RICE data gathered in 2004 [16]. The SPICE hole is assumed to have no tilt for the polarization reconstruction analysis because uncertainties due to the launch direction on the antenna response have essentially no impact on a sub degree scale. Further, the reconstructed arrival directions are used for the antenna response which do not depend on the tilt of the SPICE hole.

A typical electric field from the SPICE data is shown in Fig. 4.10, overlaid with the corresponding electric field reconstructed from the anechoic chamber data. We observe that the IDL-1 pulser used in the 2019 anechoic chamber tests produced a lower amplitude than the 2018 SPICE data. This was confirmed in 2019, one month after the anechoic chamber measurement, when the same IDL-1 pulser was lowered into the SPICE hole. The resulting

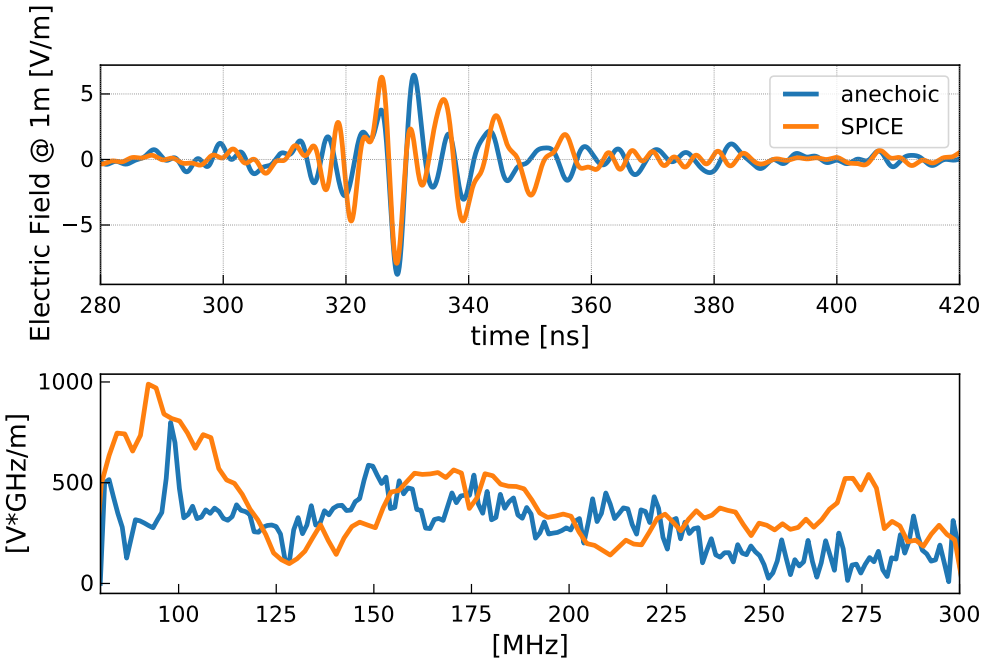

Figure 4.10: Overlays the reconstructed electric field from 2019 SPICE hole experiment (including ice effects) with the reconstructed electric field from tests in the anechoic chamber.

events recorded with station 51 were all consistently lower in amplitude than in the 2018 test. Therefore, we overlay a 2019 SPICE reconstructed electric field (which includes ice effects) with the reconstructed electric field obtained in the anechoic chamber. The SPICE electric fields appear identical between the 2018 and 2019 setup, modulo an overall scaling in amplitude. As seen in Fig. 4.10, the main pulse of the electric fields between the SPICE hole data and the anechoic chamber data is similar in frequency and amplitude, which demonstrates that the applied ice corrections (frequency-dependent ice attenuation and bending of the signal) are well-understood. There is evidence of interference in both measurements, but the two setups have different geometries. Also, the frequency scaling of the anechoic data from in-air to in-ice is only a first order approximation, and the dipole emitter might behave differently when placed in ice which can cause some of the residual differences.

In Fig. 4.11, we compare the reconstructed polarization from the SPICE data to the prediction from the anechoic chamber measurement (cf. Fig. 4.5), where the launch angle has been converted to depth according to Fig. 4.6. The resulting polarization measurements are then

averaged over 10 m depths which results in roughly 30 polarization measurements being averaged together. This is shown as dark blue circles in Fig. 4.11, where the error bars represent the 1σ spread of the distribution averaged. The light blue shading in Fig. 4.11 represents systematic uncertainties of the measurement resulting from uncertainties in the orientation of the LPDA antennas. When comparing the SPICE measurements to the anechoic measurements, we exclude data where the reflection coefficient is greater than 0.5 as indicated by the vertical blue line in Fig. 4.11 just as we had done for the angular reconstruction of the LPDAs. The SPICE data reconstructs a polarization that scatters around 9°, whereas the anechoic data reconstructs the polarization at 8° - 10°. The histogram of Fig. 4.12 shows the difference between SPICE measurement (on an event-by-event basis, i.e. without averaging) and the anechoic chamber prediction. We find a small mean offset of 0.35° and a scatter of 2.7°. We infer that we can make a precise polarization measurement for neutrino-induced Askaryan signals from the ability to determine the polarization of the radio pulser events.

There is some depth dependence seen in Fig 4.11. In particular, the reconstructed polarization from the SPICE data oscillates around the prediction from the anechoic chamber measurement. We observe that the amplitude of the θ component decreases monotonically with depth, as expected from ice attenuation and 1/r field diminution. The ϕ component, which has a lower signal-to-noise ratio[3] (∼4-8) than the θ component's signal-to-noise ratio (∼20-40), also shows this trend but with an additional oscillation of its amplitude. This results in the observed oscillation in the polarization, which is itself defined as the ratio of the amplitudes of the two components (cf. Eq. (3.2) and (3.3)). Although the exact reason for this effect is not known, we have considered the following potential sources:

- **Arrival Direction:** An uncertainty in the signal arrival direction will affect the antenna response pattern which is used in the polarization reconstruction. However, small angular changes of a few degrees have little impact on the antenna response. We

[3]using the standard definition of maximum signal amplitude divided by the RMS noise

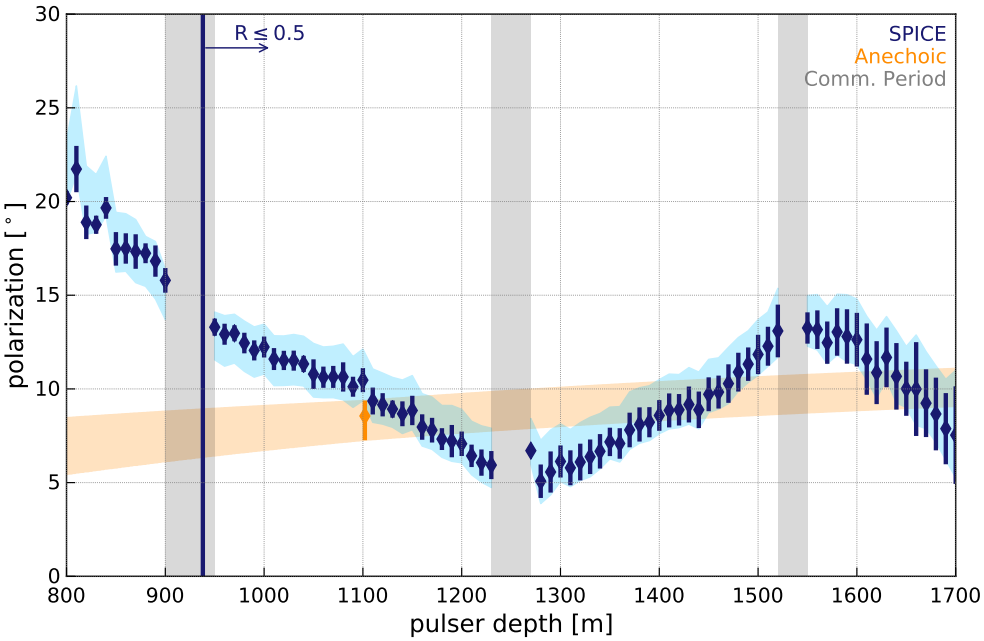

Figure 4.11: Measured polarization angle (blue data points) from 2018 SPICE hole experiment compared to measured polarization angle from tests in the anechoic chamber (orange band). The vertical blue line at 938 m indicates the boundary for which the reflection coefficient is 0.5. The gray bands shows the periods where the station was in communication mode and thus not taking data. The SPICE data was averaged over 10 m depths, and the 1σ spread of the distribution averaged is shown with the blue error bars. The light blue shading indicates the systematic uncertainty on the reconstruction stemming from systematic uncertainties in the ARIANNA LPDA orientations. There is only one anechoic data point that fits in the depth ranges of the SPICE data and is indicated as an orange diamond; the error bar represents the spread of the 10 event average. The orange band shows the linear interpolation to the next data points, outside of the depth range plotted. For the anechoic data the representative depth was calculated from the launch angle as in Fig. 4.6.

find that changing the incident direction by $\pm 2^\circ$ does not change the oscillatory behavior seen in Fig. 4.11 and only leads to a depth-independent shift in the reconstructed polarization of $\pm 1^\circ$.

- **Antenna response:** Boundary effects are hard to accurately model for antennas very close to a boundary. Since the receiver antennas are so shallow, the close proximity to the ice/air interface is likely to influence the antenna response. We have repeated the polarization reconstruction with antenna response patterns simulated for the LPDA immersed in finite firn (our nominal results), 1 m and 1 cm below the snow surface and

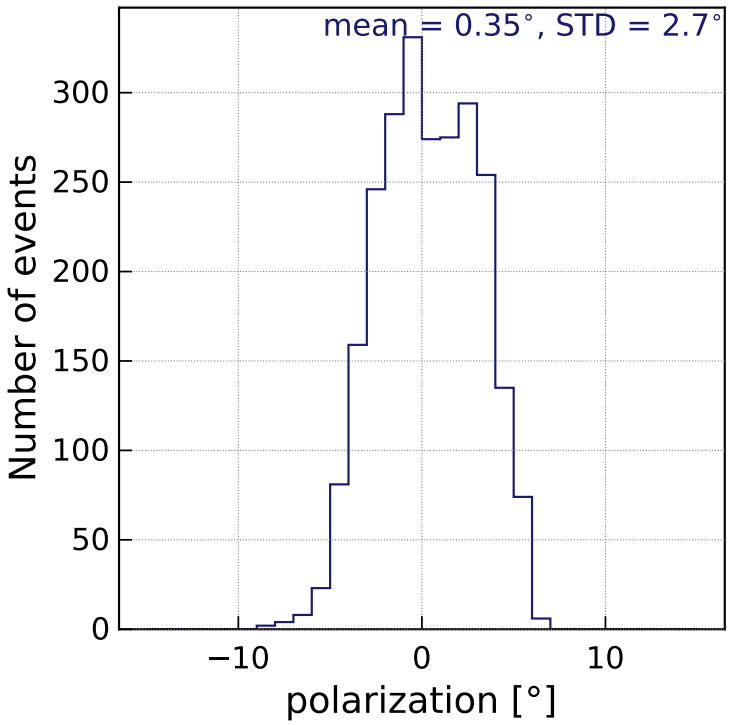

Figure 4.12: Difference between measured polarization from 2018 SPICE hole experiment (without averaging) and measured polarization from tests in the anechoic chamber.

did not observe any significant differences for transmitter depths below 1 km where surface reflections are small. However, the different LPDAs might be impacted differently by the boundary due to small differences in the geometry or snow surface which could impact the reconstructed polarization. [4]

- **Ice profile:** If propagation through the ice affected the polarization, a monotonic increase or decrease of the polarization with emitter depth would be expected. Thus, attributing the oscillatory behaviour to ice properties is challenging and would require different inhomogenities for different paths. A prior analysis [16] demonstrated that local ice density fluctuations, particularly in the firn, can result in classically unexpected signal propagation modes. Without additional *in situ* studies, we cannot rule out the possibility that such effects contribute to our observations.

[4] We note that the antenna-related uncertainties will improve in a future ARIANNA-200 detector [32] by installing the antennas deeper into the ice.

- **Change in emitter response with time:** If the emitted signal changed with time, then the polarization would also change with time and therefore depth. However, this is unlikely since ARIANNA observes the same polarization trend when analyzing SPICE data taken while the pulser was being lowered versus being raised.

- **Emitter characteristics:** If the emitted signal had some depth dependence, then the polarization would also change with depth. This might originate from depth dependent properties of the SPICE borehole, such as slight changes in the SPICE hole radius. Also, the emitter was lowered by a metal cable that will impact the response pattern of the emitting antenna, especially for launch angles close to the vertical. This may also result in the observed oscillatory behavior.

- **Reference measurement:** The anechoic chamber measurement was performed at discrete launch angles (cf. Fig. 4.5); only one laboratory launch angle lies within the corresponding range of emitter depths analyzed here. This reference point is shown as the orange diamond in Fig. 4.11. The predicted polarization is obtained via linear interpolation to reference measurements corresponding to depths outside our depth range. Interestingly, the reconstructed polarization from the SPICE data matches the anechoic measurement at the 1100 m reference point. A possible origin of the oscillatory behaviour is thus a change in the emitter characteristics with launch angle that was not captured by the discrete measurements performed in the anecoic chamber.

From the discussion above and because the change in polarization originates from amplitude variations of the small ϕ polarization component (see figure 4.13), we speculate that a change of the emitter characteristics is the most likely origin of this effect. The ϕ polarization corresponds to the cross-polarization component, for which an ideal dipole should have zero transmission. Thus, a change of the cross-polarization amplitude with depth and launch angle seems plausible (cf section. This would also mean that the polarization can be measured much better because the scatter of 2.7° is largely determined by the oscillations. The scatter

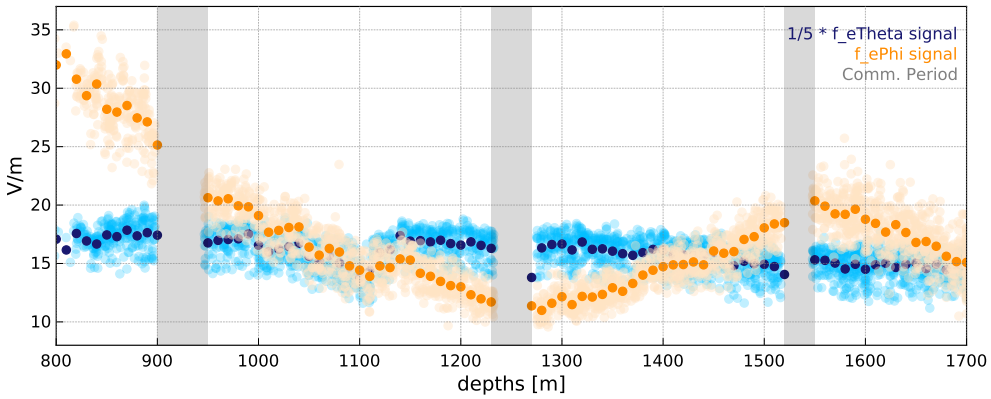

Figure 4.13: Energy fluence of the two electric field components. Frequency dependent ice attenuation and $\frac{1}{r}$ have been factored out. theta component has flattened showing reasonable understanding of the ice effects, where as the phi component continues to carry the oscillatory pattern seen in the polarization reconstruction per depth figure 4.11.

of the reconstructed polarization within a narrow depth range is often smaller than 1°. We also note the expected radio pulses from neutrinos will be cleaner: The signal will be the same in both polarization components in that the frequency spectrum and time domain behavior will be identical and only differ in amplitude which will facilitate the polarization reconstruction. This is in contrast to the SPICE transmitter which does not have the same frequency spectrum and time domain behavior in both polarization components.

4.8 Discussion of SPICE Results

We presented the measurement of calibration pulser signals, which were emitted deep in the ice at South Pole, with LPDA and dipole antennas placed slightly below the surface. The variable depth of the emitter and the large propagation distances of up to 2 km validated the modeling of the signal propagation with high precision.

We measured the signal arrival directions and compared it with the expectation which was computed from the emitter depth and a detailed calculation of the bending of the signal trajectories while propagating through the firn. We observe a negligible offset between mea-

surement and prediction with an event-by-event scatter to better than 0.4°. This result is of direct importance for the measurement of neutrinos: The effect of the ice on the propagation direction can be corrected with high precision which is important for reconstructing the neutrino direction. The corresponding uncertainty from ice modelling is likely much smaller than 0.4° as this scatter is mostly due to statistical event-by-event uncertainties. No evidence for a systematic shift in reconstructed direction with depth was found.

We reconstructed the three-dimensional incident electric field using two pairs of orthogonal oriented LPDA antennas and compared it with a reference measurement of the emitter in an anechoic chamber. After correcting for detector response and ice attenuation, we find agreement in amplitude, pulse shape and frequency content. This shows that the attenuation of radio signals is well understood and that the propagation through the ice does not lead to any significant distortion of the radio pulse.

We also calculated the polarization from the reconstructed electric fields. We find good agreement with the reference measurement of the anechoic chamber with an offset of 0.35° averaged over all depths, and a scatter of 2.7°. We observe an oscillation of the reconstructed polarization with depth which is likely due to changes in the emitter characteristics which would suggest that the polarization can be measured with even higher precision. Further studies are needed to find the origin of this effect and are planned for the future.

These results are of direct importance for the reconstruction of the direction and energy of neutrinos. The neutrino direction is a function of a) the signal arrival direction corrected for bending in the firn, b) the polarization, and c) an additional weak dependence on the viewing angle. The resolution of the neutrino direction is approximately the square root of the quadratic sum of the individual uncertainties of the three parameters. This analysis showed that uncertainties in the ice modelling will affect the neutrino direction resolution by not more than 3° and likely less depending on the origin of the scatter in the polarization reconstruction.

Chapter 5

Neutrino Direction and Shower Energy Reconstruction

So far the radio frequency signal's angular resolution and polarization resolution has been studied and quantified from *in situ* SPICEcore [13] data that was triggered by the ARIANNA South Pole station 51. The viewing angle was left as undetermined when analysing the impact that the results had on the neutrino angular resolution. The polarization resolution was much larger than the radio signal's angular resolution with roughly 2.7 degrees compared to 0.37 degrees. This chapter looks at reconstructing the viewing angle of neutrino events and ties it together with the radio signal's polarization and angular resolution to make a more detailed prediction on the neutrino direction resolution, and as a consequence of the process, the shower energy resolution is also obtained.

The viewing angle reconstruction relies heavily on being able to predict the frequency spectrum produced from a neutrino event. Figure 3.2 shows a typical dependence on the Askaryan frequency spectrum as a function of viewing angle which uses the Alvarez 2000 parameterization [18]. As the viewing angle of the event moves towards the Cherenkov angle in deep

ice (approximately 55.8 degrees), the emitted RF signals coherently add up and contains a broader frequency spectrum. This broadening or narrowing in the frequency spectrum is precisely what needs to be measured in order to determine the viewing angle, while a large data set is needed to quantify the resolution. Because a large neutrino data set is not achievable with an *in situ* experiment, studies turn to Monte Carlo simulations.

5.1 Simulation Conditions

NuRadioMC was used to produce a simulated set of neutrinos [8] with a range of energies. The majority of the studies were performed at the South Pole, with randomly generated neutrinos in a cylindrical volume having a depth of 2.7 km and a radius of 2.5 km. The top of the cylinder is centered on a simulated ARIANNA station. The following conditions were applied to the neutrino simulation:

1. The South Pole 2015 ice profile, taken from [16], was used for the ray tracing module. Section 5.3.4 compares South Pole to Moore's Bay and therefore also simulates neutrinos with the Moore's Bay simple ice profile [16].
2. The Alvarez 2009 neutrino parameterization [59] was used.
3. Only hadronic showers have been considered.
4. The current simulation setup treats the hadronic component of all neutrino flavors identically.

Further, a slight variation to the usual ARIANNA station was used. The station layout includes five channels, with the typical four down facing LPDA's buried just beneath the surface, but also with a central dipole at 15 m depth for good D'n'R measurements (see

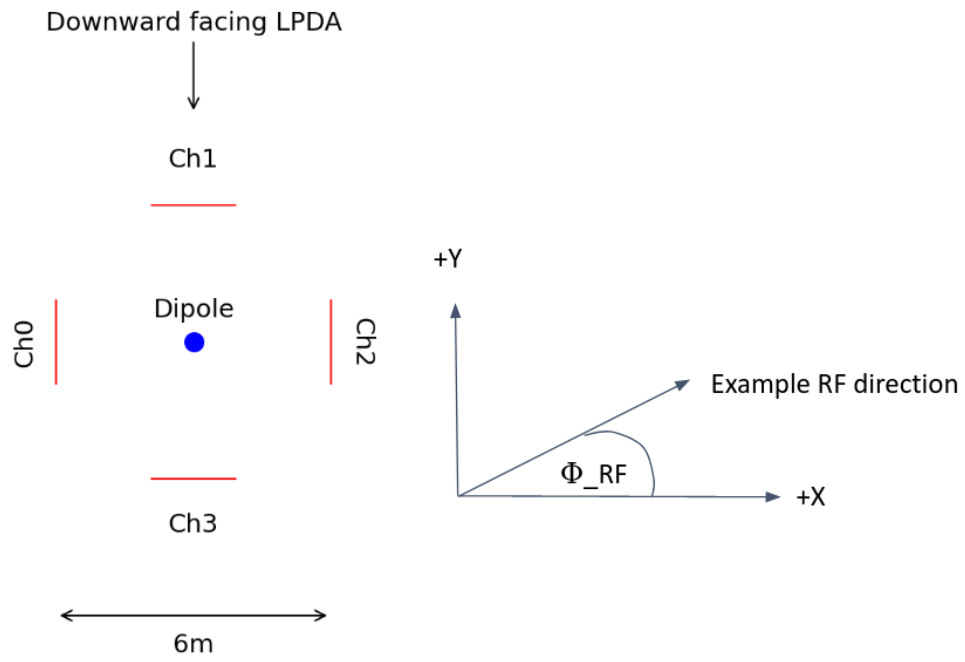

Figure 5.1: Antenna layout for the simulated station used to probe the viewing angle and ultimately the neutrino direction reconstruction.

section 3.5). A 15 m dipole provides good time separation between direct and reflected or refracted signals while also keeping the trace compact to the usual 256 ns window. Figure 5.1 shows the antenna layout for this simulated station. A narrow band (80 MHz - 150 MHz) trigger, 2 of 4 LPDA majority logic at 3.9 sigma was used. This threshold corresponds to a 100 Hz thermal trigger rate. Further, a 3 sigma dipole trigger which is equivalent to a four dipole phased array was studied and is presented in 5.3.3.

A typical population of triggered neutrino vertex locations from the simulations at the South Pole and at Moore's Bay is shown in figure 5.2. The distribution at the South Pole has a cone shape. The upper boundary of the cone is a result of the shadow zone. Signals originating in the shadow zone will bend back into the ice before reaching the detector. The other two edges are due to the earth being opaque for UHE neutrinos and the Askaryan emission is mainly at viewing angles around the Cherenkov cone since the RF emissions coherently add at these viewing angles making the signal amplitude large enough to trigger on. This restricts

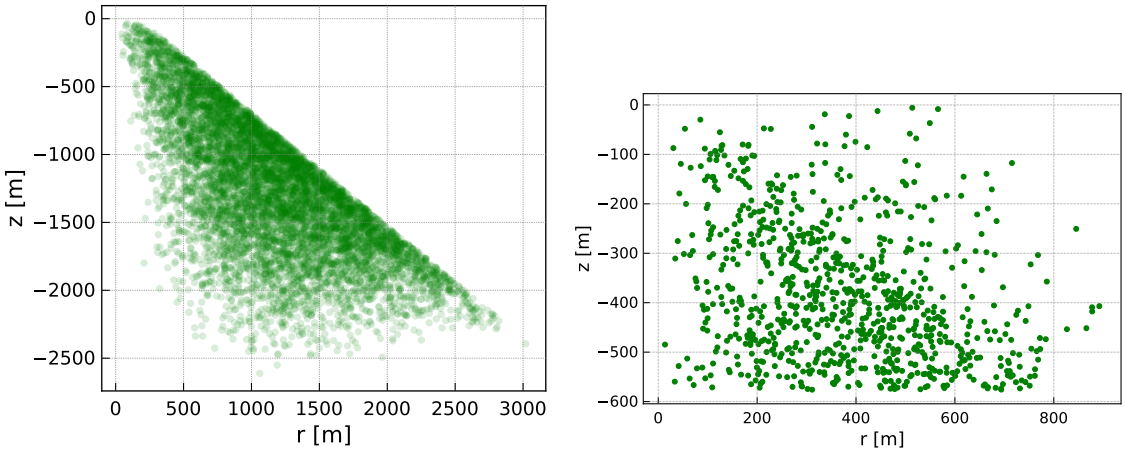

Figure 5.2: Simulated vertex locations of triggered neutrino events from NuRadioMC. (Left) is for South Pole and (right) is for Moore's Bay. Z is the depth of the vertex location and r is defined as $\sqrt{x^2 + y^2}$.

the South Pole to neutrinos that are mainly traveling horizontally. The Moore's Bay vertex positions do not have a well defined cone shape like South Pole. Moore's Bay is unique in that the bottom layer serves as an additional reflection layer due to the liquid water beneath the ice sheet. This reflective layer allows for more vertically traveling neutrinos arriving from above to be detectable because the signals can reflect off of the bottom layer and travel upward towards the detector. These extra ray tracing solutions also provides some sensitivity to events that would other wise be in the shadow zone.

5.2 Reconstruction Conditions

The neutrino direction and shower energy reconstruction procedure is discussed in section 3.5. The main precursor to this method is the reconstruction of vertex position. The vertex position along with the station layout and ice profile fully determines all ray tracing solutions, which is necessary to model different Askaryan signals from source to detector. Therefore, in order to determine the neutrino properties such as direction and energy, the event generation, radio signal propagation, and station convolution needs to be well understood. Systematic

errors due ice profile and station description is discussed in section 5.4.

The effects on neutrino direction resolution due to uncertainties in the vertex position have been studied to a significant extent. To reconstruct the vertex position, first a measurement of the radio signal's angular direction needs to be made. Then, using the ice profile with the generally accepted assumption that the signal originated below the firn, the vertex direction can be determined. However, the distance is still unknown. The D'n'R technique is used to find the vertex distance and ultimately reconstruct the vertex position. The technique takes advantage of a clean measurement between a direct and reflected or refracted signal in a dipole channel. The time delay between these two signals determines the vertex distance. The errors in determining the vertex position propagate mainly into the distance because of the sub degree radio signal's angular resolution (see figure 4.7), which constrains transverse errors in the vertex position relative to the ray tracing solution. A study on the vertex position resolution then simplifies to a study of the vertex distance resolution.

The resolution on reconstructing the vertex distance has been extensively studied in [17] through a separate Monte Carlo data set of neutrinos at the South Pole. The study presented in [17] uses the same simulation conditions as this chapter. A dipole was modeled at 15 m depth, NuRadioMC was used with the same cylindrical volume to generate the neutrino data set, the South Pole 2015 ice model was used [65] for ray propagation, and the Alvarez 2009 parameterization was used to model the Askaryan emission for these neutrino events. Because the simulation setup for the study on the vertex distance resolution is the same as this chapter's setup for the neutrino direction and energy analysis of an ARIANNA station, the vertex resolution results can be directly transferred. The main conclusion for the resolution of the vertex position and how it propagates to an uncertainty in shower energy is summarized in figure 5.3 which was directly pulled from [17]. The vertex resolution is given as 0.04 and 0.05 in $\log10(R_{rec}/R_{true})$ for neutrinos with energies of 10^{17} and eV 10^{18} eV respectively.

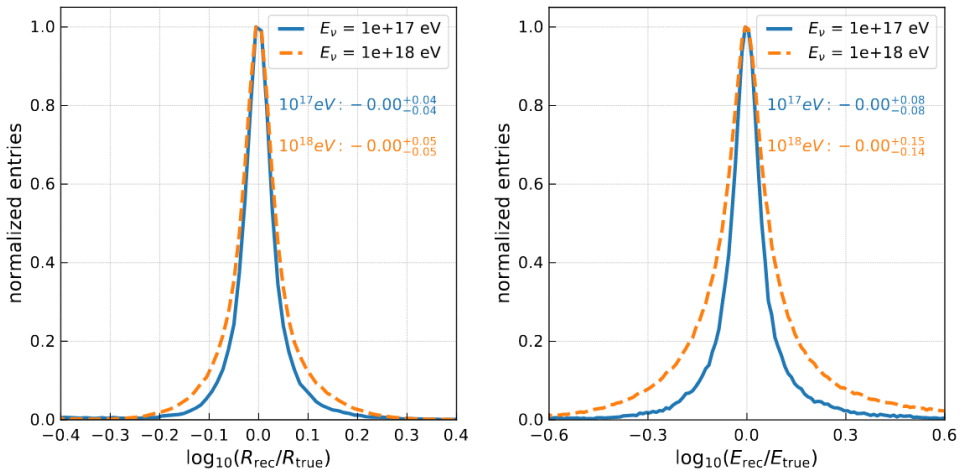

Figure 5.3: Left shows the vertex resolution for a receiving dipole at 15 m depth and added uncertainty of 0.2 ns from the D'n'R time delay along with 0.2° resolution in RF zenith direction. Right shows the energy resolution given the vertex resolution. Taken from [17]

The resolution on vertex distance can be justified through the excellent timing resolution that is achieved from using the same antenna to measure two signals, the direct and reflected or refracted signal. Using the same antenna removes any uncertainties due to antenna modeling and amplifier response. Further, any uncertainties between timing delays from cables is irrelevant. This allows the timing resolution between the two signals to be on the order of 0.1 ns. This translates to a very precise measurement of the vertex distance.

With all this in mind, the error on the vertex position is then simulated to be only on the vertex distance, which should have no impact on the neutrino direction reconstruction as all the ray tracing solutions should be directionally identical and only differ in the amount of ice attenuation. To model this uncertainty, a Gaussian distribution in log space with the resolutions reported in figure 5.3 was used to generate a random uncertainty to the true vertex distance, and then propagated into the direction of the launch vector of channel 0. Figure 5.4 shows the modeled error distribution for this analysis, which directly matched that of figure 5.3.

With the new vertex position calculated, the ray tracing solutions are obtained, and a chi

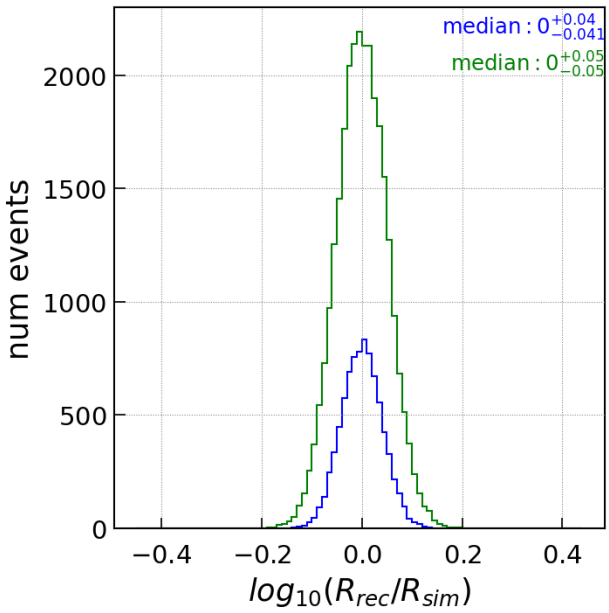

Figure 5.4: Fractional error of vertex distance that was added to the true vertex distance during reconstruction. Used to simulate the uncertainty in vertex position. This figure is for neutrinos with energies of 10^{18} eV (blue) and 10^{18} eV (green).

squared minimization is performed to find the best matching neutrino direction and energy. The input used for the minimization method was a twenty degree range of neutrino zenith and azimuth directions centered around the true direction, and with one degree steps along with an energy range between 10^{14}eV to 10^{19}eV with 0.1 degree steps in a logarithmic scale.

5.3 Reconstruction Results

The results first focus on a neutrino data set with energies of 10^{17}eV and 10^{18}eV. This was chosen as a starting point for two reasons. One is that this is within the energy range of a typical radio based neutrino detector which is between 10^{16}eV and 10^{20}eV. Secondly, this corresponds to the two energy bins that was studied for determining the resolution of vertex position [17] and therefore the uncertainties can be directly transferred from that study to this one. A note is that the simulation process takes much longer to produce the same number of triggered neutrino events for lower energies, and thus for time efficiency,

the amount of data at lower energies typically is smaller than the amount of data at higher energies. It will be shown that the neutrino space angle resolution is minimally effected by vertex errors mainly because the errors are propagated into the direction of the ray tracing solution (i.e. is only on vertex distance, not direction). Due to this result, the neutrino space angle resolution will be further studied for a wider range of energies without the need to add a vertex error which would otherwise require further simulations to determine the uncertainties on vertex position.

5.3.1 Reconstruction with Vertex Error

The last variable in reconstructing the neutrino direction that was not studied in previous chapters is the viewing angle. Chapter 4 provided an analysis of the radio signal's direction, polarization, and ice profile, showing excellent precision with a surface based detector. Here The viewing angle is reconstructed through taking the neutrino direction that produced the smallest chi-squared value, and calculating the angle between the neutrino direction and the radio signal's direction. The resolution on the viewing angle is show in figure 5.5. The resolution is found to be +0.64 and -0.88 degrees for neutrinos with energies of 10^{17} eV, while being +1.1 and -0.97 degrees for neutrinos with energies of 10^{18} eV. Events with larger viewing angles can be triggered at higher energies, which are harder to model, and provides an explanation for the degradation on viewing angle resolution with increased energy. This is a first estimate of the viewing angle resolution for an ARIANNA detector and shows that the viewing angle can be constructed fairly precisely which translates to better precision for the neutrino direction.

The reconstruction of viewing angle is performed through a chi-squared minimization on the neutrino direction and shower energy. Therefore, the resolution of neutrino direction and shower energy can be directly studied. The neutrino direction is provided as a space

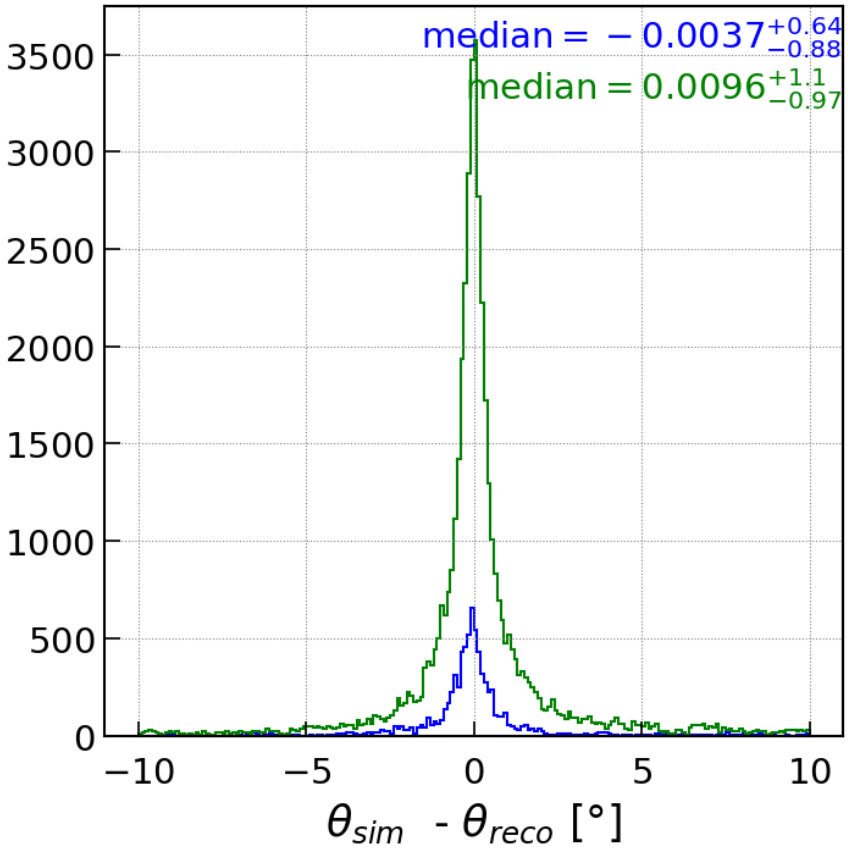

Figure 5.5: Viewing angle resolution for neutrinos with energy 10^{18} eV. A vertex error is added according to figure 5.3. Sim represents the true neutrino viewing angle and reco represented the reconstructed viewing angle.

angle which is defined as the angle difference between the true neutrino direction and the reconstructed neutrino direction, labeled as $\Delta\psi_\nu$. Figure 5.6 contains two histograms of the neutrino space angle, the left is without adding a vertex error and the right is with adding a vertex error. The resolution without simulating a vertex error is 3.3 degrees and 2.9 degrees for neutrinos with energies of 10^{17} eV and 10^{18} eV respectively. Likewise, with adding a vertex error, the neutrino space angle resolution is 3.6 degrees and 3.1 degrees for 10^{17} eV and 10^{18} eV respectively. Theoretically, the vertex error is entirely on the distance, and so the only effect that the vertex error should have is on the amount of ice attenuation that is applied to the signal. The slight differences in the space angle resolution can be attributed to a couple properties. One being that the process of adding a vertex error only on distance is not performed perfectly for all ray tracing solutions. The ray tracing solutions are calculated on a per antenna basis, and therefore, adding an error to the vertex distance may align perfectly with one particular antenna, but actually slightly alters the direction of the ray tracing solutions to the other antenna pairs. This effect is small and is dependent on how the vertex error is simulated which in this study propagates the vertex error into the ray tracing solution for the direct ray going to channel 0. Another cause of the slight differences between the two histograms in figure 5.6 is through the frequency dependent ice attenuation, which can slightly alter the shape of the frequency spectrum and ultimately the voltage trace itself. These effects are however minimal as can be seen in figure 5.6, and hence it is a reasonable approximation to assume that the vertex error does not effect ARIANNA's ability to reconstruct the neutrino direction.

The main impact of adding a vertex error is in the amplitude of the frequency spectrum which ultimately changes the predicted shower energy. The resolution of shower energy is given in figure 5.7 where again the left histogram shows the shower energy reconstruction without adding a vertex error, whereas the right includes a vertex error. When including a vertex error, the shower energy resolution closely matches the resolution in figure 5.3. The resolution is found to be +0.10 and -0.09 in $\log10(E_{rec}/E_{true})$ for 10^{17} eV and +0.15 and

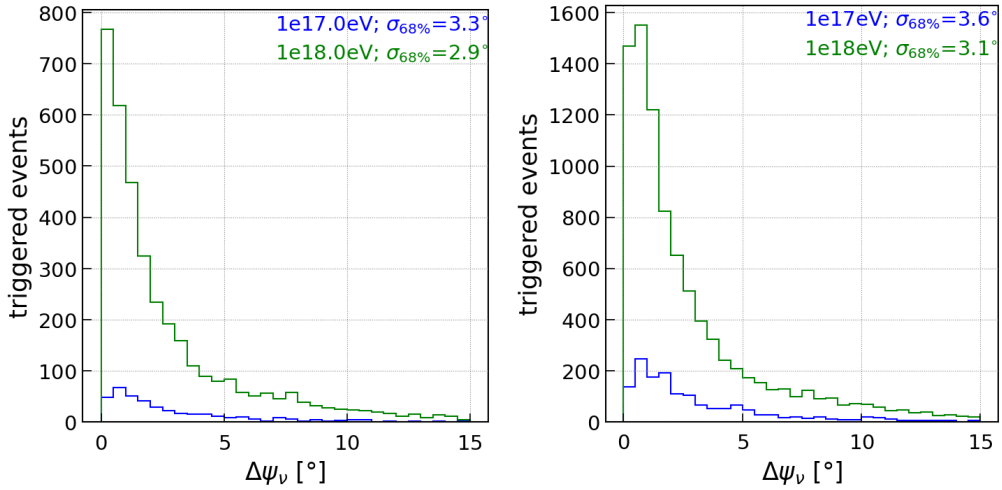

Figure 5.6: Space angle resolution for neutrinos with energy 10^{18} eV. (Left) does not introduce an error to the true vertex position. (Right) adds an error to the true vertex position according to figure 5.3.

-0.14 in log10(E_{rec}/E_{true}) for 10^{18} eV neutrinos. At 10^{18} eV, the resolution corresponds to 38% - 41% on a linear scale. This is significantly smaller than the energy limit due to the inelasticity of the initial neutrino interaction which is around 0.3 in log10(E_{rec}/E_{true}) for hadronic showers (see figure 5.8) [17]. This reconstruction procedure is sufficient for making a prediction on shower energy because it is below the inelasticity limit. Further studies will need to be made to look at the neutrino direction and energy resolutions for electromagnetic showers.

5.3.2 Energy Dependent Space Angle Resolution for Neutrinos

The neutrino space angle resolution was studied for a range of neutrino energies between 10^{17}eV and 10^{19}eV and only looking at hadronic showers. The vertex error is no longer included in this or the following studies and therefore only the space angle resolution is considered. The results of the energy dependent space angle resolution are reported in figure 5.9. This figure groups events into four energy bins with width of 0.5eV in log space. The legend gives the lower bound for each bin. As the energy increases, the resolution

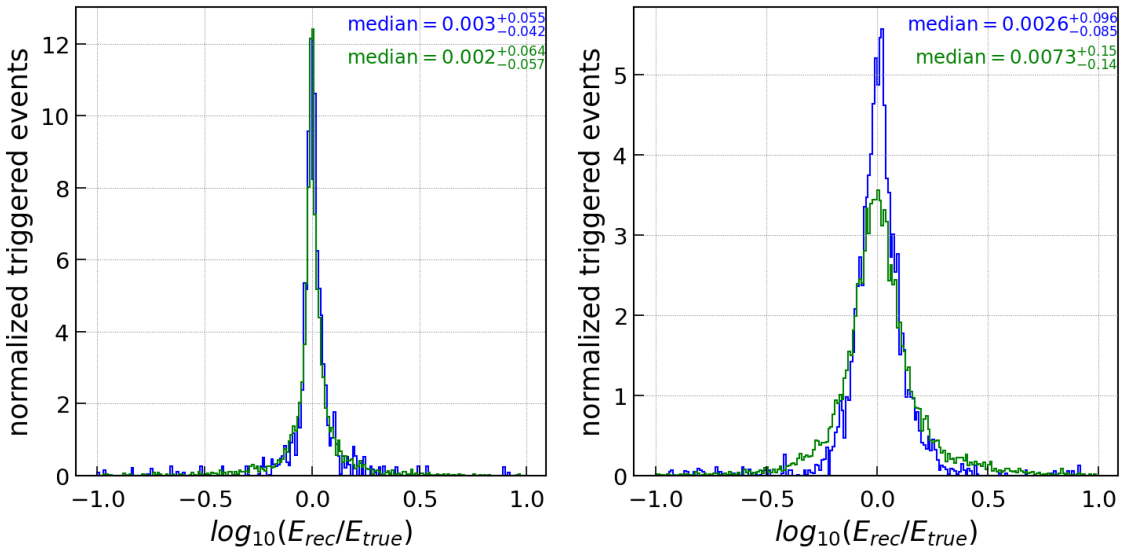

Figure 5.7: Shower energy resolution for neutrinos with energy 10^{17} eV and 10^{18} eV. (Left) does not introduce an error to the true vertex position. (Right) adds an error to the true vertex position according to figure 5.3. True represents the true neutrino viewing angle and reco represents the reconstructed viewing angle.

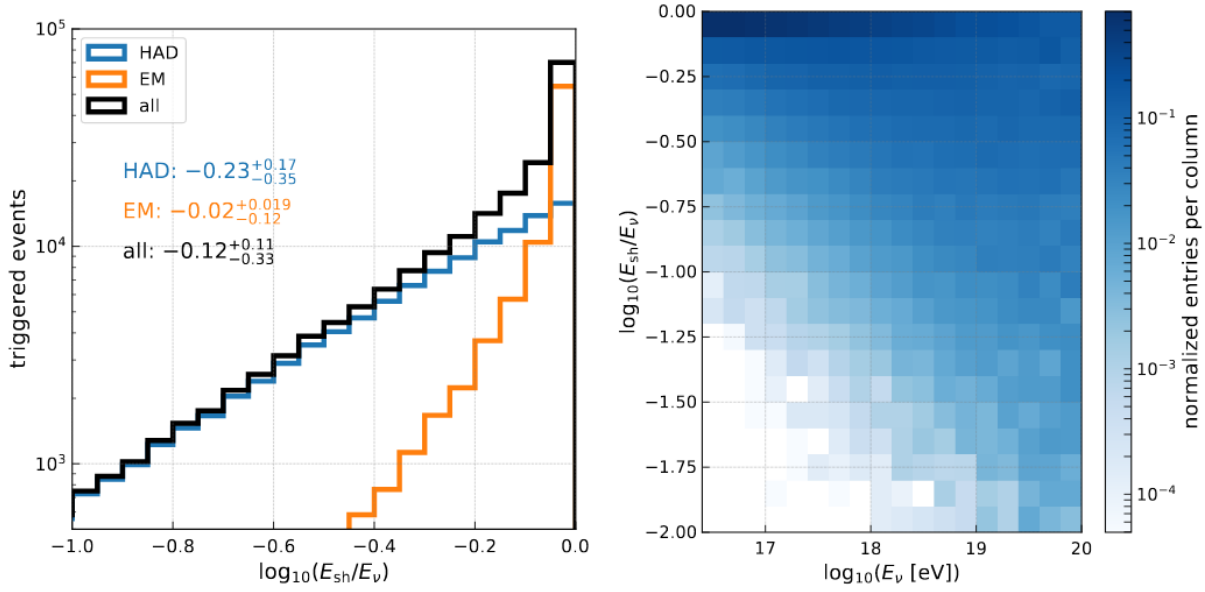

Figure 5.8: (Left) shows the ratio between shower energy and neutrino energy for triggered events. (Right) Shows how the left ratio depends on neutrino energy. Taken from [17].

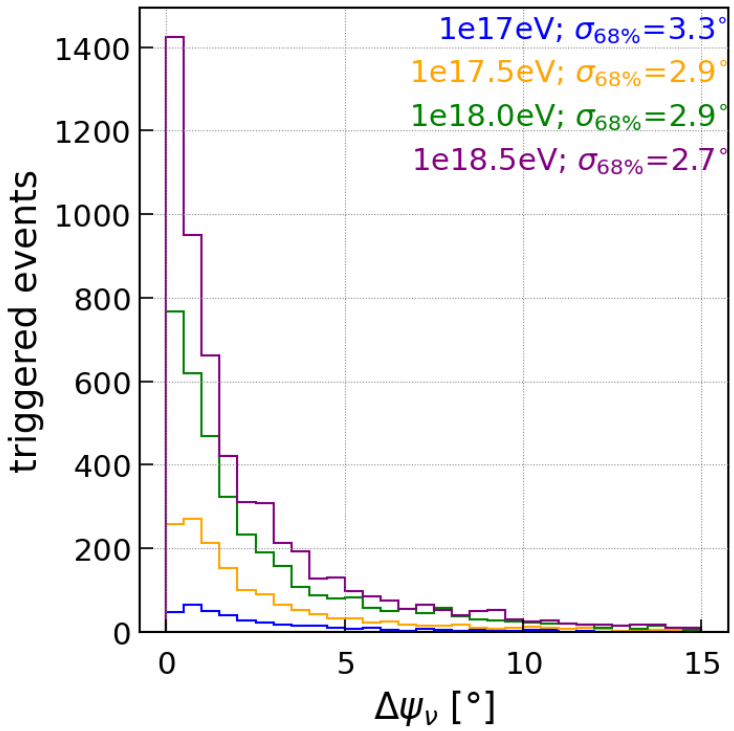

Figure 5.9: Space angle resolution for neutrinos with a range of energies between 10^{17}eV and 10^{19}eV grouped into 0.5eV bins in log space. The legend labels the lower bound of each energy bin and the space angle resolution for that bin.

on space angle slightly improves. This could be due to the hadronic component providing a larger fraction to the overall Askaryan signal as the neutrino energy increases. Overall, the resolution on neutrino space angle is around 3° for all energies which is sufficient for coincidence measurements with the IceCube detector.

5.3.3 Including a Phased Dipole Array

Including a phased array component to an ARIANNA surface station was studied to determine the gain in triggered events versus the overall degradation on neutrino space angle resolution. A four dipole phased array with dipoles all aligned vertically and placed into a single hole with 1 m separation between them and centered at 15 m can be approximated with a single dipole at 15 m and a three sigma trigger. In the approximation, the root mean

square noise would then be reduced by a factor of two during analysis in order to model the averaging of a four dipole phased array. This equivalence setup is how a phased array component was studied in this section.

The phased array is sensitive to horizontally propagating signals. Setting triggering mechanics to the phased array along side a narrow band LPDA 2 of 4 majority logic trigger allows for additional sensitivity, increasing the overall number of triggered events. Some events will trigger the phased array only, while some will trigger both trigger types or just the LPDA's. One key factor in this is the geometry of the phased array relative to the LPDA's, which has a difference in depth of 15 m. Weak signals seen by the dipole may be in the shadow zone for the LPDA's or too weak to be detected by the LPDAs. The table below shows the neutrino weighted (see section 3.4.1) number of triggered events for various combinations of the two trigger types (narrow band LPDA or phased array dipole).

Energy Bin [eV]	1e17-5e17	5e17-1e18	1e18-5e18	5e18-1e19
Total # Events	2682	4058	7080	9082
LPDA Triggered	42.0%	54.7%	62.2%	67.4%
Dipole Triggered	91.0%	88.6%	86.2%	85.8%
LPDA and Dipole Triggered	33.0%	43.4%	48.4%	53.2%
LPDA and not Dipole Triggered	9.0%	11.4%	13.8%	14.2%
Dipole and not LPDA Triggered	58.0%	45.3%	37.8%	32.6%
No LPDA Signal in all 4 Channels	28.8%	26.9%	26.6%	25.6%

Table 5.1: Percentage of events that meet various combinations of narrow band LPDA trigger and dipole trigger.

The phased array trigger roughly doubles the total number of events that this station can detect. The resolution on neutrino space angle due to reconstructing the entire event population is presented in figure 5.10. The resolution is around 5° which is essentially twice as large from the previous study on only using an LPDA trigger (Figure 5.9). This can be justified by the more than half of these additional events containing no LPDA signal at

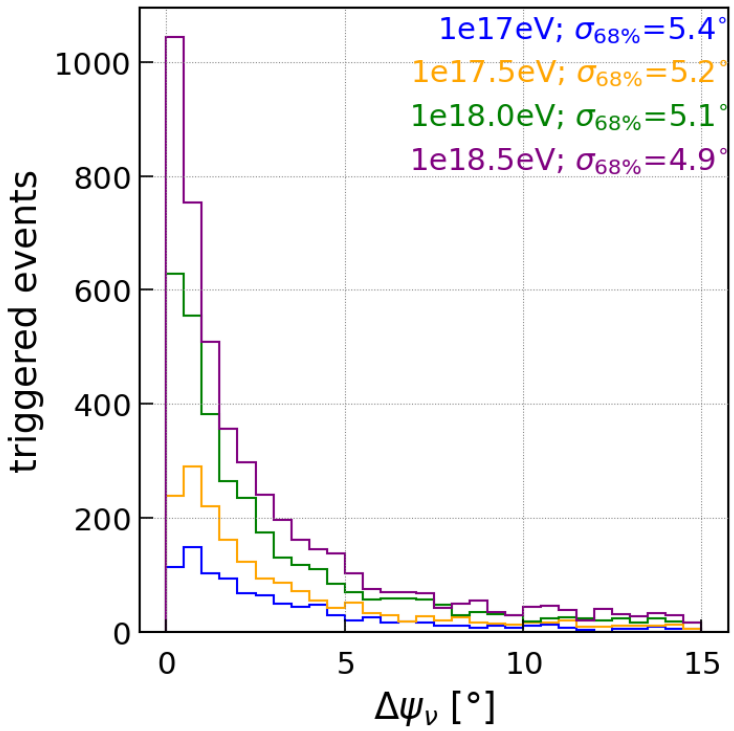

Figure 5.10: Space angle resolution for neutrino events that were triggered by either a narrow band LPDA 3.9 sigma trigger, or a Dipole 3.0 sigma trigger for a range of energies between 10^{17}eV and 10^{19}eV grouped into 0.5eV bins in log space. The legend labels the lower bound of each energy bin and the space angle resolution for that bin.

all (Last two columns of table 5.1). Therefore, even though there is a large increase in the total number events, all of these additional events have poor or no LPDA signals, which reduces the amount of information going into the reconstruction resulting in the degradation on neutrino space angle by a factor of two.

We next consider when an event has enough energy to trigger both trigger types. This extra criteria cuts the overall LPDA triggered events by roughly 20%, but has a significant improvement in space angle by roughly 1° as can be seen in 5.11. It was found that the events which triggered the LPDA's but did not trigger the dipole have a relatively large impact on neutrino space angle resolution due to most of the events originating from larger viewing angles. Therefore cutting these events out by requiring a three sigma signal in the dipoles removes these hard to model large viewing angle solutions. This criteria does not require

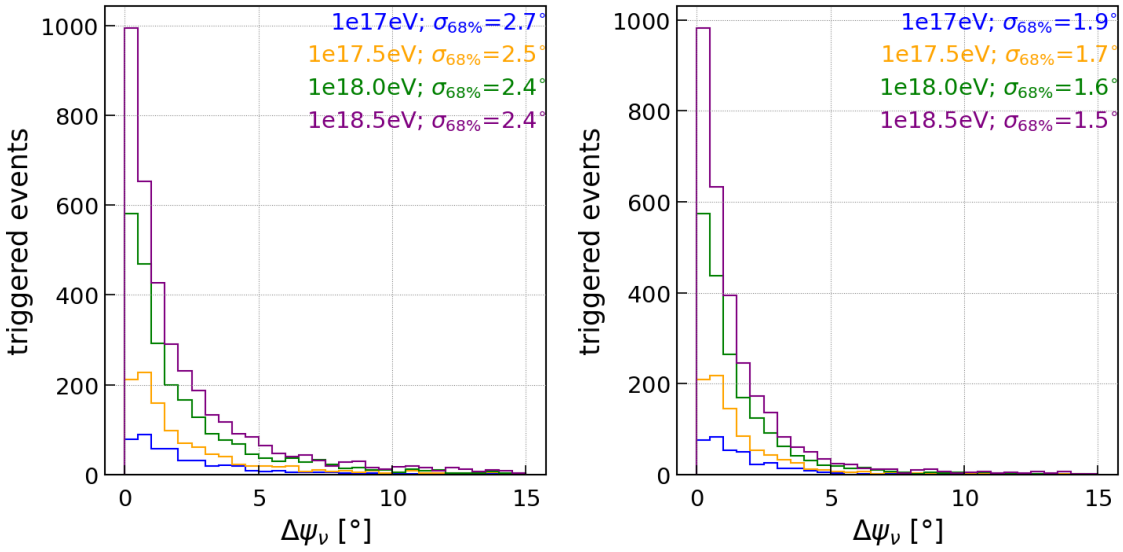

Figure 5.11: Space angle resolution for neutrino events that were triggered by: (left) narrow band LPDA 3.9 sigma trigger, or (right) a narrow band LPDA 3.9 sigma trigger and a dipole 3.0 sigma trigger. Both figures include a range of energies between 10^{17}eV and 10^{19}eV grouped into 0.5eV bins in log space. The legend labels the lower bound of each energy bin and the space angle resolution for that bin. Note that the dipole channel was made to have half the noise level during analysis in order to simulate the averaging of a phased array signal.

a phased array trigger, but a phased array setup does provide for a smaller noise floor in the dipole channel which improves the resolution on space angle by around 0.5° when only considering an LPDA trigger.

5.3.4 Site: Moore's Bay and South Pole

ARIANNA has detectors at both South Pole and Moore's Bay. Although all the studies thus far have used either the deployed ARIANNA South Pole station 51, or a simulated ARIANNA station at the South Pole (equivalent setup to station 52 at Moore's Bay), ARIANNA was originally constructed with the goal to scale the array at Moore's Bay. Therefore it is worth while to consider how Moore's Bay may effect ARIANNA's ability to reconstruct the neutrino space angle. The simulated detector for this setup does not include a phased array.

The key differences between Moore's Bay and South Pole are that Moore's Bay has a near perfect reflection layer at the bottom of the ice shelf, and that the ice thickness is only about 572 m versus 2.7 km at South Pole [16]. This results in Moore's Bay having a large sensitivity to neutrino events that are arriving from direction above the detector as opposed to the horizontally propagating direction that a South Pole detector is sensitive to. This can be seen in the vertex position distributions of neutrino events at the two sites in figure 5.2.

The neutrino space angle resolution for the two sites is shown in figure 5.13. Only neutrinos with energies of 10^{18}eV was studied as this energy is expected to produce the largest number of events for a typical GZK neutrino spectrum. Also this energy is centered at the energy range of neutrinos that ARIANNA expects to be able to detect, though there is a strong effort being made to extend the energy interval on both the high and low side. The space angle resolution at the South Pole is 2.7 degrees and at Moore's Bay is 3.6 degrees. The neutrino data set was re-simulated for both sites and therefore is not identical to the previous sections which all used the exact same neutrino data set. The differences in space angle resolution between the two sites can be attributed to the fact that Moore's Bay triggers on a lot of downward traveling neutrinos. This direction is not optimal for a dipole channel. Roughly 2/3 of the triggered events at Moore's Bay contains a signal in the dipole channel with a noiseless signal to noise ratio (SNR) of under 3. The noiseless SNR is defined as the ratio of the max signal amplitude without noise over the root mean square noise. At the South Pole, only 1/4 of events have a dipole noiseless SNR of under 3. Figure 5.11 shows that when studying events that have strong signals in both antenna types, that the neutrino space angle resolution improves by roughly 1°. The differences in neutrino space angle reconstruction between Moore's Bay and South Pole is attributed to more events with poor signals in the dipole channel.

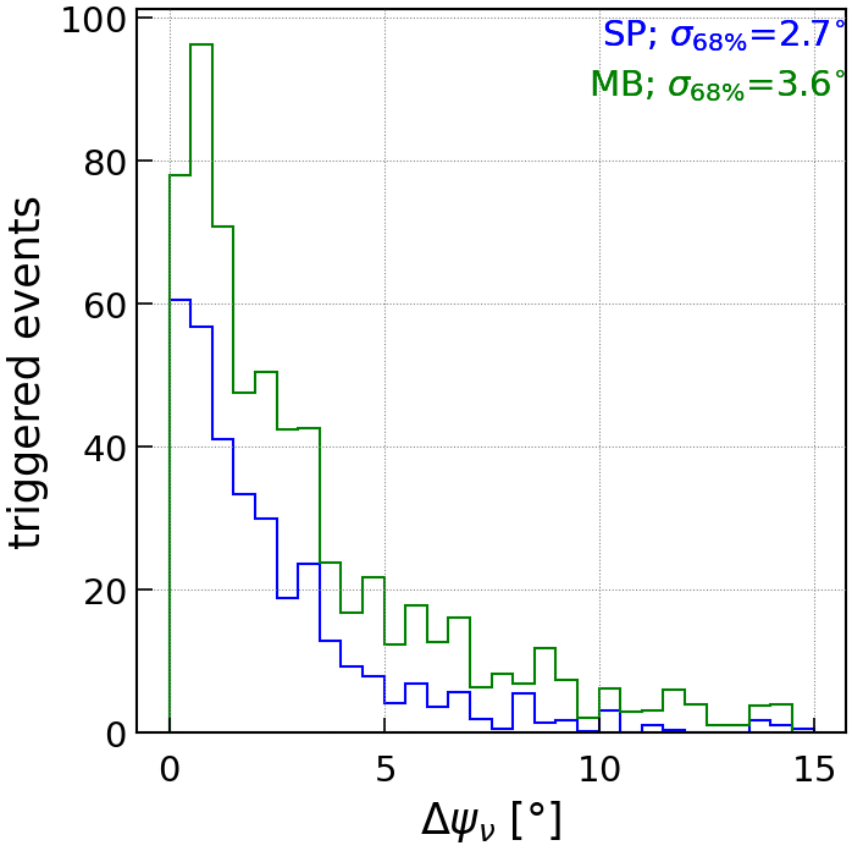

Figure 5.12: Space angle resolution for neutrino events with energy 10^{18}eV between the two ARIANNA sites; South Pole (SP) and Moore's bay (MB).

5.4 Systematic Errors

A few systematic uncertainties have been tested to see the effects on neutrino space angle reconstruction. First, the SPICE *in situ* radio frequency polarization results were tested against various changes in the LPDA orientations. In particular, all combinations of an azimuth error of 5° and zenith errors of 2° across the four LPDA's in station 51 were studied. In this test, the parallel LPDA's were rotated in opposite directions with the same azimuth and zenith errors from the SPICE study to maximize the uncertainty between them. The simulation of triggering on the events did not include the additional rotations in the LPDAs, only the reconstruction procedure had these errors included. The neutrino space angle resolution for 10^{18} eV neutrinos at the South Pole went from a resolution of 2.9° to 3.8°. We conclude that it is important to understand the antenna orientations with good precision, but we also note that the errors used are pessimistic and it is likely that the antenna orientations will be known to much better precision.

Another test looked at how the ice model effects the neutrino space angle resolution. The south pole 2015 ice model has been used for all of the previous studies in this chapter [16]. To test the ice model, during the reconstruction procedure, the South Pole simple model was used [16]. The parameters for each of these ice models are represented in table 5.2 and can be directly plugged into equation 2.4 to get the index of refraction at a particular depth.

Ice Profile	South Pole 2015	South Pole Simple
n_{ice}	1.78	1.78
Δn	0.423	0.426
z_0	77m	71m

Table 5.2: Ice model parameters for South Pole 2015 and South Pole simple [16]. See equation 2.4.

The space angle resolution for 10^{18} eV neutrinos at the South Pole changed from 2.9° to 4.0°. Small changes in the z_0 parameter results in relatively larger changes in the arrival

directions of the signals. Therefore, it is expected that the neutrino space angle resolution would diminish when not using the appropriate ice model. The density of the ice with depth can be measured with excellent precision. It is unlikely that the ice parameterization will have as large of an error as this systematic study.

Assuming that these systematic errors represent reality, then the error on the resolution of neutrino space angle is on the order of 1°. Running the reconstruction with different neutrino data sets results in roughly 0.2° differences on the neutrino space angle resolution. This number can be used as a first estimate of the error due to the reconstruction procedure itself.

5.5 Discussion of Neutrino Direction and Energy Reconstruction

We presented a Monte Carlo study for measuring the neutrino direction and energy. The method used a chi-squared minimization algorithm to fit the observed voltages to a set of reconstructed voltages found using the Alvarez 2009 model [18]. The study proved that the surface based neutrino detectors can reconstruct the direction and energy with excellent precision. The neutrino direction reconstruction resulted in a resolution of around 3°. This is important to multi-messenger astronomy for trying to narrow down the regions in the sky where UHE cosmic ray sources may be lurking. Deeper radio based neutrino detectors have around 5 times more effective volume than a surface based station at trigger level. However, if we require that an event be reconstructed with a space angle error of 3° or less, then the effective volume of surface stations is larger than deep stations as can be seen in figure **??**.

The neutrino energy reconstruction was on the order of 40% in log10 space which is below the inelasticity limit placed by the stochastic nature of hadronic showers. Therefore this

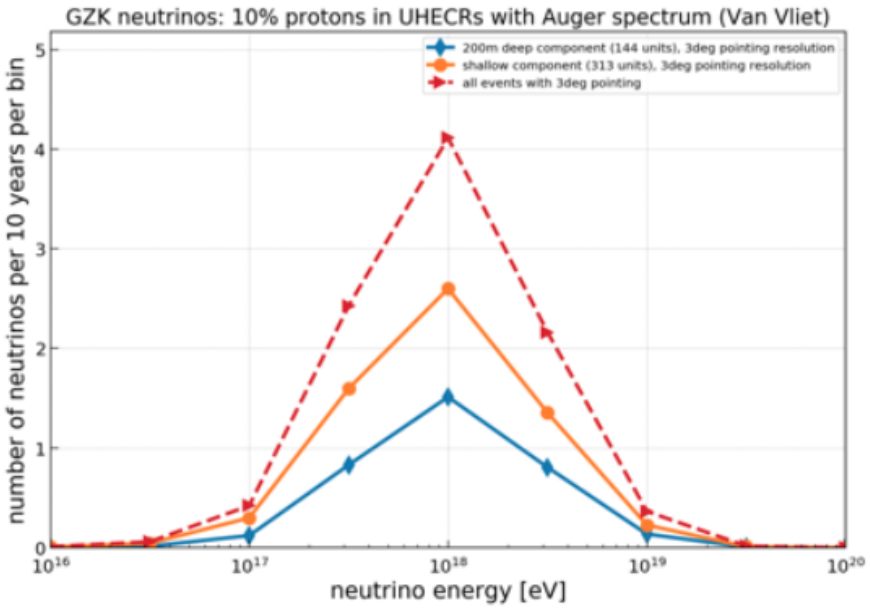

Figure 5.13: The number of triggered neutrino events as a function of neutrino energy with a direction resolution of 3° or better for either a deep station (in blue) or a shallow station (in orange), or a combination of the two (in red). Figure credit is given to Christian Glaser.

reconstruction method does not limit ARIANNA's ability to reconstruct the energy of most neutrino interactions. Further studies need to be performed to quantify the resolution of neutrino direction and energy for electromagnetic showers produced from electron neutrino charged current interactions.

Chapter 6

Conclusion

Advancing beyond coincidence measurements in multi-messenger astronomy requires precision reconstruction of various quantities for that messenger type such as angular direction and energy. For neutrinos to be used as a mechanism to discover the sources of UHE cosmic rays, excellent pointing accuracy and precision will need to be realized. A measurement of the three key ingredients for neutrino direction reconstruction has been presented through calibration pulses at the South Pole and through Monte Carlo simulations.

The first key ingredient that was measured is the radio signal's angular direction. Using the SPICE pulser data from 2018, the radio signal's angular direction was reconstructed with a resolution of 0.37°. A crucial take away from this result is that the ice effects on signal propagation direction can be corrected with high precision. The uncertainty on the radio signal's angular direction is statistical as their is no strong evidence for a systematic shift in the radio signal's direction as a function of depth.

Next the polarization was measured using the same SPICE pulser data from 2018. Reconstructing the electric field of the events and comparing them to an anechoic measurement of the SPICE pulser, the ARIANNA collaboration found an offset of 0.35° averaged over

all depths, and a scatter of 2.7°. The scatter contains a systematic oscillation pattern seen with depth, which is only observed in the amplitude of the cross polarization of the electric field. There was insufficient data taken in the anechoic chamber to rule the transmitter out as being the cause of this oscillation. A possible improvement of the polarization resolution would be through the construction of a forward folding technique to minimize the effects of the cross polarization antenna responses. One note is that the per depth statistical error of the polarization is under 1.0° which should serve as a goal for the polarization reconstruction methods in the future.

Lastly, the viewing angle was studied through Monte Carlo simulations, which ultimately resulted in a full reconstruction of the neutrino direction and shower energy. The key requirement for this method was vertex position reconstruction. The resolution on vertex position was studied in [17], and directly transferred to this work. ARIANNA finds the viewing angle resolution to be roughly 1° for 10^{18}eV neutrinos, which is the energy expected to produce the largest number of events for a typical GZK neutrino spectrum. The polarization resolution is the current bottle neck in the neutrino direction reconstruction.

The development of a method to reconstruct the viewing angle of a neutrino signal resulted in the reconstruction of neutrino direction and energy. The neutrino direction resolution of an ARIANNA shallow station was found to be around 3°. This is sufficient for coincidence measurements with the IceCube detector at high energies. Including a phased array provided additional events, but most of which had poor signals in the LPDA channels resulting in a worsening on neutrino direction reconstruction by nearly a factor of 2. Therefore it was concluded that the cost outweighs the gain. The shower energy resolution was found to be 0.15 in $\log10(E_{rec}/E_{true})$ which is below the inelasticity limit of around 0.3 for hadronic showers. This shows that the developed reconstruction method is sufficient for energy. Further studies need to be made for electron neutrino charged current interactions.

Neutrino based radio astronomy has proven to be a viable solution to detecting UHE neu-

trinos with excellent pointing resolution. This technique can be used to answer the age old question on what types of sources produce UHE cosmic rays as well as pushing the limits of high energy neutrino detection. A detector array such as ARIANNA would complement the multi-messenger industry, carving new insights in our understandings of the universe.

Bibliography

[1] L. Anchordoqui, T. Paul, S. Reucroft and J. Swain, *Ultrahigh energy cosmic rays: The state of the art before the auger observatory*, *International Journal of Modern Physics A* **18** (2003) 2229–2366.

[2] Particle Data Group collaboration, *Review of particle physics*, *Phys. Rev. D* **98** (2018) 030001.

[3] D. Harari, S. Mollerach and E. Roulet, *On the ultrahigh energy cosmic ray horizon*, *Journal of Cosmology and Astroparticle Physics* **2006** (2006) 012–012.

[4] M. Ackermann, M. Ajello, A. Albert, W. B. Atwood, L. Baldini, J. Ballet et al., *The spectrum of isotropic diffuse gamma-ray emission between 100 mev and 820 gev*, *The Astrophysical Journal* **799** (2015) 86.

[5] M. Ahlers and F. Halzen, *Opening a new window onto the universe with icecube*, *Progress in Particle and Nuclear Physics* **102** (2018) 73–88.

[6] T. P. A. Collaboration, A. Aab, P. Abreu, M. Aglietta, E. J. Ahn, I. A. Samarai et al., *The pierre auger observatory: Contributions to the 34th international cosmic ray conference (icrc 2015)*,

[7] E. Waxman and J. Bahcall, *High energy neutrinos from astrophysical sources: An upper bound*, *Physical Review D* **59** (1998) .

[8] C. Glaser et al., *NuRadioMC: Simulating the radio emission of neutrinos from interaction to detector*, *European Physical Journal* **C80** (2020) 77 [1906.01670].

[9] F. G. Schröder, *Radio detection of cosmic-ray air showers and high-energy neutrinos*, *Progress in Particle and Nuclear Physics* **93** (2017) 1–68.

[10] K. Kotera, D. Allard and A. Olinto, *Cosmogenic neutrinos: parameter space and detectabilty from pev to zev*, *Journal of Cosmology and Astroparticle Physics* **2010** (2010) 013–013.

[11] C. Glaser for the ARIANNA collaboration, *Neutrino direction and energy resolution of Askaryan detectors*, in *36th International Cosmic Ray Conference (ICRC2019)*, vol. 36 of *International Cosmic Ray Conference*, p. 899, July, 2019, 1911.02093.

[12] Google Maps, NASA Map data 2020, https://www.google.com/maps/@-78.116915,168.2218667,245011m/data=!3m1!1e3.

[13] J. M. Souney et al., *The South Pole ice core (SPICEcore) project*, *American Geophysical Union, Fall Meeting 2018, abstract C41C-1771* (2018) .

[14] S. Barwick, D. Besson, A. Burgman, E. Chiem, A. Hallgren, J. Hanson et al., *Radio detection of air showers with the arianna experiment on the ross ice shelf*, *Astroparticle Physics* **90** (2017) 50–68.

[15] C. R. Persichilli, *Performance and Simulation of the ARIANNA Pilot Array, with Implications for Future Ultra-high Energy Neutrino Astronomy*, Ph.D. thesis, University of California, Irvine, 2018.

[16] S. Barwick et al., *Observation of classically 'forbidden' electromagnetic wave propagation and implications for neutrino detection.*, *Journal of Cosmology and Astroparticle Physics* **2018** (2018) 055–055 [1804.10430].

[17] A. Anker, S. Barwick, H. Bernhoff, D. Besson, N. Bingefors, D. García-Fernández et al., *Neutrino vertex reconstruction with in-ice radio detectors using surface reflections and implications for the neutrino energy resolution*, *Journal of Cosmology and Astroparticle Physics* **2019** (2019) 030–030.

[18] J. Alvarez-Muñiz, A. Romero-Wolf and E. Zas, *Practical and accurate calculations of askaryan radiation*, *Phys. Rev. D* **84** (2011) 103003.

[19] C. Reed for the ARIANNA collaboration, *Performance of the ARIANNA Hexagonal Radio Array*, in *34th International Cosmic Ray Conference (ICRC2015)*, vol. 34 of *International Cosmic Ray Conference*, July, 2015, 1509.00109.

[20] A. Nelles, *Cosmic-ray detection with and novel reconstruction algorithms for the ARIANNA experiment*, in *36th International Cosmic Ray Conference (ICRC2019)*, vol. 36 of *International Cosmic Ray Conference*, p. 366, July, 2019.

[21] C. Glaser et al., *NuRadioReco: A reconstruction framework for radio neutrino detectors*, *European Physical Journal* **C79** (2019) 464 [1903.07023].

[22] E. C. Pettit, "South Pole (SPICEcore) Borehole Deformation, U.S. Antarctic Program (USAP) Data Center." https://doi.org/10.15784/601315,

[23] *Evidence for high-energy extraterrestrial neutrinos at the icecube detector*, *Science* **342** (2013) 1242856–1242856.

[24] R. Ruffini, G. V. Vereshchagin and S.-S. Xue, *Cosmic absorption of ultra high energy particles*, *Astrophysics and Space Science* **361** (2016) .

[25] M. Amenomori, Y. Bao, X. Bi, D. Chen, T. Chen, W. Chen et al., *First detection of photons with energy beyond 100 tev from an astrophysical source*, *Physical Review Letters* **123** (2019) .

[26] B. Abbott, R. Abbott, T. Abbott, M. Abernathy, F. Acernese, K. Ackley et al., *Observation of gravitational waves from a binary black hole merger*, *Physical Review Letters* **116** (2016) .

[27] V. Hess, *On the observations of the penetrating radiation during seven balloon flights*,

[28] J. Linsley, *Evidence for a primary cosmic-ray particle with energy* 10^{20} *ev*, *Phys. Rev. Lett.* **10** (1963) 146.

[29] A. J. Smith, *The MILAGRO Gamma Ray Observatory*, in *29th International Cosmic Ray Conference (ICRC29), Volume 10*, vol. 10 of *International Cosmic Ray Conference*, p. 227, Jan., 2005.

[30] P. D. Group, P. A. Zyla, R. M. Barnett, J. Beringer, O. Dahl, D. A. Dwyer et al., *Review of Particle Physics*, *Progress of Theoretical and Experimental Physics* **2020** (2020) [https://academic.oup.com/ptep/article-pdf/2020/8/083C01/34673722/ptaa104.pdf].

[31] J. V. Jelley, J. H. Fruin, N. A. Porter, T. C. Weekes, F. G. Smith and R. A. Porter, *Radio Pulses from Extensive Cosmic-Ray Air Showers*, **205** (1965) 327.

[32] A. Anker et al., *White Paper: ARIANNA-200 high energy neutrino telescope*, 2004.09841.

[33] P. B. Price, *Comparison of optical, radio, and acoustical detectors for ultrahigh-energy neutrinos*, *Astropart. Phys.* **5** (1996) 43 [astro-ph/9510119].

[34] ARIANNA collaboration, *Targeting ultra-high energy neutrinos with the ARIANNA experiment*, *Advances in Space Research (in press)* (2019) [1903.01609].

[35] ARA collaboration, *Performance of two Askaryan Radio Array stations and first results in the search for ultrahigh energy neutrinos*, *Phys. Rev. D* **93** (2016) 082003 [1507.08991].

[36] I. Kravchenko, G. Frichter, D. Seckel, G. Spiczak, J. Adams, S. Seunarine et al., *Performance and simulation of the rice detector*, *Astroparticle Physics* **19** (2003) 15–36.

[37] J. A. Aguilar, P. Allison, J. J. Beatty, H. Bernhoff, D. Besson, N. Bingefors et al., *Design and sensitivity of the radio neutrino observatory in greenland (rno-g)*,

[38] J. Álvarez Muñiz, R. Alves Batista, A. Balagopal V., J. Bolmont, M. Bustamante, W. Carvalho et al., *The giant radio array for neutrino detection (grand): Science and design*, *Science China Physics, Mechanics Astronomy* **63** (2019) .

[39] P. Gorham, F. Baginski, P. Allison, K. Liewer, C. Miki, B. Hill et al., *The exavolt antenna: A large-aperture, balloon-embedded antenna for ultra-high energy particle detection*, *Astroparticle Physics* **35** (2011) 242–256.

[40] J. H. A. J. au2, L. A. Anchordoqui, J. A. Apple, M. E. Bertaina, M. J. Christl, F. Fenu et al., *White paper on euso-spb2*,

[41] J. W. Nam, C. C. Chen, C. H. Chen, C. W. Chen, P. Chen, Y. C. Chen et al., *Design and implementation of the TAROGE experiment*, *International Journal of Modern Physics D* **25** (2016) 1645013.

[42] P. Allison, J. Alvarez-Muñiz, J. J. Beatty, D. Z. Besson, P. Chen, Y. Chen et al., *The payload for ultrahigh energy observations (pueo): A white paper*,

[43] W. D. Reeve, "Modeling and measuring the creative design clp5130-2n log periodic antenna." `http://www.reeve.com/Documents/ArticlesPapers/Reeve_LogPeriodicAntennaModel.pdf`,

[44] B. Kolundzija, *Wipl-d: From university software to company product*, in *Proceedings of the 5th European Conference on Antennas and Propagation (EUCAP)*, pp. 2844–2846, 2011.

[45] S. W. Barwick, E. C. Berg, D. Z. Besson, E. Cheim, T. Duffin, J. C. Hanson et al., *Design and performance of the arianna hexagonal radio array systems*,

[46] T. Prakash, *A Fully-Synchronous Multi-GHz Analog Waveform Recording and Triggering Circuit*, Ph.D. thesis, University of California, Irvine, Jan., 2017.

[47] T. Prakash, *Multi-Gigahertz Synchronous Sampling and Triggering (SST) Circuit with Picosecond Timing Resolution*, Ph.D. thesis, University of California, Irvine, 2017.

[48] TAROGE, ARIANNA collaboration, *Calibration, Performance, and Cosmic Ray Detection of ARIANNA-HCR Prototype Station*, *PoS* **ICRC2017** (2018) 358.

[49] V. Schytt, *(norwegian-british-swedish antarctic expedition)*, *Scientific results Norsk Polarinstitutt 1949-52* (1958) 113–151.

[50] NuRadioReco, https://github.com/nu-radio/NuRadioReco.

[51] NuRadioMC, https://github.com/nu-radio/NuRadioMC.

[52] A. Anker, S. Barwick, H. Bernhoff, D. Besson, N. Bingefors, D. García-Fernández et al., *Probing the angular and polarization reconstruction of the arianna detector at the south pole*, *Journal of Instrumentation* **15** (2020) P09039–P09039.

[53] ARIANNAanalysis, https://github.com/ggaswint/ARIANNAanalysis.

[54] T. E. Oliphant, *A guide to NumPy*. USA: Trelgol Publishing, 2006.

[55] *Dash (2019)*, URL https://plot.ly/products/dash/.

[56] P. Virtanen, R. Gommers, T. E. Oliphant, M. Haberland, T. Reddy, D. Cournapeau et al., *SciPy 1.0: Fundamental Algorithms for Scientific Computing in Python*, *Nature Methods* **17** (2020) 261.

[57] C. A. et al. (Particle Data Group), *Monte Carlo Particle Numbering Scheme*, *Physics Letters B667* (2018) .

[58] R. Gandhi, C. Quigg, M. H. Reno and I. Sarcevic, *Neutrino interactions at ultrahigh energies*, *Physical Review D* **58** (1998) .

[59] J. Alvarez-Muñiz, W. R. Carvalho, M. Tueros and E. Zas, *Coherent cherenkov radio pulses from hadronic showers up to eev energies*, *Astroparticle Physics* **35** (2012) 287–299.

[60] J. C. Hanson et al., *Radar Absorption, Basal Reflection, Thickness, and Polarization Measurements from the Ross Ice Shelf*, *Journal of Glaciology* (2014) [1410.7134].

[61] T. Huege, *Radio detection of cosmic ray air showers in the digital era*, *Physics Reports* **620** (2016) 1.

[62] C. Glaser, M. Erdmann, J. R. Hörandel, T. Huege and J. Schulz, *Simulation of Radiation Energy Release in Air Showers*, *Journal of Cosmology and Astroparticle Physics* **2016** (2016) 24.

[63] A. Shultz, U. Latif and A. S. Novikov, "SPICE Pulser: The Guide." https://usermanual.wiki/Document/SpicePulserTheGuide.1535821065/html,

[64] "The University of Kansas, Anechoic Chamber." https://chamber.ku.edu/specifications,

[65] I. Kravchenko, D. Besson and J. Meyers, *In situ index-of-refraction measurements of the South Polar firn with the RICE detector*, *Journal of Glaciology* **50** (2004) 522.

[66] R. Lahmann for the ARIANNA collaboration, *Investigations of ice and emitter properties from radio signals recorded with ARIANNA*, in *36th International Cosmic Ray Conference (ICRC2019)*, vol. 36 of *International Cosmic Ray Conference*, p. 939, July, 2019.

[67] G. Gaswint for the ARIANNA collaboration, *New results on angular reconstruction of deep pulser radio signals*, in *36th International Cosmic Ray Conference (ICRC2019)*, vol. 36 of *International Cosmic Ray Conference*, p. 897, July, 2019.

Appendix A

Steps to Reproduce and Advance Work

A.1 Software Requirements

The first steps in reproducing the work outlined in this thesis is to install all the required software. ARIANNAanalysis is a good starting spot for weaving through this process. Check out the installation section in the README markdown of this Github page [53] to see steps for installing all of the required software. The README also contains documentation of the various pieces of software included within the ARIANNAanalysis repository. One way to download the ARIANNAanalysis software is to clone the repository through the command line with the command:

```
$ git clone https://github.com/ggaswint/ARIANNAanalysis.git
```

If using a terminal is unfamiliar territory, then please google some quick guides to the command line. The rest of this appendix will be focused on the analysis scripts found within

the ARIANNAanalysis Github repository that are required to reproduce the work outlined in this thesis. The code base is written in python and relies heavily on NuRadioReco and NuRadioMC [8, 21]. For a detailed discussion on how NuRadioReco and NuRadioMC works, see [8, 21] or chapter 3.

Note that as NuRadioReco and NuRadioMC evolve, some of the more complex analysis software in ARIANNAanalysis may need to be tuned to incorporate these changes. It should hopefully be straightforward to modify, but if there is any difficulty, do not hesitate to email me at ggaswint@gmail.com

A.2 Radio Frequency Signal Direction Reconstruction

The RF angular reconstruction is a key measurement in determining the neutrino direction and the vertex position. It is typically the first measurable that would be reconstructed as other modules depend on it. It is also one of the simplest in terms of code length and complexity. The incoming radio direction of a particular event is found by fitting the time delays between channels, calculated from an input grid of possible arrival directions, to the actual time delays seen in that event. In particular, for an ARIANNA station with two sets of parallel LPDAs, the time delays are taken to be between the two parallel antennas. Parallel LPDAs should see essentially identical signals and therefore errors in modeling the antenna response has less of an impact on the ability to reconstruct the time delays. In fact, the antenna model can be completely ignored when assuming the antenna properties and arrival direction are identical between pairs.

The key function in the RF direction reconstruction is outline below. This code can be found within the NuRadioReco software under modules and is called "correlationDirectionFitter.py". In this set up, channels 0 and 2 are two parallel LPDAs, while channels 1 and

3 are another set of parallel LPDAs. These two sets are perpendicular to each other. The positions are saved as a pair, and the time delays are considered for each pair separately. The true time delays for the event in question is found through correlating the two parallel channels together.

```
def ll_regular_station(angles, corr_02, corr_13, sampling_rate, positions,
    trace_start_times):
    zenith = angles[0]
    azimuth = angles[1]
    times = []

    for pos in positions:
        tmp = []
        tmp.append(geo_utl.get_time_delay_from_direction(zenith, azimuth, pos[0],
                n=n_index))
        tmp.append(geo_utl.get_time_delay_from_direction(zenith, azimuth, pos[1],
                n=n_index))
        times.append(tmp)

    delta_t_02 = times[0][1] - times[0][0]
    delta_t_13 = times[1][1] - times[1][0]
    delta_t_02 -= (trace_start_times[0][1] - trace_start_times[0][0])
    delta_t_13 -= (trace_start_times[1][1] - trace_start_times[1][0])
    delta_t_02 *= sampling_rate
    delta_t_13 *= sampling_rate
    pos_02 = int(corr_02.shape[0] / 2 - delta_t_02)
    pos_13 = int(corr_13.shape[0] / 2 - delta_t_13)

    weight_02 = np.sum(np.abs(corr_02))
    weight_13 = np.sum(np.abs(corr_13))

    likelihood = -1 * (corr_02[pos_02] / weight_02 + corr_13[pos_13] / weight_13)
```

```
    return likelihood
```

ARIANNAanalysis contains all the scripts and data necessary to reproduce the figures in chapter 4. A few scripts in particular will be highlighted as they are related to the RF angular direction reconstruction. First, the data is located in the data directory which contains raw and processed data so that any step along this procedure can be executed without having to run a previous step. The script called "plotAngularDirectionPlusHist.py" will make figure 4.7 directly from already processed data. This is useful for learning how the plots were made, however none of the reconstruction process is found in this script.

To reconstruct the angular direction of the SPICEcore [13] events in the ARIANNA South Pole station (i.e. station 51) from the December 30th 2018 run, execute "getAngularReconstructionDataNurInput.py". You can execute all of these scripts directly from a command line interface by typing for example:

```
$ python getAngularReconstructionDataNurInput.py
```

This script is currently setup to read the SPICEcore data from 2018 which is saved as a .nur file and located in the data directory. If a different set of data was to be processed using this script, a few changes would need to be made. The input file will need to be modified and the function that converts a time stamp to the depth of the SPICE pulser at that time will have to be adjusted or removed. This particular script is the only one that includes a Root file input version and a Nur file input version. It is recommended to use Nur input file types but both produce the same results. See the installation instructions for some more details.

The study in this thesis included a recalculation of cable delays by looking at the average timing differences between channels after accounting for all known effects and adjusting the cable delays accordingly. The recalculation was seen as a more precise measurement of the

cable delays. To calculate the additional cable delays in this manner, execute "calculateCableDelayErrorsSpice2018Station51.py". This script is tuned to the SPICEcore 2018 data, and so a few minor modifications will need to be made which include the input file type and the conversion between event time and SPICE pulser depth (lines 120-121). Also line 131 calculates the zenith angle according to the geometry in the SPICE setup.

Note, to look at the space angle of the RF signal, use the plotting script "plotSpaceAngularDirectionPlusHist.py" on the same RF angular data set. The distribution is now Rayleigh like and the resolution is comparable to adding the resolution for RF zenith and RF azimuth in quadrature showing that the two measurements are more or less independent from each other.

It is likely that the RF angular reconstruction with a sub degree resolution in space angle will not be further tuned as this is not the limiting factor in ARIANNA's ability to reconstruct the neutrino direction.

A.3 Radio Frequency Signal Polarization Reconstruction

In order to reconstruct the polarization, a reconstruction of the events electric field needs to be done. This is essentially the entire process of obtaining a polarization measurement. Reconstructing the electric field boils down to deconvolving the antenna responses and that requires the signal arrival direction. Therefore this process should proceed the RF angular direction reconstruction outlined in the previous section.

The main module for deconvolving out the antennas is found in NuRadioReco under modules and is called "voltageToEfieldConverter.py". The python code to implement this module is

shown below:

```
voltageToEfieldConverter.run(evt, station, det, use_channels=chans,
    force_Polarization='')
electricFieldBandPassFilter.run(evt, station, det,
    passband=[lower * units.MHz, upper * units.MHz], filter_type='rectangular')
```

There are a few things to note with this code. The electric field can be reconstructed with a subset of the total channels in the ARIANNA station such as using only the LPDAs. Recall that in order to reconstruct the full electric field, multiple polarizations will need to be captured in the event which means that orthogonal antennas will need to be deployed for each station. However, there is a way to reconstruct the electric field for only one polarization component such as only using the vertically oriented dipoles in an ARIANNA station. The "force_Polarization" parameter does just this. When set to an empty string it is ignored, but when set to either eTheta or ePhi, the module will reconstruct the electric field for only that polarization. This is useful for the dipoles since the cross-pol component is essentially 0, but not exactly. It is hard to model the cross-pol component of the dipole antennas and this can lead to large errors in the electric field. By forcing the polarization, these errors are ignored.

Also note that there is a separate band pass filter module for the electric field. This is because the electric field's data structure is different than the voltage trace's data structure and NuRadioReco version 1.2 treats the band pass filter separately for these two classes. Keep in mind that if a band pass filter is applied to the voltage traces, then it should also be applied to the electric field after reconstruction.

When the electric field is reconstructed the polarization can then be determined through:

```
etheta = station.get_electric_fields()[0].get_trace()[1]
ephi = station.get_electric_fields()[0].get_trace()[2]
```

```
h_etheta = hilbert(etheta)
h_ephi = hilbert(ephi)
h2 = np.sqrt(np.abs(h_etheta)**2 + np.abs(h_ephi)**2) # abs takes care of complex numbers
fwhm = hp.get_FWHM_hilbert(h2)

IW = int(sampling_rate*70.0) # length of window is 70ns
mid_fwhm = fwhm[0] + int((fwhm[1] - fwhm[0])/2) # Center of FWHM
noise_idx = int(1.1*int(mid_fwhm+IW/2)) # Noise start
signal_idx = int(mid_fwhm+IW/2) # signal end

f_etheta = np.sqrt(np.sum(etheta[signal_idx-IW:signal_idx]**2)
    - np.sum(etheta[noise_idx:noise_idx+IW]**2))
f_ephi = np.sqrt(np.sum(ephi[signal_idx-IW:signal_idx]**2)
    - np.sum(ephi[noise_idx:noise_idx+IW]**2))

polarization_angle = np.rad2deg(np.arctan(f_ephi/f_etheta))
```

This process uses the end of the electric field trace to determine the noise contribution and subtracts this off. Note that the process in reconstructing the electric field includes padding 0 values at the beginning and end to prevent wrapping effects when rolling a trace to account for timing delays. Therefore the appropriate noise window is just after the signal and not at the end of the entire window. The polarization is defined as 0 degrees being entirely eTheta polarized and 90 degrees being entirely ePhi polarized.

When first reconstructing the electric field, the location of this electric field is at the receiver or the ARIANNA station. Deconvolving ice effects such as frequency dependent attenuation is necessary to represent the electric field at the source. There are two scripts in ARIANNAanalysis for either getting the electric field at the receiver or at the source. The setup is again for the SPICE 2018 data and modifications will need to be made to perform this procedure on different data sets.

The polarization reconstruction is found to be the limiting factor in the neutrino direction reconstruction. The biggest evidence for possible improvement in polarization reconstruction can be seen in figure 4.11 through the systematic error of 2.7 degrees. The depth independent statistical errors are much smaller on sub degree scales and could be the goal for the polarization resolution. The systematic error results from the oscillatory behavior of the depth dependent polarization in figure 4.11. This oscillation results from the cross polarization component which in this geometry is the ePhi component. This can be seen in figure 4.13.

The systematic error may originate from the transmitter. It was not possible to get a finer analysis of the transmitted pulses as a function of launch angle which changes with depth. Therefore this is left as an uncertainty. One possible solution to the systematic error seen in the polarization reconstruction would be to minimize errors in the antenna modeling of the cross polarization response. Some studies do this by developing a forward folding technique where one minimizes on the events voltage traces from a set of predicted voltage traces due to various polarizations. However, this requires a good understanding of the electric field at the source, which could be obtained for SPICE data through good Anechoic measurements of the transmitter or for neutrinos through semi-analytic models. By performing a forward folding method, the hard to model cross polarization response of the antennas has less of an impact. This is because when forward folding, the small responses due to poor geometries is multiplied by the electric field instead of divided out by the voltage traces when working in the frequency domain. Dividing by small numbers causes the noise to be amplified and typically is responsible for the uncertainties in a deconvolution technique.

The polarization reconstruction done on the SPICE data has been heavily studied through systematic changes in the antenna positions, orientations, energy fluence windows, noise window definitions, and through changing the ice profile along with tilts in the SPICE hole. None of these studies removed the oscillations seen in the polarization reconstruction. Further the expected electric fields that were provided only corresponded to a single depth

for the SPICE data seen in station 51. It could be that the transmitter had some poorly understood effects that were not accounted for. Any future study should strive for a more detailed understanding of the expected signals in order to remove this as a possible source of error in the reconstruction.

A.4 Python Code for Reconstructing Neutrino Energy and Direction

Reconstructing the neutrino angular direction and energy requires a Monte Carlo simulation. All the driver scripts can be found in ARIANNAanalysis for this procedure. The first step is to create a neutrino data set which stores neutrino information such as energy, flavor, and vertex position in an hdf5 file format. To do this, run "produceNeutrinoDataSet.py" which is currently configured to produce ten neutrinos with energies of 10^{19}eV within a cylindrical volume appropriate for the South Pole.

Once the neutrinos have been saved, the propagation and convolution with a detector needs to be simulated. "simulateNeutrinoEventDetection.py" performs this process. This file is different from all other scripts in ARIANNAanalysis in that it requires input arguments from the command line. All of the necessary inputs to get started are within the ARIANNAanalysis repository. An example command for running this script is found at the end of "simulateNeutrinoEventDetection.py". For this command to work, it should be executed in the ARIANNAanalysis directory.

One of the input arguments contains a path to a configuration file named "simulateNeutrinosConfig.yaml" which is used to change the simulation setup such as the neutrino parameterization, ice model, and adding noise. A default configuration can be found in NuRadioMC under simulation which can be used as a template to see all the different parameters that can

be modified. Another input file is the station's configuration. The current setup contains an ARIANNA five channel station with four LPDAs and one central dipole. However, the station configuration has ten channels, each one is duplicated. The duplicated channels are for triggering purposes only and are simulated to apply a narrow band filter. Any changes to the station's configuration will likely require changes to "simulateNeutrinoEventDetection.py", specifically in terms of channel identifiers and triggering mechanisms.

The triggering implementation is fairly self explanatory, but is also described below:

```
highLowThreshold.run(evt, station, det,
                     threshold_high=threshold_high,
                     threshold_low=threshold_low,
                     coinc_window=40 * units.ns,
                     triggered_channels=[5, 6, 7, 8],  # select the LPDA channels
                     number_concidences=2,  # 2/4 majority logic
                     trigger_name='LPDA_2of4_3.9sigma')
```

The triggering code snippet above simulates a duel threshold 2 of 4 majority logic trigger on the duplicated LPDA channels with identifiers between 5 and 8. The 2 of 4 majority logic coincidence window and thresholds are inputs to this function. The trigger name is what will be stored within the event data structure and can be used to identify which trigger was used for that event, which is useful when there are multiple triggers at play.

The input neutrino data set only contains ten events, but the simulated energies are large at 10^{19}eV. This typically results in one triggered event when running the simulation process of triggering with the ARIANNA station. If the event barely meets the threshold with noise added, then it can be that some runs do not trigger the station whereas others do. This is because the noise is seeded by a different number for each execution.

The output simulation data is what will be used to test the neutrino energy and direction

reconstruction using an ARIANNA detector. The driver script called "runNeutrinoReconstruction.py" should be executed to obtain the reconstructed data. The core of this driver code is executing "voltageToEfieldAnalyticConverterForNeutrinos.py" which will be incorporated into NuRadioReco but is also provided in the ARIANNAanalysis repository, and the driver code is currently pointing to the ARIANNAanalysis version. This method will reconstruct the voltage traces due to an Askaryan signal originated at the simulated vertex position for a range of neutrino zenith and azimuth directions along with a range of energies. The details are further described in section 3.5.

"runNeutrinoReconstruction.py" is setup to run on a single event. This was done to allow for parallel processes so that multiple events can be reconstructed at the same time, since a single reconstruction can take up to thirty minutes. University of California, Irvine's HPC3 cluster is typically used to create many bash jobs each for an individual event and then submitted to the Slurm cluster that HPC3 uses. Currently, the scripts are setup to process locally only a single event. This takes roughly fifteen minutes on my standard and fairly cheap laptop which is a 2016 Acer Aspire using Ubunutu 18.

Once an event is reconstructed, the data is stored as a dictionary and saved as a numpy file. For analysis of many events, multiple numpy files will be saved and need to be concatenated together to use the plotting script provided. For things to work out of the box, it is recommended to concatenate the data in a way that the keys in the dictionary point to arrays of the reconstructed values such as an array of all the reconstructed neutrino zenith angles. Once a final data set is constructed, run "plotNeutrinoReconstructionData.py" to create similar histograms to the ones presented in chapter 5. This is currently setup to make the figures using only a single reconstructed event, which is also provided in the data directory of ARIANNAanalysis. The full data samples used in chapter 5 are omitted from the directory to prevent the repository from taking up a lot of disk space. The data can be requested by emailing me at ggaswint@gmail.com. Happy analysis!